An Estimate of the Hadron Production Uncertainty and a Measurement of the Rate of Proton Emission after Nuclear Muon Capture for the COMET Experiment

Andrew William John Edmonds
University College London

Submitted to University College London in fulfilment
of the requirements for the award of the
degree of **Doctor of Philosophy**

May 28, 2015

Declaration

I, Andrew William John Edmonds confirm that the work presented in this thesis is my own. Where information has been derived from other sources, I confirm that this has been indicated in the thesis.

Andrew Edmonds _____

Abstract

The COherent Muon to Electron Transition (COMET) experiment will be searching for the charged lepton flavour violating process $\mu^- + N(Z, A) \rightarrow e^- + N(Z, A)$ in aluminium with a single event sensitivity of 3×10^{-17}.

In order to achieve this sensitivity, COMET will utilise a novel pion capture solenoid and a high power proton beam to create the most intense pulsed muon beam in the world. Because these are innovative technologies, it is not known exactly what the muon yield will be and so, in this thesis, simulations of this section of the experiment have been performed using a variety of hadron production models in order to estimate the muon yield and its uncertainty.

Another aspect required to achieve such a low sensitivity is that all possible sources of background need to be known and accounted for. One of the less well measured backgrounds is caused by protons emitted after the muon has been captured by a nucleus and so the AlCap experiment was set up to measure the rate of this process and, in this thesis, an analysis of the data collected in the first AlCap run is presented.

Throughout this thesis, natural units will be used where $\hbar = c = 1$.

Acknowledgements

There have been many people who I feel I should thank for their help, guidance and friendship over these past few years. Unfortunately, there are far too many of you and so my sincere apologies if you are not mentioned here.

First and foremost, I would like to thank my supervisor, Mark Lancaster, for all his help and guidance over the course of my studies.

Secondly, I would like to thank those people who I have worked closely with on both COMET and ALCAP including Phill L, Ben K, Nam T and John Q.

Thirdly, I would like to thank the people I have worked physically close to and see day-in-day out (unless they're on some trip to an exciting corner of the globe) and regularly field my ROOT questions – the C17 crew: Ben S, Becca, Andy and Ash.

Fourthly, I would like to thank all those at UCL who have kept me entertained with a very ancient and fish-like smell (crosswords), the Xinema Cliub (films) and good times at the JB (drinks): Xin, Tomas, Becky, Alex, Patrick, Ines and Guillaume.

Fifthly, I would like to thank those people outside of both UCL and physics who have kept me vaguely in touch with reality, some of whom I have known for many, many years (they may say too many): Ed, James, Matt G, Stu, Greg, Alvaro, Matt M, Paola and Marc.

Sixthly (probably not a word), I would like to wish my brother, Paul, and his fiancee, Jo, many happy years together.

Finally, I would like to thank my parents for teaching me the value of hard work, without which this thesis would not exist.

Contents

List of Figures

List of Tables

"Physics is puzzle solving, too, but of puzzles created by nature..."
— Maria Goeppert Mayer

"The nice thing about doing a crossword puzzle is, you know there is a solution."
— Stephen Sondheim

Chapter 1

The Standard Model

"Flag display is currently the best, in theory (8, 5)"
— Phssthpok, *Financial Times #14312*

1.1 Overview

1.1.1 Particle Content of the Standard Model

The Standard Model is currently the best theoretical model of the interactions between elementary particles via three of the four fundamental forces.

Mathematically, it is a quantum field theory that consists of seventeen types of field: twelve fermionic fields, which represent the matter particles; and five bosonic fields, of which four represent the carriers of the weak, electromagnetic and the strong forces and one represents the Higgs boson [1]. These particles and some of their important properties are shown in Table 1.1.

The gauge symmetry of the Standard Model is that of an $SU(3)_C \times SU(2)_L \times U(1)_Y$ gauge group where C indicates colour charge, L indicates that only left-handed fields participate in the weak interaction and Y is the hypercharge. The $SU(2)_L \times U(1)_Y$ electroweak part of the gauge group breaks down to the $U(1)_{EM}$ of electromagnetism via the Higgs mechanism.

	Particle	Charge	Spin
Fermions	**up-type quarks** (u, c, t)	$+\frac{2}{3}$	$\frac{1}{2}$
	down-type quarks (d, s, b)	$-\frac{1}{3}$	$\frac{1}{2}$
	charged leptons (e, μ, τ)	-1	$\frac{1}{2}$
	neutral leptons (ν_e, ν_μ, ν_τ)	0	$\frac{1}{2}$
Bosons	**strong force carrier** (g)	0	1
	weak force carriers ($W^\pm$, Z^0)	±1 ($W^\pm$), 0 (Z^0)	1
	electromagnetic force carrier (γ)	0	1
	Higgs boson (H)	0	0

Table 1.1: The particle content of the Standard Model.

Experimentally, the Standard Model has been phenomenally successful in calculating and predicting many observables including the anomalous magnetic moment of the electron (measured to 10 significant figures [2, 3]) and the existence of the Higgs boson (discovered in the LHC at CERN in 2012 [4, 5]), neutral currents [6], the tau neutrino [7] and the top quark [8, 9].

1.1.2 Shortcomings of the Standard Model

However, it is known that the Standard Model is not a complete theory of the universe for the following reasons:

- Gravity is not described.
- The matter-antimatter asymmetry of the universe is not fully explained.
- 96% of the universe (dark matter and dark energy) is not described.
- Neutrino mass is not fully explained.

In addition, the Standard Model suffers from fine tuning problems, where parameters have to be precisely adjusted in order to match observations with no a priori reason for doing so.

Gravity

Gravity is very well described by General Relativity at galactic scales, explaining phenomena such as gravitational lensing [10] and at macroscopic scales reduces to Newtonian gravitation. However, when trying to describe gravity at quantum scales, one has to unite General Relativity and Quantum Mechanics which results in an unrenormalisable theory and means that calculations are impossible and so the Standard Model does not attempt to incorporate gravity.

Matter-Antimatter Asymmetry

The matter-antimatter asymmetry of the universe can be explained through CP violation, where matter and antimatter exhibit slightly different behaviour resulting in an excess of matter over antimatter. This is incorporated into the Standard Model through the Cabibo-Kobayashi-Maskawa (CKM) and Pontecorvo-Maki-Nakagawa-Sakata (PMNS) matrices [11–15], which describe the weak mixing between different generations of particles in the quark and neutrino sectors respectively.

Currently, a CP violating phase has only been measured in the quark sector and the value found does not result in a large enough asymmetry between matter and antimatter and so the Standard Model does not adequately explain the abundance of matter over antimatter. However, the CP violating phase in the neutrino sector has not been measured and may be large enough to account for this asymmetry.

In addition to CP violation, there are two other Sakharov conditions [16] that must be met in order to account for the matter-antimatter asymmetry. The first is that a B violating process must exist (i.e. baryogenesis) and the second is that interactions must take place outside of thermal equilibrium.

Dark Matter and Dark Energy

The field content of the Standard Model outlined in Table 1.1 only describes the particles that have been observed experimentally. However, it is known from galactic observations that these only contribute about 4% of the total mass-energy of the universe [17]. The remaining 96% is termed dark matter and dark energy which are introduced to explain several observed discrepancies in astronomy such as the

rotation curves of galaxies and the accelerating expansion of the universe. The true nature of both dark matter and dark energy is unknown to physicists and there is no clear indication as to whether they are new particles or some other problem with with our description of gravity and so are not included in the Standard Model.

Massless Neutrinos

The final problem with the Standard Model is the fact that it describes neutrinos as massless. This is in stark contrast to the observation of neutrino oscillations [18–20] which shows that neutrinos *do* have mass.

Since right-handed fermions exist in a weak singlet (i.e. they do not participate in the weak interaction) and, in the lepton sector, this singlet comprises of the charged lepton, no Higgs coupling can be written for neutrinos since this requires both a left-handed and a right-handed field and so neutrinos are massless in the Standard Model. However, it is possible to minimally extend the Standard Model by adding an extra right-handed fermion singlet that contains right-handed neutrinos in order to obtain the Higgs couplings. This then raises a few questions: why are neutrinos so much lighter than the other particles in the Standard Model and is the Higgs mechanism responsible for their mass?

Many extensions to the Standard Model implement neutrino masses in a different way to the Higgs mechanism by assuming that neutrinos are Majorana in nature (i.e. that they are their own antiparticles), this allows for Majorana mass terms to be added via the seesaw mechanism [21]. This results in light, left-handed neutrinos and heavy, right-handed neutrinos, whose mass could be at the GUT scale (10^{16} GeV). If these heavy, right-handed neutrinos existed at the beginning of the universe then they could undergo CP-violating decays to produce a lepton asymmetry, which could then produce a baryon asymmetry via sphaleron processes [22].

Since right-handed neutrinos cannot be directly produced at colliders, searching for their effects in neutrino oscillations, neutrinoless double beta decay ($0\nu\beta\beta$) and charged lepton flavour violation are now a priority.

1.2 Charged Lepton Flavour Violation

1.2.1 In the Standard Model

In the Standard Model, the quantity known as lepton flavour (L_e, L_μ, L_τ) is conserved, with leptons of a given flavour having a value of $+1$ and antileptons having a value of -1. The other lepton flavour numbers are 0 for both leptons and antileptons. As an example, the muon, μ^- has $L_\mu = +1$ and $L_e = L_\tau = 0$.

All conservation laws should, via Noether's theorem [23], have a corresponding underlying local symmetry (for example, conservation of momentum arises from the requirement that the laws of physics are translationally invariant). This is not the case for lepton flavour conservation which arises from an ad-hoc global symmetry of the form $U(1)_e \times U(1)_\mu \times U(1)_\tau$ and so is considered a symmetry that is not sacrosanct.

Indeed, when neutrino masses are added to the Standard Model, this conservation law is violated and so it is possible for leptons to change flavour. This has already been observed in the neutrino sector where neutrinos have been seen oscillating between flavours over long distances [18–20] and so opens up the possibility of observing lepton flavour violation (LFV) in the charged lepton sector. However, even with the addition of neutrino masses, the Standard Model prediction for the rate of charged lepton flavour violating (CLFV) processes is incredibly small, $\mathcal{O}(10^{-54})$ [24]. This means that, if the Standard Model is the only source of CLFV, then it would never be observed experimentally.

The reason for the Standard Model prediction being so small can be seen in Fig. 1.1, which shows the leading Feynman diagram for the CLFV decay $\mu \to e\,\gamma$. In this diagram, the incoming muon decays emitting a muon neutrino and a W boson, which gets reabsorbed after the neutrino oscillates into an electron neutrino and creates an electron.

Since the neutrino is essentially oscillating in a virtual loop (a much shorter length scale than the $\mathcal{O}$(km) that neutrinos have actually been observed oscillating over), this process is massively suppressed by a factor of $\frac{m^2_{\nu_i}}{M^2_W}$ as shown in Eq. 1.1 [24], where the equation for the branching ratio (BR) of this process is given. Here, U is the

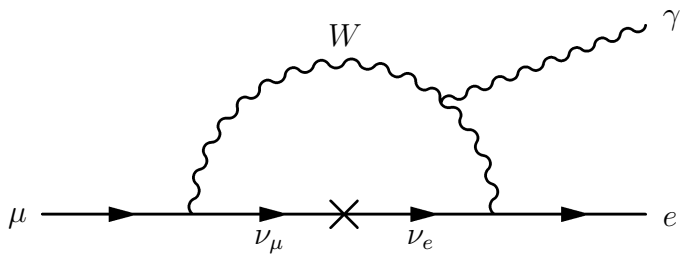

Figure 1.1: The Standard Model Feynmann diagram for the charged lepton flavour violating decay $\mu \to e\,\gamma$.

PMNS neutrino mixing matrix, α is the electromagnetic coupling constant and m_{ν_i} and M_W are the masses of the neutrinos and W boson respectively.

$$BR(\mu \to e\,\gamma) = \frac{3\alpha}{32\pi}\Big|\sum_i U^*_{\mu i}U_{ei}\frac{m^2_{\nu_i}}{M^2_W}\Big|^2 < 10^{-54}. \tag{1.1}$$

This minute Standard Model rate actually makes searches for CLFV processes very appealing since it means that there is no Standard Model background to take account of and so any observation would be clear evidence of physics beyond the Standard Model.

1.2.2 Beyond the Standard Model

Many extensions to the Standard Model predict enhanced rates of CLFV that could be observed by experiments in the near future. Obviously, if an observation of CLFV were to be made then that would lend some weight to these theories. However, a non-observation of CLFV would also restrict the large parameter spaces of these theories and possibly exclude them outright.

Because there are so many different theories that attempt to explain physics beyond the Standard Model, it is advantageous to parameterise them in a model independent way. A simple parameterisation, given in [24], considers the effective Lagrangian of Eq. 1.2, where the first term corresponds to a dipole-type operator (such as the one

in Fig. 1.1) and the second term corresponds to a four-fermion interaction between leptons and quarks.

$$\mathcal{L}_{CLFV} = \frac{m_\mu}{(\kappa+1)\Lambda^2}\bar{\mu}_R\sigma_{\mu\nu}e_L F^{\mu\nu} + \frac{\kappa}{(1+\kappa)\Lambda^2}\bar{\mu}_L\gamma_\mu e_L(\bar{u}_L\gamma^\mu u_L + \bar{d}_L\gamma^\mu d_L). \quad (1.2)$$

The parameters of this Lagrangian are Λ and κ, where Λ is the energy scale of the new interaction and κ is the ratio between the four-fermion and dipole-type interactions. For $\kappa \ll 1$, the dipole interaction dominates and for $\kappa \gg 1$, the four-fermion interaction dominates.

Fig. 1.2 and 1.3 show the parameter space for muon CLFV that has been excluded by previous experiments and also where any future experiments would probe were they to have the given sensitivity. There are two interesting things to note: first, is that CLFV searches can probe energy scales of $\mathcal{O}(10^4)$ TeV, which are much higher than can currently be directly probed at colliders. There is one caveat with this however, and that is that these values also depend on the mixing angles between the leptons and the coupling strength of the new interaction. The relationship between these three variables is shown in Eq. 1.3 and it is important to note that Fig. 1.2 assumes a coupling strength (g) on the same order as the weak interaction and maximal mixing between the leptons ($\theta_{e\mu} = 1$).

$$\text{Rate} \sim \frac{g\theta_{e\mu}}{\Lambda^2}. \quad (1.3)$$

The second thing to note from Fig. 1.2 is that an observation in a single channel would not give any indication as to the form of the new interaction. For example, if a signal was seen in $\mu - e$ conversion alone (see Sec. 1.3) with a branching ratio of 10^{-16} then the value of κ would not be known until a signal had been seen or excluded in $\mu \to e\,\gamma$ at a sensitivity greater than 10^{-14}. In addition, there is a connection to non-CLFV measurements such as the anomalous magnetic moment of the muon ($g_\mu - 2$), whose loop diagrams are similar to those of CLFV processes. The value of muon $g - 2$ has been measured to be 3.6σ from the Standard Model prediction [25] and so a more precise measurement could provide further information

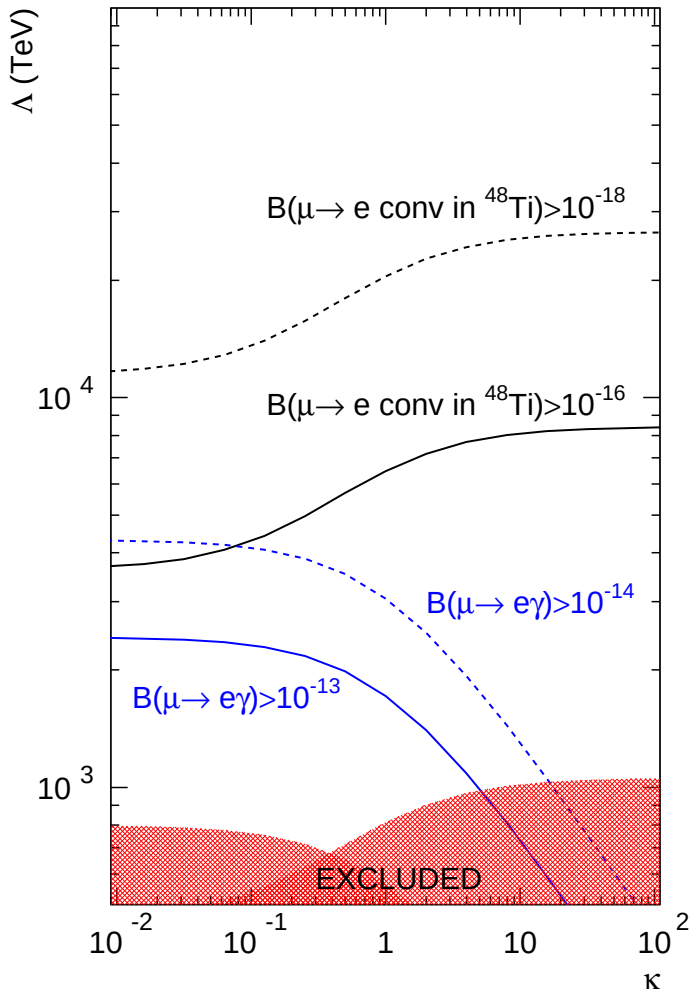

Figure 1.2: The current and hypothetical limits of $\mu \to e\,\gamma$ and $\mu - e$ conversion in terms of the two parameters Λ and κ (Eq. 1.2), where Λ is the energy scale of the new interaction and κ is the ratio between the four-fermion and dipole-type interactions. $\kappa \ll 1$ means that the dipole interaction dominates and $\kappa \gg 1$ means that the four-fermion interaction dominates [24]. The model assumes that $g \approx g_W$ and $\theta_{e\mu} = 1$. The lines show the parameter space the would be excluded were a future experiment to have the given sensitivity.

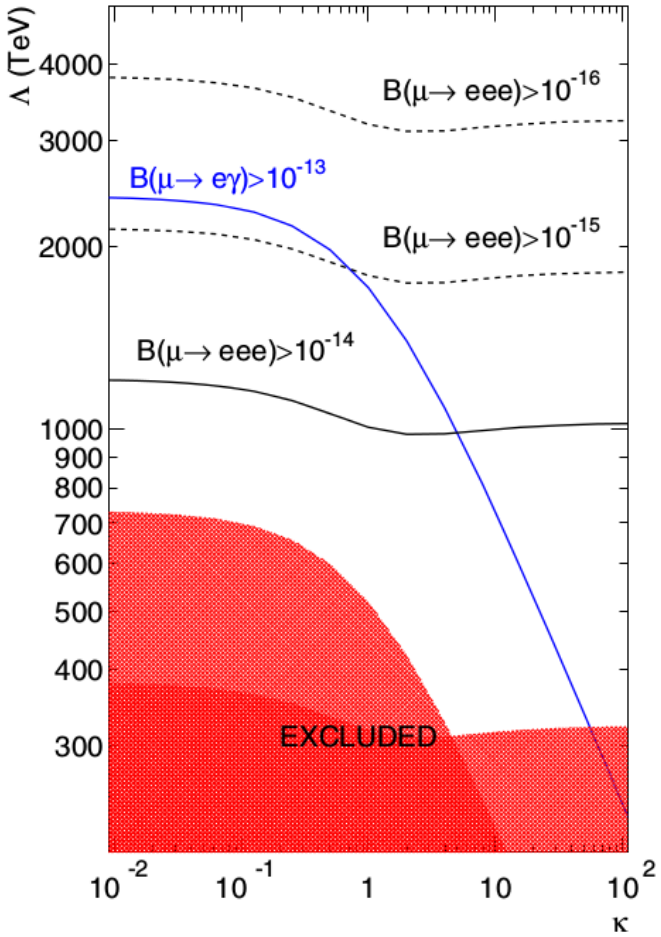

Figure 1.3: The current and hypothetical limits of $\mu \to e\,\gamma$ and $\mu \to e\,e\,e$ in terms of the two parameters Λ and κ (Eq. 1.2 with u_L and u_D replaced with e_L), where Λ is the energy scale of the new interaction and κ is the ratio between the four-fermion and dipole-type interactions. $\kappa \ll 1$ means that the dipole interaction dominates and $\kappa \gg 1$ means that the four-fermion interaction dominates [24]. The model assumes that $g \approx g_W$ and $\theta_{e\mu} = 1$. The lines show the parameter space the would be excluded were a future experiment to have the given sensitivity.

to the mechanism of the new interaction. Therefore, a complete set of searches needs to be performed in as many channels as possible in order to determine the mechanism of CLFV, in the event of a non-null measurement.

1.2.3 Experimental Searches

The experimental search for CLFV has been ongoing ever since Hincks and Pontecorvo's first attempt to find $\mu \to e\,\gamma$ in 1947 [26]. Nowadays, searches are made in the muon, tau and meson sectors where processes such as $\mu \to e\,\gamma$, $\tau \to \mu\gamma$ and $K_L^0 \to \mu e$ could be observed. In this section, only searches in the muon sector will be described.

There are three possible CLFV muon decays: $\mu \to e\,\gamma$, $\mu \to e\,e\,e$ and $\mu - e$ conversion. A full history (and future) of the searches for each of these decay modes is shown in Fig. 1.4 and the current best experimental limits are given in Table 1.2. From this plot it is clear that increases in experimental sensitivity have been getting smaller and smaller and it is only with the new generation of experiments that a large leap in sensitivity (by a few orders of magnitude) is achievable.

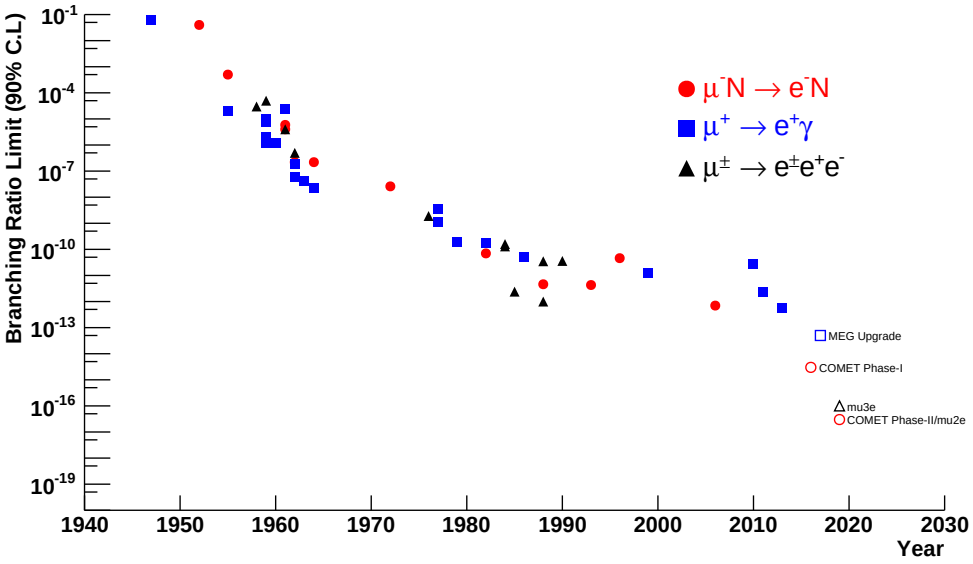

Figure 1.4: The history [27] (filled) and future [28–31] (unfilled) of CLFV searches in the muon sector.

CLFV Process	Current Limit	Experiment	Reference
$\mu^+ \to e^+ + \gamma$	$< 5.7 \times 10^{-13}$	MEG	[32]
$\mu^+ \to e^+ + e^- + e^+$	$< 1.0 \times 10^{-12}$	SINDRUM	[33]
$\mu^- + \mathrm{Au} \to e^- + \mathrm{Au}$	$< 7 \times 10^{-13}$	SINDRUM-II	[34]

Table 1.2: The current limits in muon CLFV searches at 90% confidence level.

The experimental method for each of these rare muon decay searches is the same - large numbers of muons are brought to rest and allowed to decay. Since the muon is stopped, it is in a well known initial kinematic state (all the energy is in its mass) and so the kinematics of the decay products are well defined. Therefore, each rare decay has a very specific signature to search for.

For example, the $\mu \to e\,\gamma$ process has two products and so is described by a two body decay, where the positron and photon must carry half of the energy each and be emitted back-to-back at the same time. Therefore, $\mu^+ \to e^+\,\gamma$ searches try to find a positron and a photon of 52.8 MeV ($\frac{m_\mu}{2}$) at 180° to each other and that have been produced at a common vertex. It is a similar situation for the $\mu^+ \to e^+\,e^-\,e^+$ search where the signal is two positrons and an electron with a combined energy of the muon mass arising from a common vertex. Finally, the $\mu - e$ conversion process has a very simple signal of a monoenergetic electron with an energy roughly equivalent to the mass of the muon.

In order to achieve the increases in sensitivities that are planned, highly-intense muon beams are required. This can be a problem for the $\mu^+ \to e^+\,\gamma$ and $\mu^+ \to e^+\,e^-\,e^+$ searches since their main backgrounds are the result of accidental coincidences. For example, in $\mu \to e\,\gamma$, an accidental coincidence will occur if two muons decay close to each other and one of the produced electrons radiates a photon. The rate of these is given by Eq. 1.4, where B_{acc} is the rate of accidental background events normalised to the total decay rate, R_μ is the muon rate, ΔE_e is the resolution on the positron energy, ΔE_γ is the uncertainty on the photon energy, $\Delta\theta_{e\gamma}$ is the uncertainty on the angle between the positron and the photon and $\Delta t_{e\gamma}$ is the uncertainty on the time difference between the positron and the photon [35]. To overcome this challenge, high resolution position and timing measurements are needed but the efficacy of

these overcoming the accidental backgrounds gets progressively worse as the muon beam intensity increases.

$$B_{acc} \propto R_\mu \Delta E_e \Delta E_\gamma^2 \Delta\theta_{e\gamma}^2 \Delta t_{e\gamma}. \tag{1.4}$$

However, an increase in muon beam intensity is not as much of a problem for $\mu - e$ conversion searches since no coincidences need to be found and so large, order-of-magnitude increases of sensitivity are possible with similar increases in muon beam intensity. This is the process that COMET will be searching for.

1.3 $\mu - e$ Conversion

1.3.1 Signal

In $\mu - e$ conversion experiments, muons are fired at a stopping target, where they are stopped and form muonic atoms. The muons then immediately fall into the $1s$ ground state emitting photons in the process. Finally, the muon can then interact coherently with the whole nucleus and, in the case of $\mu - e$ conversion, will transform into a single electron with a well-defined energy. The formula for this energy is given by Eq. 1.5, where m_μ is the muon mass, E_b is the binding energy of the $1s$ state of the muonic atom ($\approx \frac{Z^2\alpha^2 m_\mu}{2}$) and E_{rec} is the recoil energy taken by the nucleus ($\approx \frac{E_\mu^2}{2m_N}$, where m_N is the mass of the nucleus). For aluminium ($Z = 13$), the signal energy is 104.96 MeV and for gold ($Z = 79$) it is 95.56 MeV.

$$E_e = m_\mu - E_b - E_{rec}. \tag{1.5}$$

It is worth mentioning that the $\mu - e$ conversion process has a Z dependence because the conversion process as a whole scales as Z^5 (the interaction itself scales by Z^2 and then the probability of the wavefunctions overlapping scales as Z^3). Since the branching ratio is normalised to the rate of muon capture (proportional to Z^4) the rate of the $\mu - e$ conversion process scales linearly in Z and so a high-Z

material would be preferred. However, in order to reduce certain backgrounds (see Sec. 1.3.4), experiments will record data some time after the beam has been injected (see Sec. 2.2.5) and so there is a competing requirement of having a long muonic atom lifetime, which means that low-Z materials are preferred. Taking these considerations into account, the search for the $\mu - e$ conversion process will initially be conducted using an aluminium target, with the possibility that other materials will be investigated at a later data since the rate of a given CLFV operator has a Z-dependence as shown in Fig. 1.5.

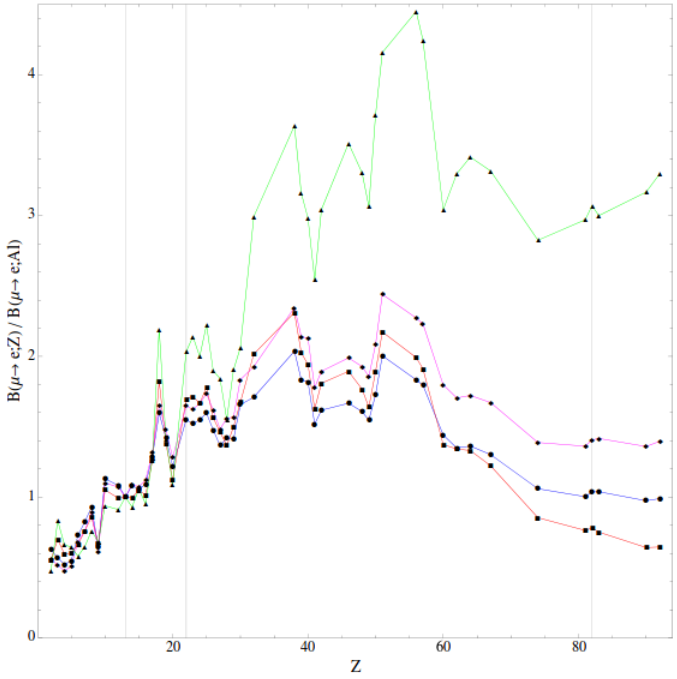

Figure 1.5: A plot of the Z-dependence of the $\mu - e$ conversion rate (normalised to aluminium) for different single-operator models [36]: dipole (blue), scalar (red) and two vector models: γ-mediated (magenta) and Z-mediated (green). The vertical lines correspond to aluminium, titanium and lead nuclei.

1.3.2 Branching Ratios and Sensitivities

The definition of branching ratios used in $\mu - e$ conversion searches is slightly different to that in other areas of physics. In general, the branching ratio of a process is the fraction of times that a particle will undergo that process out of all possible processes that can occur. In $\mu - e$ conversion searches (as shown in Eq. 1.6) the number of

$\mu - e$ conversion events is normalised to the number of muon captures rather than the total number of decays.

$$\mathrm{BR}(\mu - e \text{ conversion}) = \frac{n(\mu^- + N(Z,A) \to e^- + N(Z,A))}{n(\mu^- + N(Z,A) \to \nu_\mu + N(Z-1,A))}. \tag{1.6}$$

The definition of the single event sensitivity (S.E.S) used by COMET is shown in Eq. 1.7, where $N_{\mu-stop}$ is the total number of stopped muons, f_{cap} is the fraction of stopped muons that are captured (this depends on the nucleus and for aluminium, $f_{cap} = 0.601$ [37]), and ε is the efficiency of the experiment. This value corresponds to the branching ratio for one expected signal event and no background and so is, in essence, the best possible measurement COMET could make.

$$\mathrm{S.E.S} = \frac{1}{N_{\mu-stop}\, f_{cap}\, \varepsilon}. \tag{1.7}$$

COMET will achieve a S.E.S of 3×10^{-17} and this is related to the 90% CL of a null result by a factor of $-\ln(0.1) = 2.3$ and so the 90% CL branching ratio limit that COMET would make, were it to see no signal events, would be 6.9×10^{-17}.

1.3.3 Current Limit

The current best experimental limit of the branching ratio for $\mu - e$ conversion was set by SINDRUM-II on gold in 2006 and is $< 7 \times 10^{-13}$ at 90% CL [34]. COMET is aiming for a final single event sensitivity (S.E.S) of 3×10^{-17}, which is a four order of magnitude improvement.

Previous searches have focused on using high-Z materials since the rate of the $\mu - e$ conversion process is proportional to Z. However, in order to achieve the necessary increases in sensitivity, pulsed muon beams must be used (see Sec. 2.2.1) and so materials with a long muonic atom lifetime are preferred and this is one of the reasons why COMET has chosen an aluminium stopping target. However, this introduces a subtlety when comparing an aluminium limit with a gold limit since they have

different sensitivities to any new interaction because of the Z-dependence of the $\mu - e$ conversion process.

The SINDRUM-II result [34] is shown in Fig. 1.6, where the grey histogram is the simulation of the main background to $\mu - e$ conversion (muon decay-in-orbit (DIO): see Sec. 1.3.4), the dashed line is the simulation of the $\mu - e$ conversion signal and the data points are the measurements of electrons or positrons. The positrons arise from radiative pion capture background, which is charge symmetric.

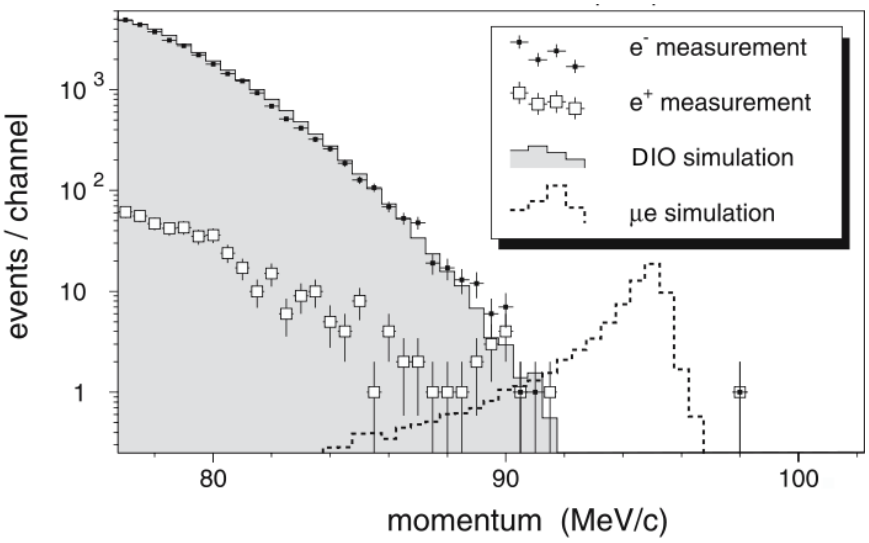

Figure 1.6: A plot of the electron energy from the SINDRUM-II experiment [34].

This plot demonstrates how important high-resolution measurements are to the $\mu - e$ conversion search, since this determines the overlap between the background and a potential signal. It also shows the importance of knowing all the background processes since there is a data point that was measured above the signal energy which doesn't match either of the simulated processes.

1.3.4 Backgrounds

As with any rare search experiment, it is incredibly important that all backgrounds are understood, accounted for and mitigated. For $\mu - e$ conversion, there is no Standard Model background but there are other processes that could obscure or mimic a signal and these are split into the following categories:

Intrinsic Physics Backgrounds

These arise from muons stopping in the stopping target and cannot, therefore, be removed completely. The way to mitigate their effect is to have a high resolution detector since, neglecting resolution effects, there are no intrinsic physics backgrounds that have the same energy as the $\mu - e$ conversion signal energy.

Beam-related Prompt Backgrounds

These arise from contamination of the muon beam causing electrons with an energy close to or in the signal region to be created. By pulsing the muon beam, the impact of these are greatly reduced by only recording data in a delayed time window (see Sec. 2.2.1). However, these prompt backgrounds could still cause a problem if there are particles leaking out of the main pulses and into the gaps between them. Therefore, a high level of "extinction" of secondary proton pulses (see Eq. 2.1) is required to achieve the design sensitivity.

This contamination chiefly comes from three sources. Firstly, pions that have not decayed by the time the beam reaches the stopping target can be captured immediately by the nucleus (see Sec. 1.3.4 below). Secondly, high energy electrons can come directly from pion decays which, despite having a small branching ratio (1.23×10^{-4}), are important for the high intensity beams that will be used. Finally, muons can decay in flight and, if they have a momentum greater than 77 MeV/c, then the boost to the lab frame is enough for an electron with the maximum momentum in the centre-of-mass frame (52.8 MeV/c if the neutrinos are emitted in the same direction) to have an energy in the 104.96 MeV signal region.

Beam-related Delayed Backgrounds

These are backgrounds that are from the main proton pulse but which arrive at the stopping target section late (for example, antiprotons or neutrons) and are reduced by having a sufficiently long muon beam line and using a delayed time window measurement.

Other Backgrounds

The main cause of other backgrounds is cosmic rays, which can induce a background event in the detector but can easily be accounted for by using a cosmic ray veto.

A table showing the COMET Phase-I background estimates is shown in Table 1.3 and the most important ones are described in the following sections.

Type	Background	Estimated events
Physics	Muon decay in orbit	0.01
Physics	Radiative muon capture	5.6×10^{-4}
Physics	Neutron emission after muon capture	< 0.001
Physics	Charged particle emission after muon capture	< 0.001
Prompt Beam	Beam electrons (prompt)	8.3×10^{-4}
Prompt Beam	Muon decay in flight (prompt)	$\leq 2,0 \times 10^{-4}$
Prompt Beam	Pion decay in flight (prompt)	$\leq 2.3 \times 10^{-3}$
Prompt Beam	Other beam particles (prompt)	$\leq 2.8 \times 10^{-6}$
Prompt Beam	Radiative pion capture(prompt)	2.3×10^{-4}
Delayed Beam	Beam electrons (delayed)	~ 0
Delayed Beam	Muon decay in flight (delayed)	~ 0
Delayed Beam	Pion decay in flight (delayed)	~ 0
Delayed Beam	Radiative pion capture (delayed)	~ 0
Delayed Beam	Anti-proton induced backgrounds	0.007
Others	Electrons from cosmic ray muons	< 0.0001
Total		0.019

Table 1.3: Table of the COMET Phase-I estimated background events for a single-event sensitivity of 3.1×10^{-15} and a proton extinction factor of 3×10^{-11} [29].

Decay In Orbit

The decay-in-orbit (DIO) process is the most important intrinsic physics background process to the $\mu - e$ conversion search and occurs when a stopped muon decays via its normal Michel decay to an electron and two neutrinos ($\mu^- \rightarrow e^- \nu_\mu \overline{\nu}_e$).

Normally, in a free muon decay, the electron energy would not exceed 52.8 MeV, which occurs when the electron and two neutrinos are emitted in opposite directions and is equal to half of the mass of the muon. However, in the case of DIO, the decay is occuring when the muon is in a muonic atom. This means that the nucleus

can take away some of the momentum which, being non-relativistic, means it can take momentum out of the system without taking any significant energy. Therefore, electrons can essentially recoil off the nucleus and thus have more energy than the free muon decay limit. Even so, the electrons cannot take all of the energy (the two neutrinos will take some) and so the end point of the DIO spectrum is slightly lower than the $\mu - e$ conversion signal energy of 104.96 MeV.

The DIO electron energy spectrum has been calculated by Czarnecki et al. [38–40] and is shown in Fig. 1.7. It can be seen that the spectrum falls very sharply after 52.8 MeV (as $\frac{1}{m_\mu{}^5}$) and appears to vanish at 60 MeV (Fig. 1.7a). However, looking at the DIO spectrum on a log scale (Fig. 1.7b), it can be seen that the occurrence of DIO electrons above 100 MeV is still at an appreciable level relative to a signal with a branching ratio of $\mathcal{O}(10^{-17})$. This is further complicated by the detector resolution which could measure a DIO electron with a higher energy than it truly has and so in order to minimise the impact of this background, COMET will use a high-resolution detector (see Sec. 2.2.6 and Sec. 2.2.8).

Nuclear Muon Capture

Another intrinsic background process that can occur when the muon has formed a muonic atom is that the muon can be captured by a proton in the nucleus ($\mu^- p \to \nu_\mu n$). This is not a background process in the sense that it could mimic a $\mu - e$ conversion signal electron. Rather, this process can leave the nucleus in an unstable configuration and, upon falling to the ground state, will emit particles that enter the detectors.

For example, any protons emitted can generate hits in the detector which could be included in track finding algorithms and bias the momentum measurement. In addition, if the flux of protons is too high, the DAQ system could get flooded and result in significant dead time, reducing the efficiency and, hence, sensitivity of the experiment.

Similarly, any neutrons emitted will travel straight out of the experiment and penetrate enough material to trigger multiple layers of the cosmic ray veto and thus cause deadtime. Also, they can interact with material in the experiment to produce

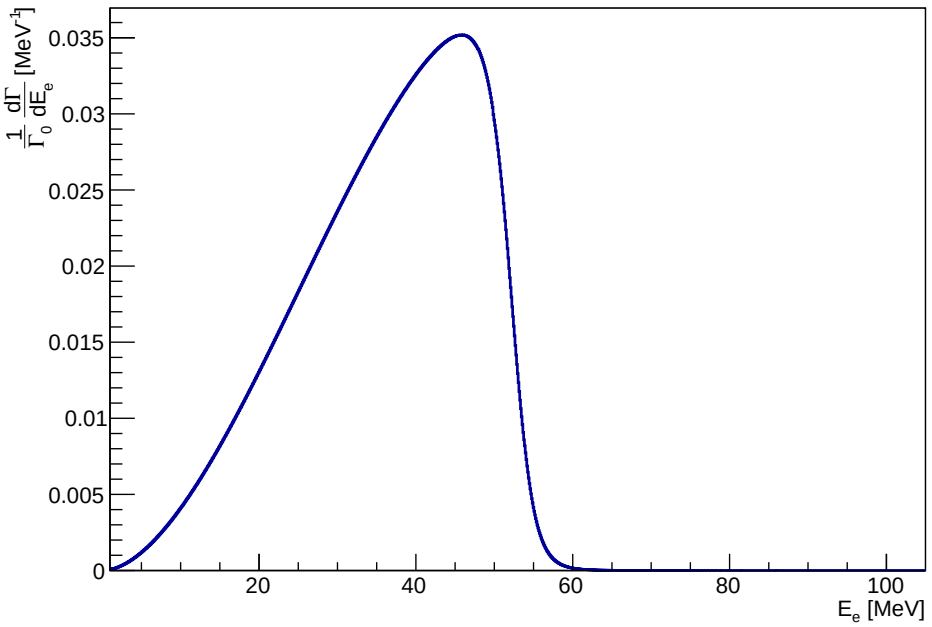

(a) linear scale

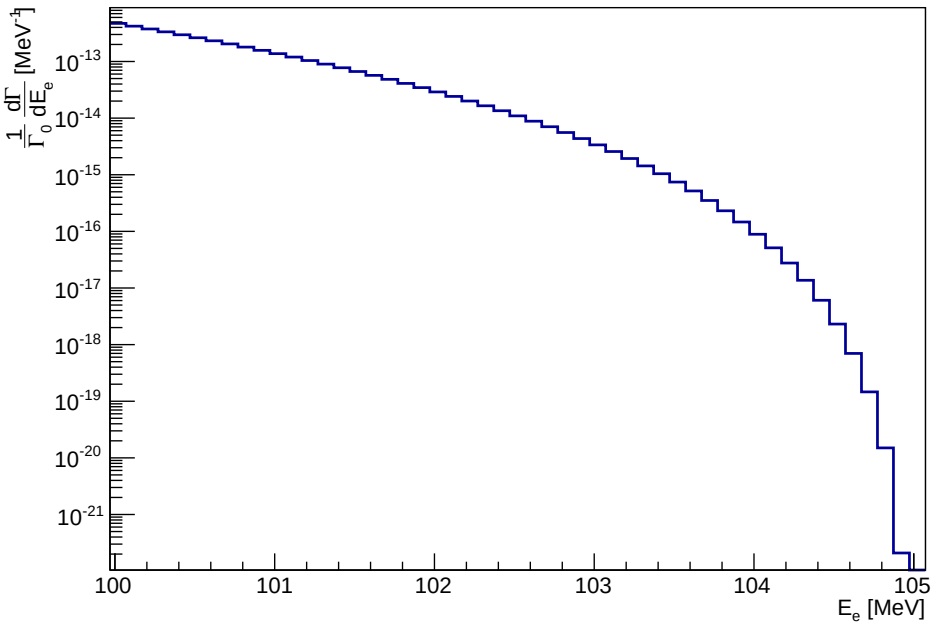

(b) log scale (zoom in)

Figure 1.7: The energy spectrum of DIO electrons calculated by Czarnecki et. al. The theoretical uncertainties are not larger than the target accuracy of the calculation and so are ignored [38–40].

high energy photons, which can pair produce to create high energy electrons that may have an energy in the signal region.

The exact nature and composition of the emitted particles is incredibly important in designing COMET and so data for this would be extremely valuable. Therefore COMET, along with the MU2E collaboration (FNAL), joined together to perform the ALCAP experiment which is described in detail in Ch. 4.

Radiative Pion Capture

The largest beam-related prompt background is radiative pion capture. This process occurs because of pion contamination in the muon beam, which will also stop in the stopping target (see Sec. 2.2.5). Once the pions are stopped, they are immediately captured by the nucleus, which is left in an excited state. Then, as the nucleus falls back down to the ground state, it emits high energy photons that can pair produce in the stopping target region and could have an energy in the signal region.

As with all prompt backgrounds, radiative pion capture is first reduced by using a pulsed muon beam and collecting data in a delayed time window (see Sec. 2.2.1). This greatly reduces the problem in the main proton pulses but if there are any pions arriving at the stopping target between pulses, due to protons between the main pulses, then the delayed time window does not help and thus it is important to maintain a high level of "proton extinction" (see Sec. 2.2.1).

Antiproton Induced Backgrounds

Antiprotons are an important background because they travel slowly and are one of the few backgrounds that would not be eliminated by any charge selection. This means that any electrons that are produced as the antiprotons interact with parts of the experiment (which could have an energy in the signal region) could arrive at the stopping target between the main proton pulses. In addition, without any dE/dx information, antiprotons cannot be distinguished from electrons in a tracker-only experiment.

Antiprotons are produced at the pion production target and there is a threshold below which none are produced. This is at a kinetic energy of 5.6 GeV and so COMET would

ideally run at a lower proton beam energy. However, there are other considerations that need to be taken into account such as the pion production cross-section and the dispersion of the beam (see Sec. 2.2.1) and so COMET will run at a slightly higher kinetic energy of 8 GeV. In order to remove the antiprotons, an antiproton absorber will be placed in the beampipe to stop them.

Chapter 2

The COMET Experiment

"Approach junction - it provides a long tail back (5)"
— Dante, *Financial Times #14679*

2.1 Overview

The COherent Muon to Electron Transition (COMET) experiment will search for the charged lepton flavour violating process $\mu^- + N(Z, A) \rightarrow e^- + N(Z, A)$ in aluminium with a single event sensitivity (S.E.S) of 3×10^{-17}. This will be an improvement of four orders of magnitude on the current limit set by SINDRUM-II in 2006 [34].

COMET is being built at the Japan Proton Accelerator Research Complex (J-PARC) near Tokai and will be constructed in two stages with physics analysis being done in both. The first phase (Phase-I) has already begun construction and will take data for four months in 2017 to achieve a S.E.S of 3×10^{-15}. The second phase (Phase-II) will begin construction immediately after Phase-I has finished running and will run for at least a year in 2020 to reach the final goal of 3×10^{-17}.

2.2 Experimental Layout

The experimental layouts of both the Phase-I and Phase-II experiments are shown in Fig. 2.1 and Fig. 2.2 respectively. As can be seen, Phase-II will have a distinctive S-shape and Phase-I will be identical to Phase-II up to the end of the first 90° bend.

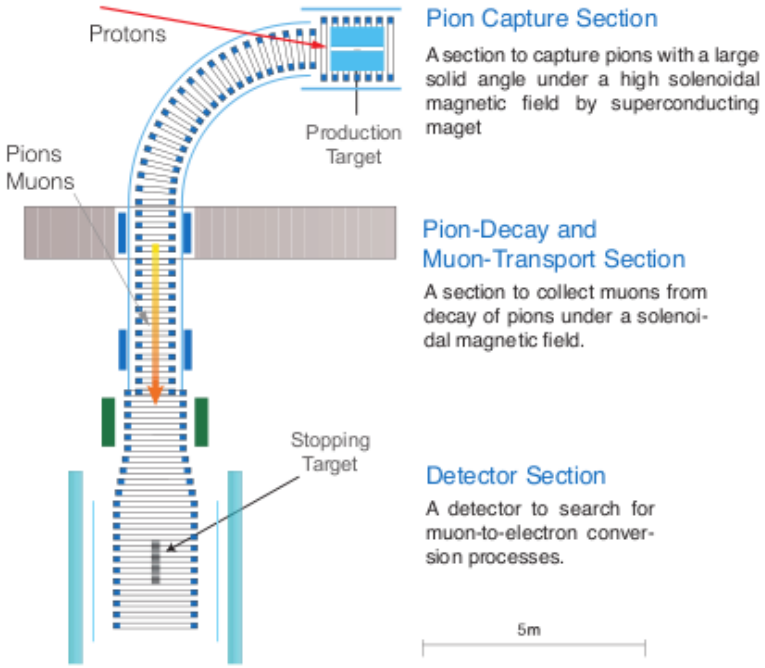

Figure 2.1: The experimental layout of COMET Phase-I [29].

In order to achieve the target sensitivity, COMET will use one of the highest intensity muon beams in the world. In general, muon beams are created by firing protons at a production target to create pions that will then decay to muons – COMET is no different in this regard (Sec. 2.2.1 and Sec. 2.2.2). However, in order to get the intensities required, COMET will be utilising a novel pion capture system that uses a large solenoidal magnetic field to collect particles emitted from the production target. The high magnetic field means that particles are travelling in tight spirals and so, geometrically, more particles can be accepted than if a lower strength magnetic field is used creating looser helices. This is based on the design of Dzhilkibaev and Lobashev for the MELC experiment [41] (Sec. 2.2.3).

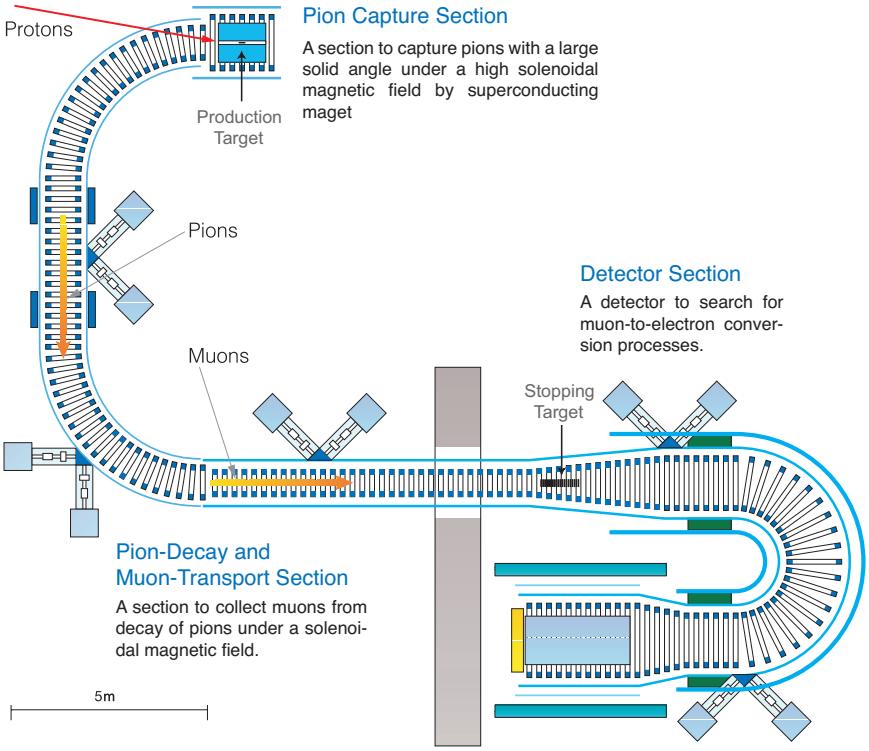

Figure 2.2: The experimental layout of COMET Phase-II [29].

The beam of particles from the production target will contain far more pions than muons and so the beam has to travel far enough so that the majority of the pions decay to muons, which greatly reduces the radiative pion capture background described in Sec. 1.3.4. This is achieved in the transport section leading to the muon stopping target, which will be a 90° bend for Phase-I and extended to a 180° bend for Phase-II (Sec. 2.2.4).

Once the muons reach the stopping target section, they will stop in the stopping target (Sec. 2.2.5) where the muonic aluminium atoms are formed and the $\mu - e$ conversion process can occur. The stopping target is designed so that as many muons as possible are stopped whilst also ensuring that the emitted electrons lose as little energy as possible in order to prevent the signal electrons smearing into the background.

Finally, after the electrons have been emitted from the stopping target, their energies need to be measured. For Phase-I, this will be done by the Cylindrical Detector (CyDet), which consists of a Cylindrical Drift Chamber (CDC) and two Cherenkov

counters and allows for a greater geometrical acceptance, but poorer resolutions, than in Phase-II (Sec. 2.2.6). For Phase-II, the emitted electrons are first transported around a final C-section for momentum selection (Sec. 2.2.7) and then measured by a detector consisting of a straw tube tracker and electromagnetic calorimeter called the StrECAL (Sec. 2.2.8). Phase-I will also use a prototype StrECAL to measure and characterise backgrounds for Phase-II.

2.2.1 Proton Beam

As already mentioned, COMET will create a muon beam by firing a proton beam at a production target. The important properties of the proton beam are that it will have an energy of 8 GeV, a pulsed time structure, a beam power of 3.2 kW (56 kW) in Phase-I (Phase-II) and will be slow extracted from the Main Ring (MR) at J-PARC.

Pulsed Time Structure

The reason for using a pulsed beam is to ensure that measurements can be made in a delayed timing window so that the effect of prompt backgrounds is reduced. This is illustrated in Fig. 2.3 where the main proton pulses are in grey and spaced 1.1 μs apart and the prompt background, decay of stopped muons and signal processes are shown in blue, red and black respectively. It can then be seen that, if a measurement is taken in a delayed timing window (green), the electrons resulting from prompt backgrounds will have already passed through the experiment and so their impact is greatly reduced. In order to maintain this time structure, COMET will be using the MR in bunched slow extraction mode.

However, the delayed time window does not reduce prompt backgrounds from protons that arrive between the main pulses (see, for example, the smaller, grey proton pulse in the centre of Fig. 2.3). This means that the extinction of the proton beam (as defined in Eq. 2.1) is critical and if it is greater than 10^{-8}, then the resulting prompt background from these protons reduces the experiment's S.E.S as shown in Fig. 2.4. Below an extinction factor of 10^{-8}, the S.E.S is dominated by intrinsic physics backgrounds which cannot be reduced using extinction. Therefore, an extinction of at least 10^{-8} is required for COMET Phase-I to achieve its target sensitivity.

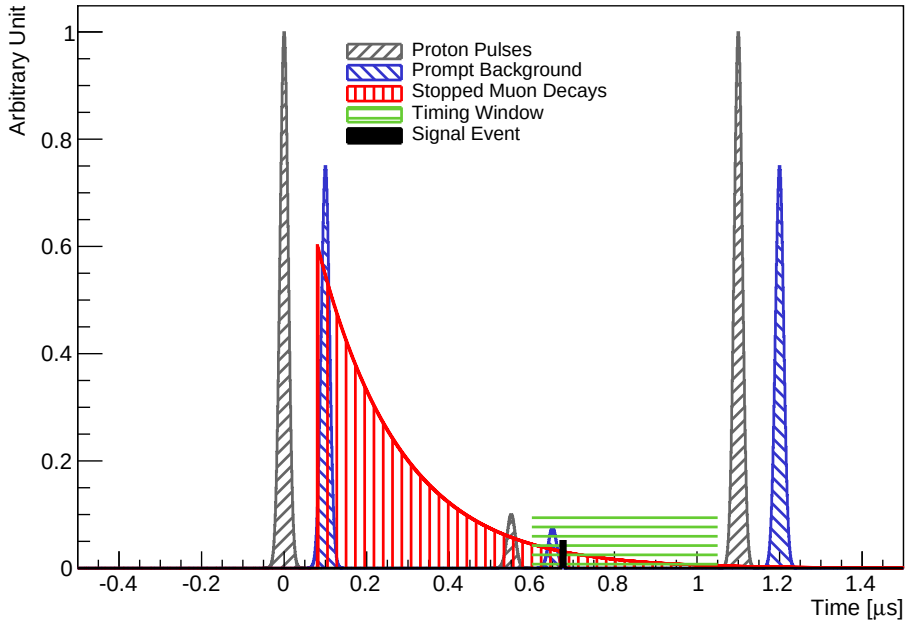

Figure 2.3: A schematic of the time structure of the proton beam. The two large grey peaks show the main proton pulses in alternate buckets and the small grey pulse in the centre of the plot shows any protons that have not been extinguished.

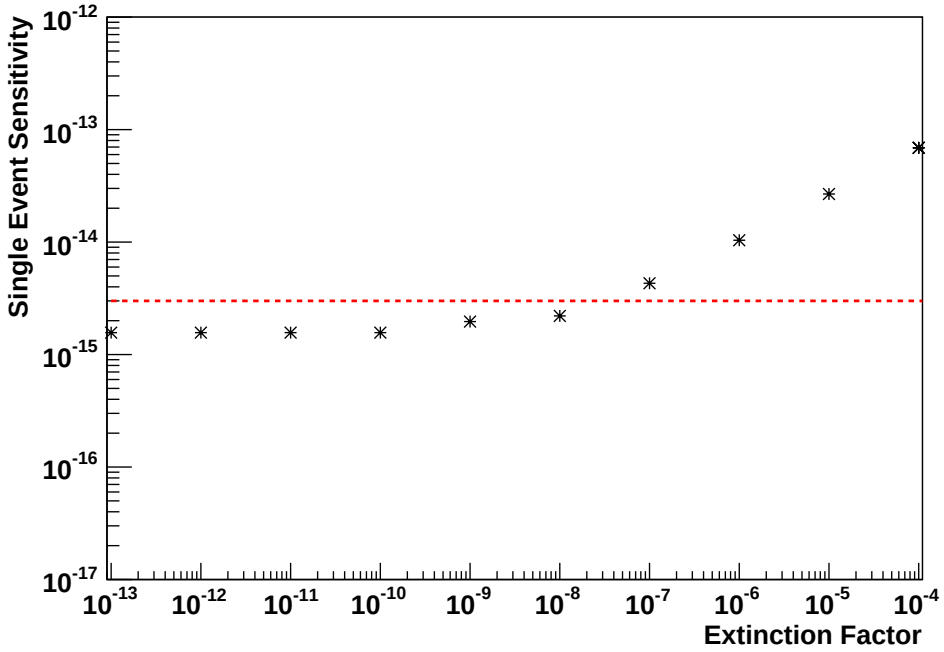

Figure 2.4: A plot of the single event sensitivity for different extinction factors. The red line corresponds to the Phase-I design sensitivity of 3×10^{-15}.

$$\text{Extinction} = \frac{\text{number of protons between pulses}}{\text{number of protons in main pulse}}. \tag{2.1}$$

A new extinction method has been demonstrated at the J-PARC Main Ring and has shown that an extinction of $\mathcal{O}(10^{-11})$ should be possible. Usually, the previous acceleration stage has half of its buckets filled with a significant number of protons in the "empty" buckets. Then, when both buckets are injected into the MR, a secondary kick is administered after a single turn to clean the "empty" bucket. This is improved in the new method by delaying the initial kick by half a turn so that the "empty" bucket never enters the MR thus ensuring a much higher extinction rate.

Beam Energy

There are a few considerations in deciding on the energy of the proton beam. First, in order to remove the antiproton background (see Sec. 1.3.4), a proton beam energy

below the 5.6 GeV production threshold would be required. A lower energy beam is also favoured by the fact that it is easier to perform extinction kicks at lower energies. However, the emittance of the beam[1] needs to be low enough so that the proton pulses can be extracted safely from the MR and this is easier to do at higher energies. Therefore, COMET has opted to use an 8 GeV proton beam, since this is the lowest energy that can be safely extracted.

Beam Power

COMET will not be the only experiment using the J-PARC MR and, due to the differing requirements of the other experiments, COMET cannot run at the same time as them. Therefore, in order to make best use of the beam time it is given, COMET will be running at a relatively high beam power of 3.2 kW for Phase-I and 56 kW for Phase-II.

2.2.2 Pion Production Target

For Phase-I, COMET will be using a graphite target of radius 20 mm, length 600 mm and rotated at a 10° angle to the muon beam direction in order for the proton beam to be injected.

For Phase-II, the material of the production target may change to tungsten, which has a larger pion production cross-section due to its larger atomic number. The reason that tungsten is not being used for Phase-I is because it requires a sophisticated cooling system. This is still being developed and will be completed for Phase-II.

2.2.3 Pion Capture System

In order to create one of the most intense muon beams in the world, COMET will be using a pion capture system to collect the pions and muons that are produced from the protons hitting the production target.

The idea of a pion capture system was first proposed by Dzhilkibaev and Lobashev for the MELC experiment [41], which would have also searched for $\mu - e$ conversion,

[1] a measure of its size

and works by applying a large solenoidal magnetic field[2] across the pion production target section. The particles are then guided by this magnetic field backward (w.r.t. the incoming proton beam) and into the muon transport section. This system has already been demonstrated at MUSIC in Osaka [42].

In general, low momentum pions are preferred because these will decay to low momentum muons which can be stopped by the stopping target. High momentum muons are not desirable because when they decay in flight they could produce electrons in the signal region. The pion capture system achieves this by preferentially collecting pions emitted in the backward direction and only forward-going pions that have a low transverse momentum. The actual yield of muons from this system is not well known since there is little experimental data of pion production in the backwards region. Therefore, a study of hadron production is required and this is presented in Ch. 3 and reducing this uncertainty will be one of the goals of COMET Phase-I.

2.2.4 Muon Transport Section

Once the pions have been produced, they will start decaying to muons that will be stopped in the stopping target. In order to reduce the amount of pion contamination in the beam, a sufficiently long muon transport section is needed. In addition, charge and momentum selection can be performed if the muon transport section is curved. This means that the preferred negative, low momentum muons can be extracted and background sources can be greatly reduced.

For these reasons, the muons will be transported around a toroidal channel of radius 3 m before entering the stopping target section. For Phase-I, the torus will be 90° and for Phase-II, this will be extended to 180°. In addition to this, for Phase-I there will be a long collimator at the end of 90° that will be thick enough to stop all pions and positioned so that high momentum muons are stopped. This is necessary because of the shorter muon transport section.

[2] for reference, COMET will use capture solenoids with a peak magnetic field strength at the target of 5 T

2.2.5 Stopping Target

The muon stopping target is where the muons will stop and possibly undergo the $\mu - e$ conversion process. COMET will be searching for this process in aluminium because it has a sufficiently long muonic atom lifetime of 864 ns [43] so that a delayed time window measurement will be effective. Although a high-Z material would have a larger relative cross-section for $\mu - e$ conversion, these materials have muonic atom lifetimes that are too short to make the timing window a viable method.

The geometrical design of the stopping target is determined by two requirements. First, the target must stop as many muons that enter the stopping target region as possible (the stopping efficiency). And secondly, the energy loss of electrons leaving the target must be minimal in order to avoid the 104.96 MeV signal electrons merging into the DIO background. These two requirements are conflicting in that a thicker target has a higher stopping efficiency but also reduces and smears the energy of the electrons more.

An optimisation of the geometrical design has been performed and resulted in a stopping target of 17 aluminium disks spaced 50 mm apart to be chosen. The current design parameters of which are summarised in Table. 2.1 [29].

Material	aluminium
Shape	flat disk
Radius	100 mm
Thickness	200 μm
Number of disks	17
Disk spacing	50 mm

Table 2.1: The parameters of the muon stopping target for COMET [29].

2.2.6 Cylindrical Detector

The Cylindrical Detector (CyDet) is the detector that will be used in Phase-I for the $\mu - e$ conversion search and consists of a Cylindrical Drift Chamber (CDC) to

measure the momentum of the electrons and a pair of Cherenkov counters to provide a trigger. A schematic of the layout is given in Fig. 2.5.

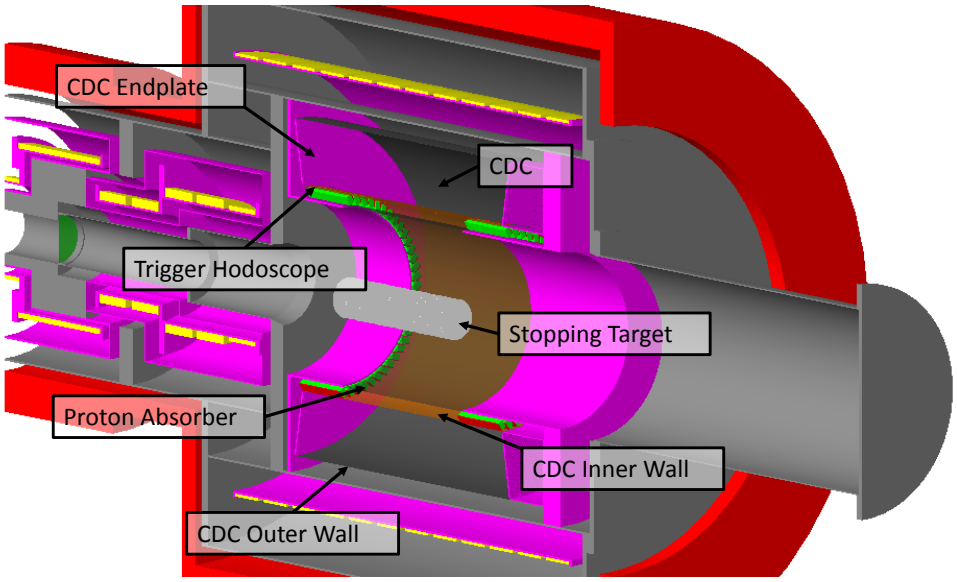

Figure 2.5: A schematic of the CyDet [29].

Having a cylindrical detector around the stopping target gives a greater geometrical acceptance to the signal, but also means that any other particles emitted from the stopping target (for example, protons from nuclear muon capture described in Sec. 1.3.4) will enter the detector volume and affect the data rates or even mimic hit patterns that get mistaken for electrons in track finding algorithms.

The requirements of the CDC are that it needs to have a gas gain of greater than 10^5, a position resolution in the transverse plane of less than 250 μm, a position resolution in the z direction of less than 2 mm and a drift gas with low multiple scattering in order to minimise the amount of energy loss and achieve a momentum resolution of $\mathcal{O}(200$ keV) and a track reconstruction efficiency of 80% [29].

There are two important parameters that help in the reduction of the backgrounds. First, the inner radius of the CDC needs to be large enough so that the high flux of low p_T electrons from muon decay-in-orbit do not enter the detector and, second,

the inner wall needs to be thick enough to stop protons emitted from the target but not so thick that any signal electrons that pass through it lose too much energy.

With these considerations in mind, the current design parameters for the CyDet are given in Table. 2.2.

CDC inner radius	55 cm
CDC outer radius	84 cm
CDC length	150 cm
CDC drift gas	He:iso-C_4H_{10} (90:10)
Trigger counter material	Plastic Scinitillator
Trigger counter length	300 mm
Trigger counter thickness	35 mm
Inner wall thickness	0.5 mm
Magnetic field	1 T

Table 2.2: The parameters of the CyDet for COMET Phase-I [29].

2.2.7 Electron Spectrometer

For Phase-II, there will be a final C-section that will act as an electron spectrometer to momentum-select the signal electrons. This will also be a 180° curved solenoid like the muon transport section and gives a further reduction in the number of background events that reach the final detector region.

2.2.8 Straw Tube Tracker and Electromagnetic Calorimeter

The straw tube tracker and electromagnetic calorimeter detector (StrECAL) will be used in Phase-II to measure the momentum and energy of the electrons that make it around the electron spectrometer. For Phase-I, a prototype will be used for background studies.

The full Phase-II straw tube tracker will consist of five stations with four layers of straws in each station to measure the momentum of the electrons and the electromag-

netic calorimeter will be used to measure the energy of the electrons as a redundancy measurement but will also be used as the trigger for the DAQ.

The requirements of the calorimeter are that it needs to have a resolution of $< 5\%$ at 105 MeV/c, a low trigger rate, a spatial resolution of less than 1.5 cm and a quick response of less than 100 ns. The resulting design is an array of approximately 2000 LYSO crystals of dimension $20 \times 20 \times 120$ mm^3 [29].

Chapter 3

Hadron Production Simulations

"Location of shooting craps etc: no moral outrage (5, 5)"
— Boatman, *Guardian #25404*

3.1 Motivation

In order for COMET to optimise the beamline and detector design and make a reliable estimate of its sensitivity, knowledge of the rate of pion and muon production is important. Unfortunately, this is not a well-known value for two reasons. Firstly, COMET will be using a novel pion capture system (see Sec. 2.2.3) and secondly, the pion capture system is designed to collect pions emitted in the backwards region and this is a region of phase space that few experiments have explored.

Although a prototype of the pion capture system has been tested at MUSIC in Osaka [42] and shown that a muon rate of 3×10^8 s^{-1} should be achievable, this was with a very different proton beam to the one COMET will use. The proton beam used in the MUSIC test had an energy of 392 MeV and a current of 1 μA, which corresponds to a proton beam power of 392 W. These are an order of magnitude lower than the COMET Phase-I proton beam power of 3.2 kW and beam energy of 8 GeV. The rate of particle production should scale linearly with the beam power however, the hadron production cross-sections will not. This will affect both the

production of the pions and muons, but also the production of background particles such as antiprotons.

One experiment that did search in this backward region is the HARP experiment [44–46], which ran at CERN between 2000 and 2002 with the aim of measuring the rate of hadron production in different angular regions using a wide-angle spectrometer covering the region from 20° to 160° for different energy protons striking a variety of target materials. Unfortunately, due to internal disagreements, the HARP collaboration split into two groups to analyse the data (HARP and HARP-CDP) which has led to inconsistencies between their results. An example plot from the HARP analysis team is shown in Fig. 3.1 where the HARP data is compared to different hadron production models for an 8 GeV proton beam striking a tantalum ($Z = 73$) target [47] and shows that none of the models agreed at the time.

For COMET to quantitatively assess the uncertainty in the muon production rate, simulations of the pion production section were performed and these studies are discussed in the rest of this chapter.

3.2 Software

3.2.1 Overview

In order to simulate the pion capture section and obtain a quantitative estimate of the pion production uncertainty, two programs were developed using two different Monte Carlo toolkits. The first program, `comet_g4`, uses the GEANT4 toolkit [48, 49] which is widely used throughout the high energy physics community for simulating experiments. The second program uses the `MARS` toolkit [50–53] which is a Monte Carlo generator developed at Fermilab which specialises in low energy nuclear interactions such as the ones in the COMET proton-target interaction.

There are four important aspects of the simulation that need to be implemented as accurately as possible in order to get a reliable result: the geometry of the pion capture system (including the pion production target), the proton beam, the magnetic field and the interaction between the proton and the production target.

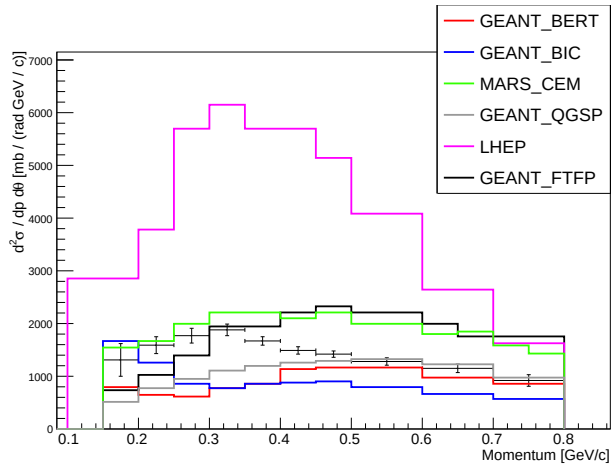

(a) $350 - 550$ mrad $(20 - 32°)$

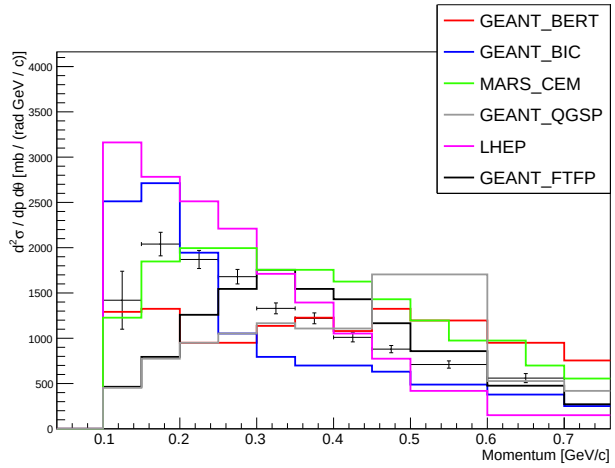

(b) $750 - 950$ mrad $(43 - 54°)$

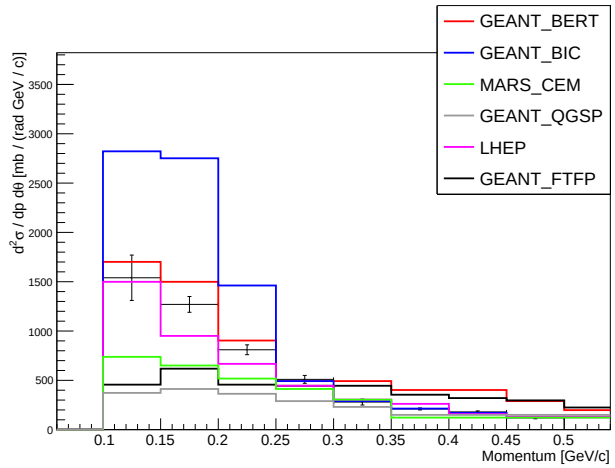

(c) $1750 - 1950$ mrad $(100 - 112°)$

Figure 3.1: Plots of the pion production differential cross-section ($d^2\sigma/dpd\theta$) in the angular bins 350−550 mrad, 750−950 mrad and 1750−1950 mrad comparing the HARP data (points) with different hadron production models (lines) for an 8 GeV proton beam striking a tantalum target ($Z = 73$) (reproduced from [47]). The data in (c) is in the backward region.

3.2.2 Geometry

A baseline version of the geometry of the pion capture section was implemented in both `comet_g4` and `MARS`. This included the solenoids and the shielding as they were designed at the time. Visualisations of the geometry in `comet_g4` and `MARS` are shown in Fig. 3.2 and Fig. 3.3 respectively.

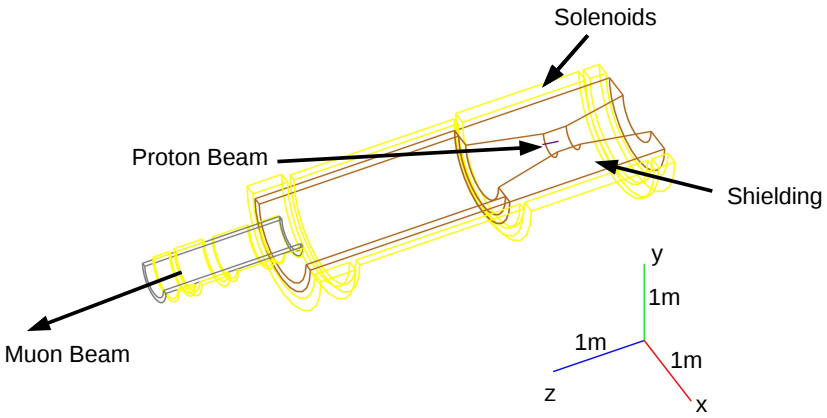

Figure 3.2: A visualisation of the pion capture section in `comet_g4`.

The COMET geometry is defined with respect to a coordinate system where the $+z$-axis is defined as the direction of the muon beam at the beginning of the experiment, the $+x$-axis is defined as the direction parallel to the Phase-I CyDet towards the Phase-I stopping target and the y-axis is defined as perpendicular to the ground.

The proton target geometry was also implemented. However, since these simulations were done before the decision was made to have a graphite target for Phase-I, a tungsten target ($Z = 74$) with a different design than that specified in Sec. 2.2.2 was implemented. A comparison of tungsten and graphite production targets is covered

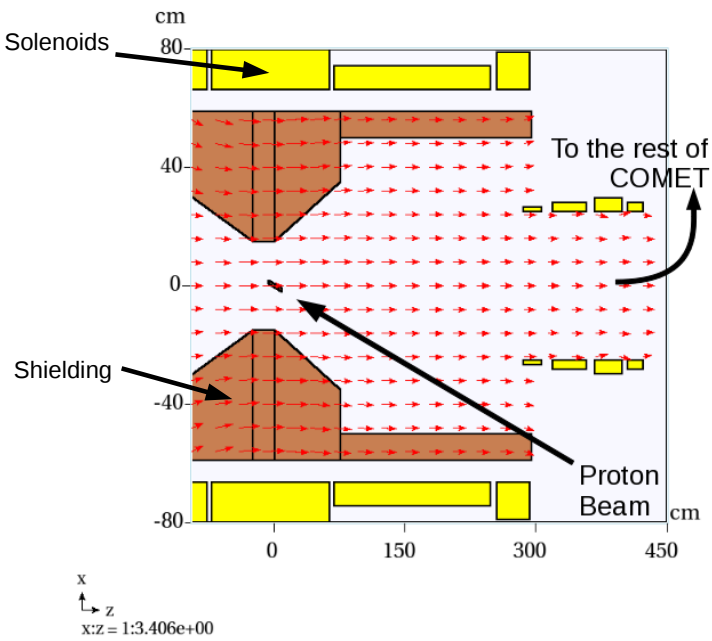

Figure 3.3: A visualisation of the pion capture section in MARS. Also shown are the direction that the proton beam enters and the location of the muon transport section. Note, that the axes have different scales.

in Sec. 3.6 but the details of the design used in the simulations of the tungsten target are given in Table 3.1.

Material	Tungsten
Radius	6 mm
Length	160 mm
Rotation around y-axis	10°

Table 3.1: The parameters of the pion production target for the simulations in this chapter.

3.2.3 Proton Beam

The input proton beam can be easily implemented in both programs by setting values to a series of input parameters. Since no detailed simulation of the upstream part of the proton beamline had been done at the time of these simulations, the

values of these parameters were considered preliminary. For both `comet_g4` and `MARS`, the simulated proton beam had a kinetic energy of 8 GeV, a Gaussian spread of 2 mm $\times$ 2 mm in x and y and was initiated 2 cm in z from the pion production target. The effect of the beam size is covered in Sec. 3.5 and the z position is deemed unimportant since, during the actual experiment, the accelerator team will be able to focus the whole beam onto the target and so the effect of the magnetic field on the protons is ignored here.

3.2.4 Magnetic Field

COMET will be using a special magnetic field configuration in order to capture pions emitted from the pion production target and so it is important that this is represented accurately in the simulations. Both `MARS` and `comet_g4` have the functionality to use an externally defined magnetic field and so both use the exact same fieldmap data file which was supplied to the COMET collaboration by Toshiba, who calculated it based on the given design of the solenoids. A plot of the field strength along the pion capture section is shown in Fig. 3.4.

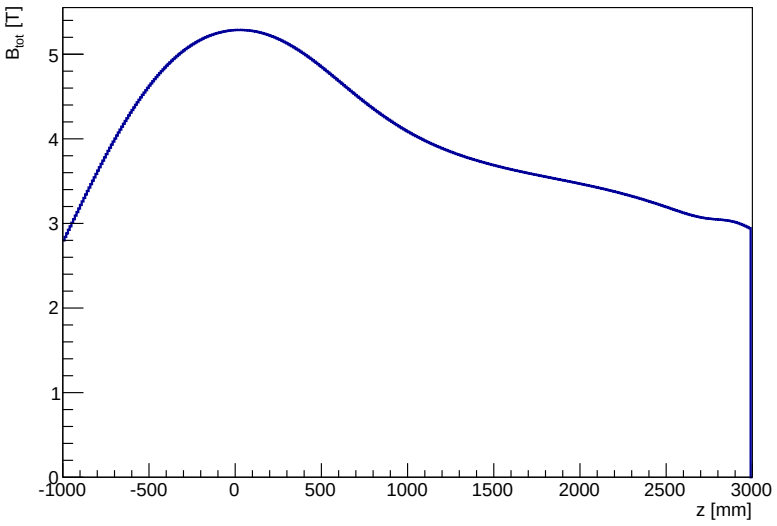

Figure 3.4: A plot of the magnetic field strength in the pion capture system along ($x = 0$, $y = 0$). The centre of the target is located at $z = 0$ and the resulting pions and muons are directed along the $+z$ axis.

3.2.5 Hadron Production Models

If a proton interacts with a nucleus in the target then the proton-target interaction can be modelled in different ways. While the hadron production models are different in detail, they all consist of the same three stages:

Intranuclear Cascade (INC): the primary particle interacts with a nucleon in the nucleus. This primary particle is then rescattered and interacts with other nucleons, producing secondary nucleons, until it has escaped (or is captured by) the nucleus.

Coalescence: the emitted secondaries outside of the target are grouped together to form higher mass states (for example, deuterium, tritium, ^{3}He etc.). This grouping is based on the nucleons being emitted in the same direction and having a small difference between their momenta.

Relaxation/Break-up: the nucleus is left in an excited state after the above stages have occured and a relaxation model simulates the nucleus falling back to the ground state or, for light nuclei, it may break up completely and is simulated using a break-up model.

The differences between hadron production models arise because of the different assumptions used at each stage. For example, how the nuclear density is modelled or when to use the break-up model. Also, differences could arise from the experimental data that the models are tuned to and some may have taken into account the HARP data while others have not. Both `MARS` and `comet_g4` contain different hadron production models and in the following subsections a brief description of these models, their assumptions and regions of validity (as outlined in [54] and [55]) are given.

MARS: Cascade Exciton Model

The intermediate-energy event generator that `MARS` uses is the Cascade Exciton Model (CEM) [56]. It uses an inclusive calculation where each particle is not simulated individually but is given a weighting in order to improve the speed of the calculation.

The intranuclear cascade is based on the standard time-independent Dubna cascade model [57] and the density of the target nucleus is modelled as seven concentric spheres of constant density.

The break-up model is used if any resulting fragment has $A < 13$, otherwise it uses a relaxation model.

One important consideration is that the CEM does not take into account the so-called "trawling" effect, where target nucleons are depleted during the cascade. This means that the CEM is only valid in the region between 1 and 5 GeV. Since COMET will be using an 8 GeV proton beam, this model may not be an accurate representation of the COMET setup but it was still used in the simulations in this chapter.

MARS: Los Alamos Quark-Gluon String Model

Another event generator that `MARS` uses is the Los Alamos Quark-Gluon String Model (LAQGSM) [58]. It is an exclusive calculation where each particle is simulated individually and differs from the CEM model in two important aspects. Firstly, it is a time dependent model and secondly, the density of the nucleus is described by a continuous distribution.

The cross-sections used in the LAQGSM model are from experimental data at low energies and from calculations of the quark-gluon string model at higher energies. These calculations are valid up to about 1 TeV per nucleon, which is well above the energy that COMET will operate at.

One final thing to note about `MARS` is that, although it only has two models, it actually has three different modes: CEM only, LAQGSM only or a mixture of the two where the LAQGSM model is used for all ions when $E > 1 + \frac{65}{A}$, $A < 3$ and for all $\overline{p}$, $K^{\pm}$, d, t, ^{3}He, ^{4}He, $\overline{n}$, hyperons and heavy ions.

GEANT4: LHEP

The LHEP model [55] in GEANT4 is a parameterised model of hadronic interactions composed of two parts: a low energy part (1 GeV to 25 GeV) and a high energy part (25 GeV to 10 TeV). In this model, only the initial interaction is fully simulated and

the results of the remaining interactions are determined by functions that were fitted to experimental data.

GEANT4: QGSP

In GEANT4, there is also a quark-gluon string model [55] which is not the same as the LAQGSM model in MARS. This model appears in a number of GEANT4 hadronic interaction modes but is only used for incoming protons, neutrons, pions and kaons above 10 GeV and another model is used for energies below this. Since COMET will be using an 8 GeV proton beam, it is only the low energy model which is important for simulations and so there is no commonality between any of these modes.

It should be noted that for the QGSP mode in GEANT4, the LHEP model described above is used in the low energy region.

GEANT4: QGSP_BERT

The QGSP_BERT mode [55] in GEANT4 is the same as the QGSP mode except that the Bertini cascade model [59] is used for particles with an energy less than 10 GeV.

In the Bertini cascade model, the target nucleus is modelled by up to 6 concentric spheres of constant density with the exact number of spheres depending on the size of the nucleus.

The break-up model is used in the extreme cases where $A < 12$, $3(A - Z) < Z < 6$ or $E_{\text{excitation}} > 3E_{\text{binding}}$.

GEANT4: QGSP_BIC

The QGSP_BIC mode [55] is the same as the QGSP mode above 10 GeV but the Binary cascade model [60] is used for incoming particles with lower energies.

The Binary cascade assumes all interactions are between a primary particle and a single nucleon in the nucleus with collisions being selected with reference to experimental cross section data. The Binary cascade is also different to the Bertini cascade in that its model of the nuclear density for light nuclei ($A < 17$) is given

by a harmonic oscillator shell model and for heavy nuclei is given by a continuous distribution.

GEANT4: FTFP_BERT

Finally, the FTFP_BERT model [55] uses the same Bertini cascade as in QGSP_BERT, but only for protons with energies below 5 GeV. Above this energy (in the region that is important for COMET) the FRITIOF string model is used.

The FRITIOF model has an upper limit of 1 TeV per nucleon like the LAQGSM model because it does not include multi-jet production. Again, this is not a problem for these simulations since COMET will run at a much lower proton beam energy.

Another important aspect of the FRITIOF model is that it does not perform intranuclear cascades of any secondaries that are produced from the primary proton beam interacting with the nucleons.

3.3 Differences between the Forward and Backward Regions

3.3.1 Setup

The first study done was to investigate the momentum distribution of pions emitted from the pion production target in the forward and backward directions and simulations using the hadron production models in both `MARS` and `comet_g4` were performed.

The simulation was setup as described in Sec. 3.2 with the addition of three software monitors placed around the pion production target. Two circular monitors were placed at each end of the production target and one cylindrical monitor was placed around it. All particles were recorded as they passed through any of the monitors. A diagram of the setup is shown in Fig. 3.5.

For each `comet_g4` model, 10^6 protons were fired at the pion production target and for each `MARS` mode, 10^5 protons were generated. Note that in this study, the forward

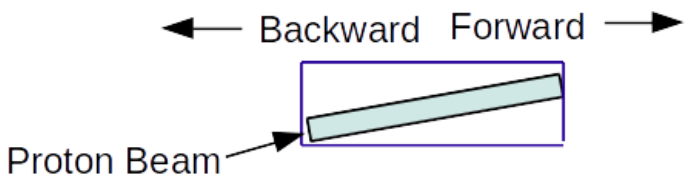

Figure 3.5: A diagram of the simulation setup for the forward-backward differences study. The pion production target is in light blue and the software monitors are represented by the dark blue box.

direction is defined with respect to the incoming proton beam rather than the muon beam.

3.3.2 Results

The pions that passed through the monitors are plotted in Fig. 3.6, where those with $p_z < 0$ are defined as going in the forward direction and those with $p_z > 0$ are defined as going in the backward direction.

As can be seen from these plots, there are large differences in both the shape and size of the momentum distributions between the different hadron production models in the forward region. However, in the backward region, the models have a better agreement on the shape (although there is still some momentum dependence) than on the overall normalisation.

Because of these differences, it is important to know how much of the final COMET muon beam is composed of muons coming from decays of pions emitted in the forward direction and how much arises from pions emitted in the backward direction. If the pion capture system does chiefly collect backwards travelling pions (as it is designed to do) then the uncertainty on the muon yield will only have a small momentum dependence.

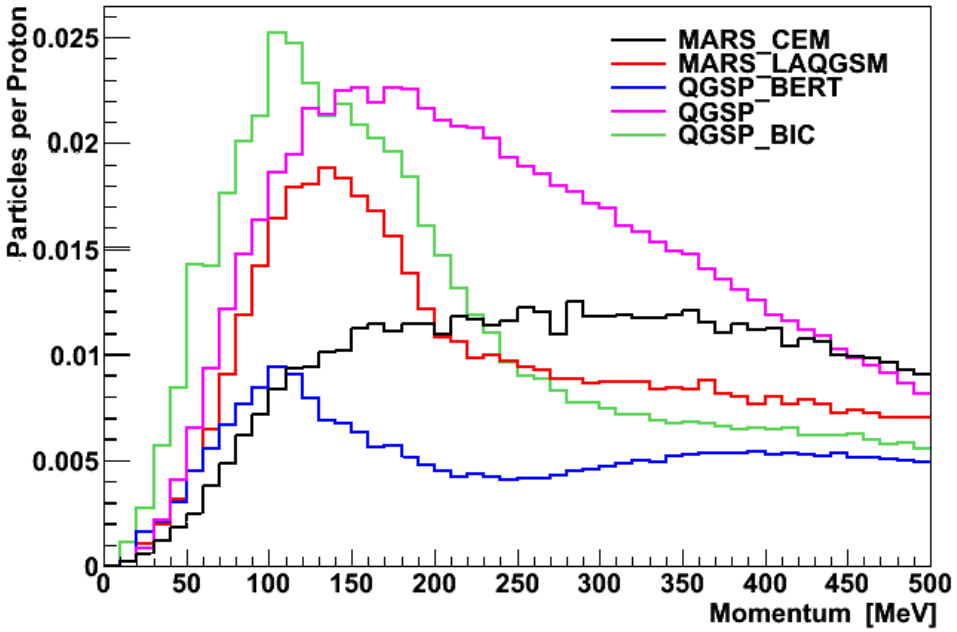

(a) Forward region.

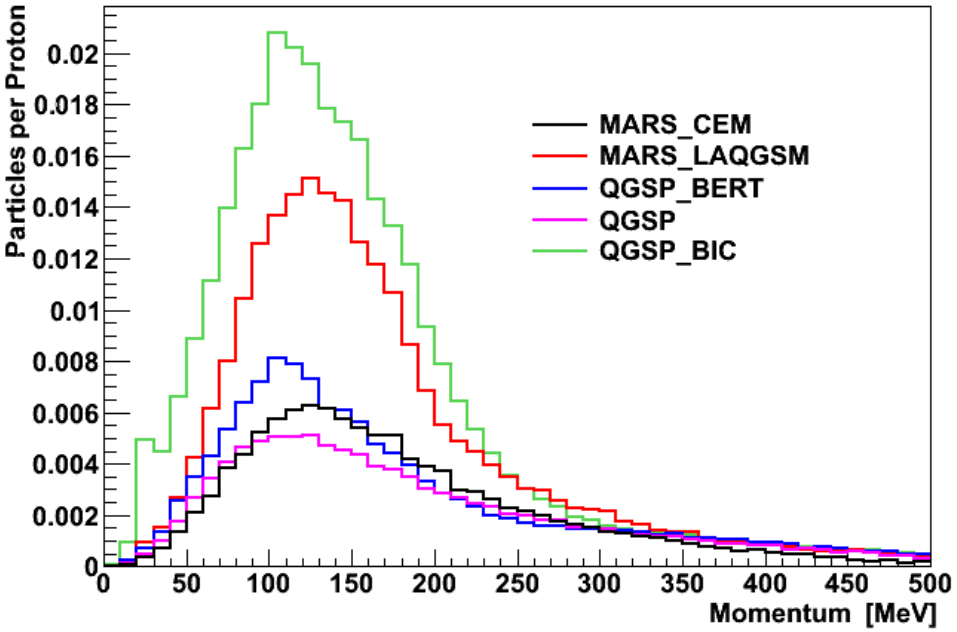

(b) Backward region.

Figure 3.6: Comparison of the momentum distributions of π^- (normalised to the number of input protons) in the (a) forward and (b) backward regions for different hadron production models (note that FTFP_BERT was not used for this study).

3.4 Effect of Magnetic Field

3.4.1 Setup

The second study done was to investigate the effect of the magnetic field and to check that the pion and muon yields do increase as expected.

The setup of the experiment was the same as in the previous study but with the addition of a software monitor placed 3 m downstream of the pion production target to record the particles that managed to exit the pion capture system and enter the muon transport section. Simulations were performed of 10^6 protons using the QGSP_BERT model in `comet_g4` both with and without the magnetic field. It is assumed that there will be no difference when using `MARS`.

3.4.2 Results

The results of this study are shown in Fig. 3.7, where the momentum distribution of all pions emitted in the backward direction are shown in black. Of these, the pions that reached the 3 m monitor are shown in red and the pions that were initially emitted in the forward direction and reached the 3 m monitor are shown in blue.

It is evident from these plots that the magnetic field does significantly increases the number of pions that enter the muon transport section since, in the no magnetic field simulation, only a few pions managed to exit the pion capture system at all. In addition, it can be seen that, with the magnetic field, the fraction of forward pions that constitute the muon beam is very small when compared with the backward pions. Therefore, the large differences between different hadron production models of the shape of the momentum distribution in the forward direction will have a small effect and is neglected.

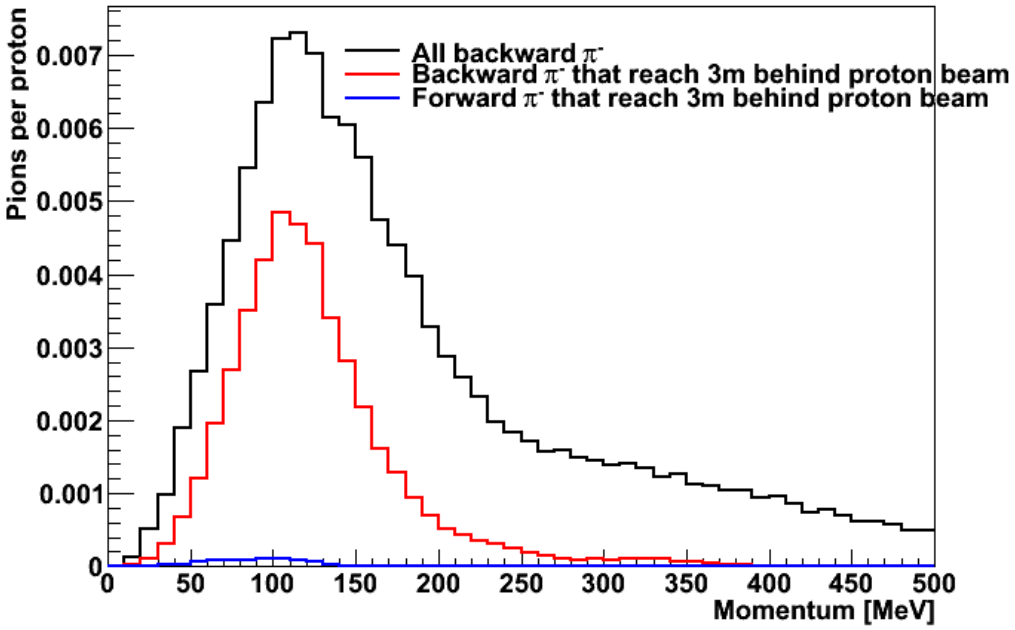

(a) with magnetic field

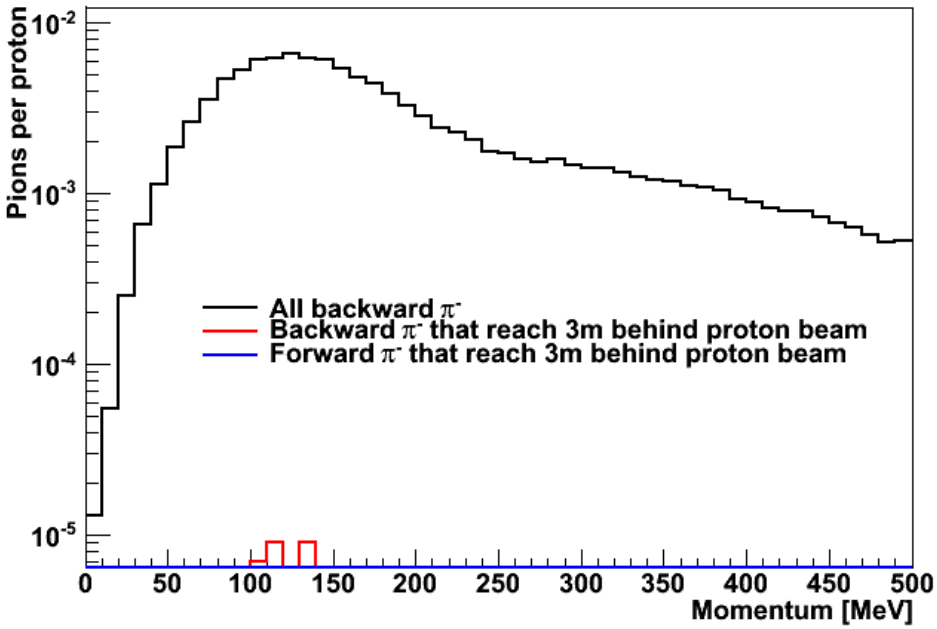

(b) without magnetic field

Figure 3.7: Plots of the π^- momentum distribution (a) with and (b) without the magnetic field. All backward pions (black), backward pions that reach the 3 m monitor (red) and forward pions that reach the 3 m monitor (blue) are shown.

3.5 Pion and Muon Yield

3.5.1 Setup

The next study performed was to evaluate the variance of the pion and muon yield between the different hadron production models.

The simulation setup is similar to that in the previous study except the monitors around the pion production target were removed and only the monitor placed at 3 m downstream is used. For the three GEANT4 models 10^6 protons were simulated and for the three MARS modes 10^5 protons were simulated.

3.5.2 Results

The muon and pion momentum distributions for the MARS models and the `comet_g4` models are shown in Fig. 3.8 and Fig. 3.9 respectively.

These plots again show that the only significant difference between hadron production models is in the normalisation of the pion and muon momentum spectra and there is little difference in the shape. The pion and muon yields per proton for the different models are listed in Table 3.2 and plotted in Fig. 3.10. From these values the difference between the highest (MARS_LAQGSM) and lowest (FTFP_BERT) values is found to be a factor of 3.27 ± 0.03.

Hadron Production Model	Monte Carlo Generator	$(N_{\mu^-} + N_{\pi^-})/N_p$
CEM only	MARS	0.061 ± 0.001
CEM/LAQGSM	MARS	0.138 ± 0.001
LAQGSM only	MARS	0.144 ± 0.001
QGSP_BERT	GEANT4	0.0511 ± 0.0002
QGSP_BIC	GEANT4	0.1278 ± 0.0005
FTFP_BERT	GEANT4	0.0440 ± 0.0002

Table 3.2: The number of pions and muons per proton reaching the 3 m monitor for each of the hadron production models investigated in this section.

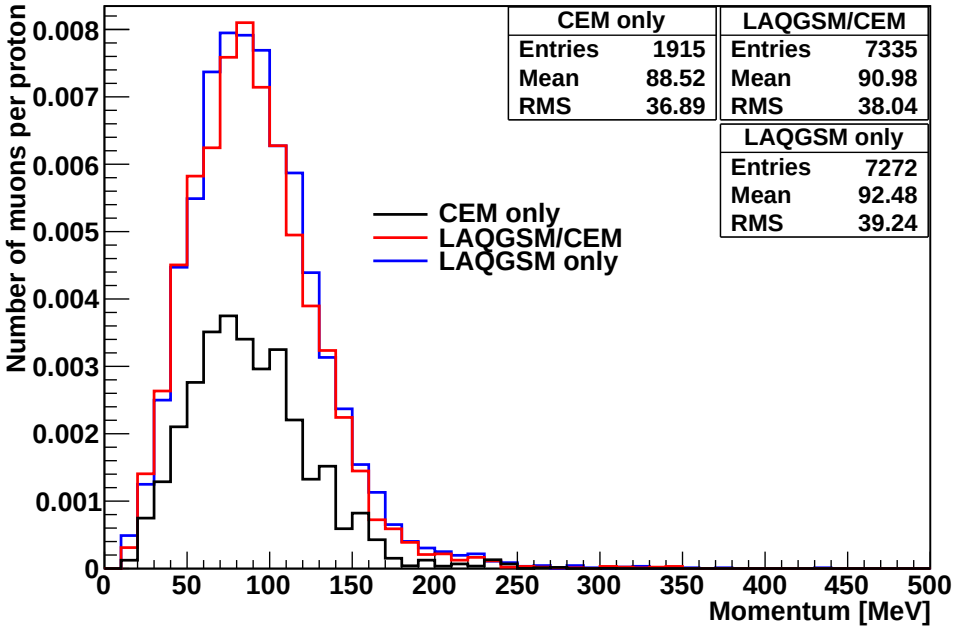

(a) μ^- momentum distribution.

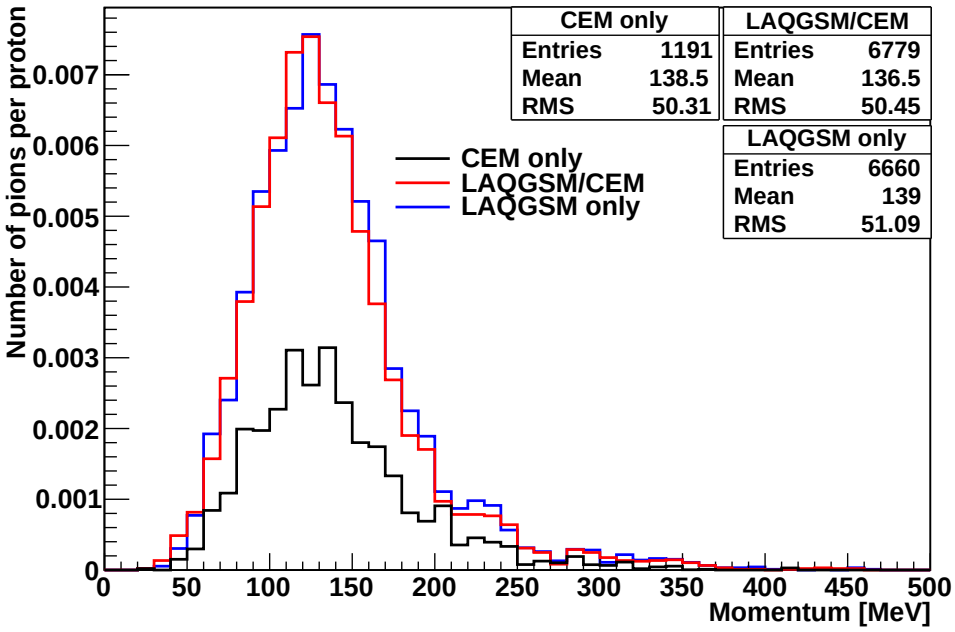

(b) π^- momentum distribution.

Figure 3.8: Comparison of the momentum distribution of (a) μ^- and (b) π^-, normalised to the number of input protons, at 3 m for the three different MARS hadron production modes.

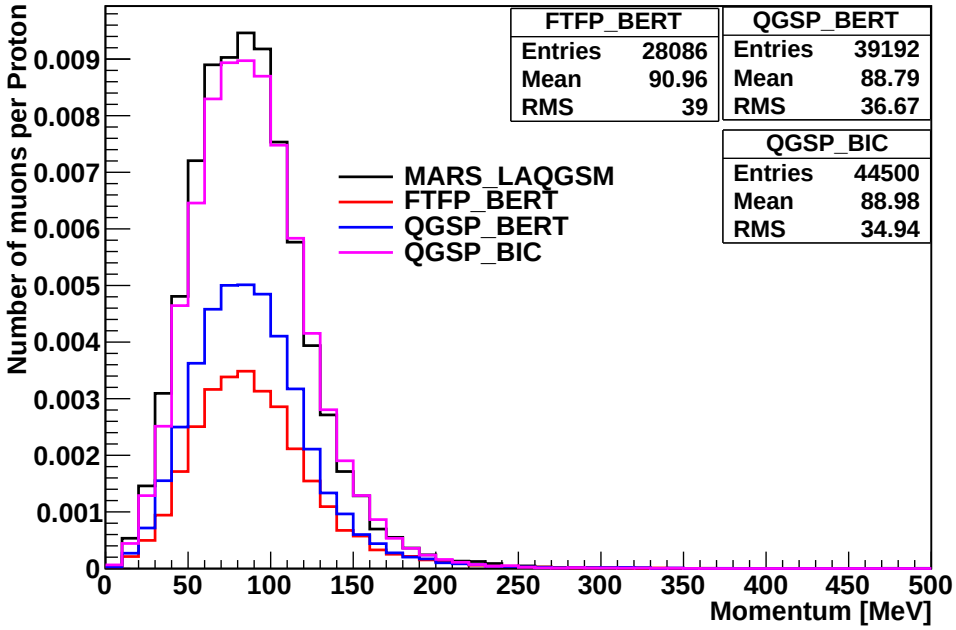

(a) μ^- momentum distribution.

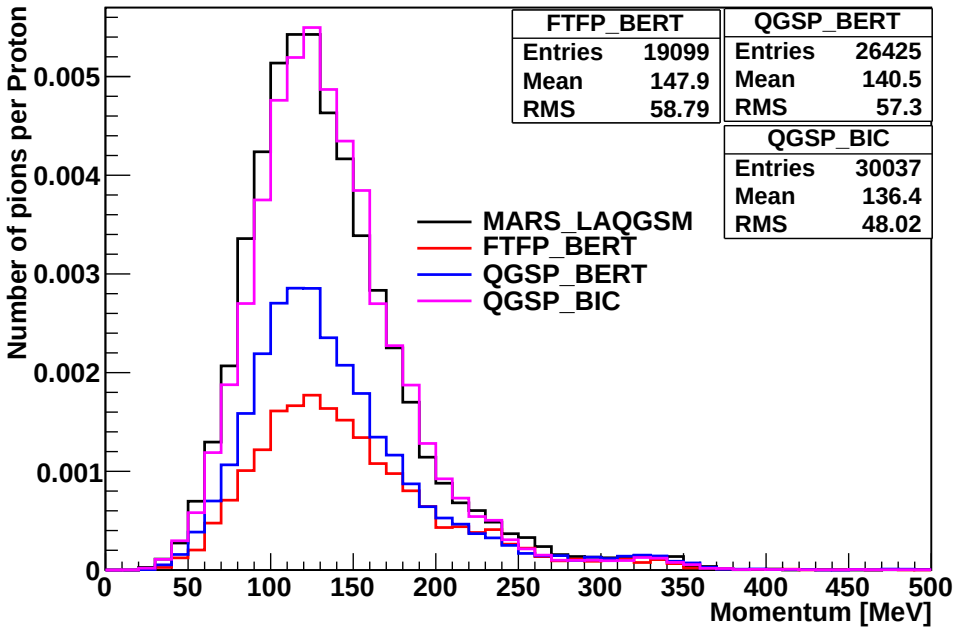

(b) π^- momentum distribution.

Figure 3.9: Comparison of the momentum distribution of (a) μ^- and (b) π^-, normalised to the number of input protons, at 3 m with different GEANT4 modes (MARS_LAQGSM added for comparison).

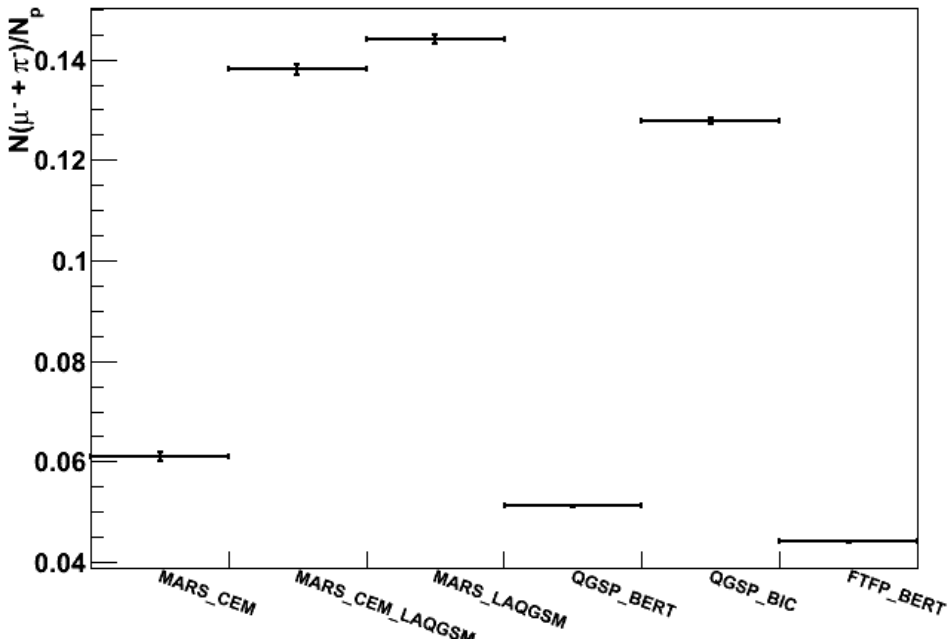

Figure 3.10: A plot of the number of pions and muons per proton reaching the 3 m monitor for each hadron production model investigated in this section.

In Fig. 3.10 two distinct groups can be seen: one at ~ 0.05 pions and muons per proton and another at ~ 0.14 pions and muons per proton. There is no way to ascertain which (if either) of these is correct. To characterise the scale of the uncertainty, it is worth noting that the mean of the values is ~ 0.09 and the spread is ~ 0.04 and so the pion and muon yield should, at 90% CL, be in the region 0.01 to 0.17 pions and muons per proton. Since this is quite a large uncertainty, COMET Phase-I will take the opportunity to measure the pion and muon yield and establish which model is most accurate for this situation. It is worth noting that for all COMET background estimates, the conservative QGSP_BERT model is used.

As a brief aside, the effect of changing the simulated beam size was investigated using the QGSP_BERT model. The pion and muon yields are shown in Table 3.3. As can be seen, the yields are very similar until the beam size is greater than the diameter of the pion prodution target, at which point, the protons start to miss the target completely.

Beam Size [mm]	Pion and Muon Yield at 3 m
2	0.0511 ± 0.0002
4	0.0517 ± 0.0003
6	0.0528 ± 0.0003
8	0.0313 ± 0.0002
10	0.0200 ± 0.0001

Table 3.3: A table of the pion and muons yields for different size beams.

3.6 Target Material and Length

3.6.1 Setup

As mentioned in Sec. 3.2, the pion production target used in these simulations was made of tungsten ($Z = 74$). However, for COMET Phase-I, the decision was made to move to a graphite production target ($Z = 6$) in order to remove the need for a special cooling system. It is known that the muon yield will decrease when moving to the low-Z target since there are fewer nucleons to interact with the incoming proton.

Simulations of 10^6 protons striking graphite targets of lengths 15 cm, 30 cm, 60 cm and 80 cm were performed using `comet_g4` and the QGSP_BERT model keeping all other conditions the same.

3.6.2 Results

Plots of the momentum distributions of pions and muons for each length of graphite production target are shown in Fig. 3.11 with the 16 cm tungsten target also shown for comparison. The pion and muon yields at 3 m for each length are given in Table 3.4 and shows that graphite targets do result in a lower pion and muon yield as expected.

COMET Phase-I was initially planned to run for 90 days with a tungsten production target. However, Fig. 3.12 shows that if a 60 cm graphite production is used, then COMET will not achieve its target sensitivity because of this reduction in the pion

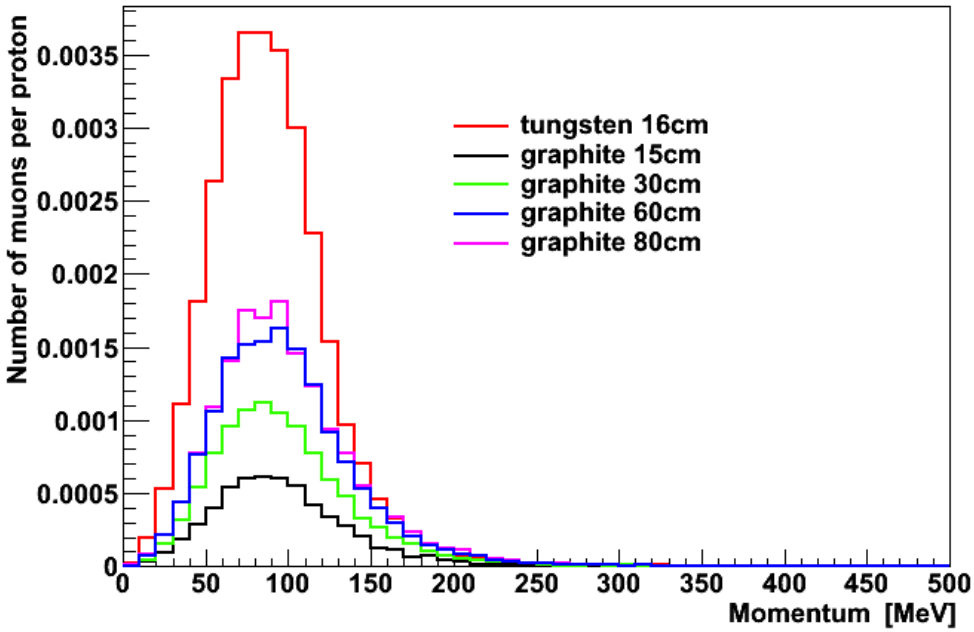

(a) μ^- momentum distribution.

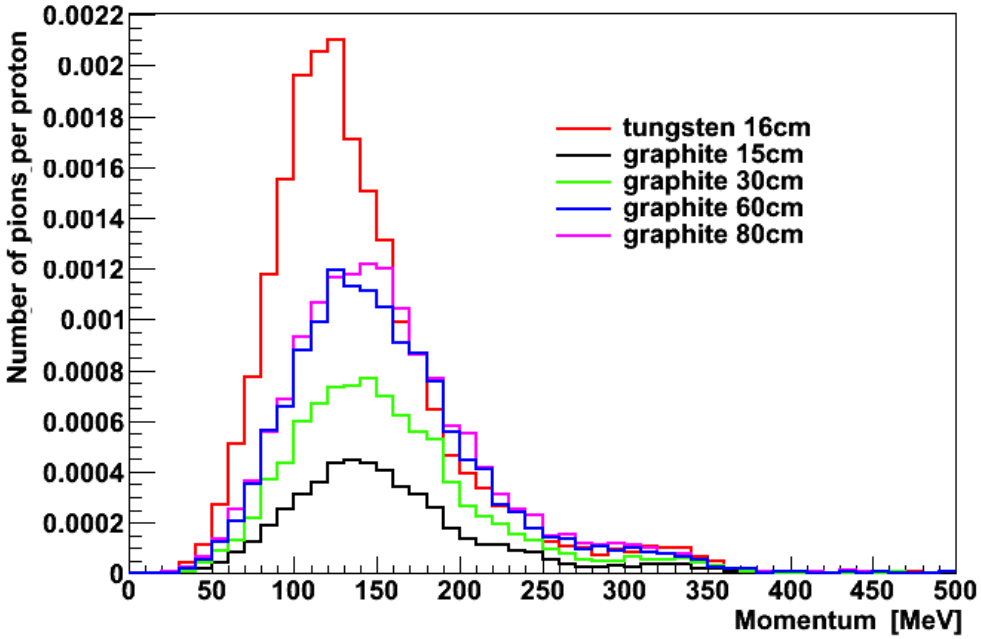

(b) π^- momentum distribution.

Figure 3.11: Comparison of the momentum distribution of (a) μ^- and (b) π^-, normalised to the number of input protons, at the 3 m monitor for a tungsten target of length 16 cm (red) and graphite targets of lengths 15 cm (black), 30 cm (green), 60 cm (blue) and 80 cm (magenta) pion production target.

Material	Length	$(N_{\mu^-} + N_{\pi^-})/N_p$
Graphite	15 cm	0.0109 ± 0.0001
Graphite	30 cm	0.0195 ± 0.0002
Graphite	60 cm	0.0292 ± 0.0002
Graphite	80 cm	0.0311 ± 0.0002
Tungsten	16 cm	0.0511 ± 0.0002

Table 3.4: The number of pions and muons per proton reaching the 3 m monitor for each of the different pion production targets investigated in this section.

and muon yield by a factor of 1.6 ± 0.1. Therefore, it is suggested that COMET Phase-I should run for 110 days.

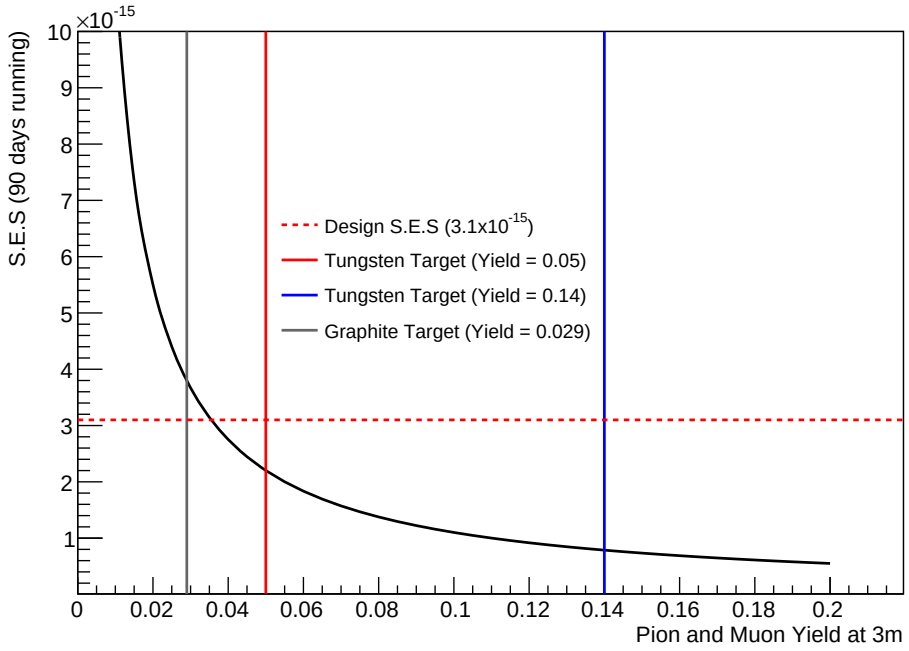

Figure 3.12: A plot of the S.E.S after 90 days of running as a function of the pion and muon yield at 3 m. Also shown are the design sensitivity (dashed, red) and yields corresponding to a 60 cm graphite target (grey, 0.029 pions and muons per proton), and a 16 cm tungsten target (both the high yield (blue, 0.14 pions and muons per proton) and the low yield (red, 0.05 pions and muons per proton)).

3.7 Conclusions

Simulations have shown that different hadron production models predict different shapes of the pion momentum spectrum for pions emitted in the forward direction while there is only a difference in the normalisation for pions emitted in the backward direction.

In addition, these simulations have shown that the magnetic field underpinning COMET's novel pion capture system chiefly collects pions emitted in the backward direction and very few in the forward direction. This means that the uncertainty in the pion and muon beam leaving the pion capture section is limited to an uncertainty in the total yield of pions and muons rather than in their momenta.

The value for the pion and muon yield is, at 90% CL, in the region 0.01 to 0.17 pions and muons per proton. With the difference between the highest and lowest value being a factor of 3.27 ± 0.03. COMET Phase-I will measure the muon yield so that a determination of the most accurate hadron production model can be made.

Finally, there was a study of the effect on the pion and muon yield of moving to a graphite pion production target for COMET Phase-I. This preliminary study found that the pion and muon yield will be reduced by a factor of 1.6 ± 0.1 and so COMET Phase-I will run for 110 days instead of the planned 90 days to achieve a S.E.S of 3.1×10^{-15} assuming 0.0292 pions and muons per proton.

Chapter 4

The AlCap Experiment

"Metal I dropped over the Atlantic (9)"
— Orlando, *Guardian #26136*

4.1 Overview

The AlCap experiment [61] is a joint venture between Comet and Mu2e that aims to measure the spectra of particles emitted after a muon has been captured by a nucleus. A brief discussion of this nuclear muon capture process and its impact on the Comet experiment has already been presented in Sec. 1.3.4.

This chapter will first provide some further motivation for the experiment based on the existing data that is present in the literature. Then, it will go on to state the aims of the AlCap experiment before giving a comprehensive summary of the first AlCap run at which I was present. This will include a description of the experimental setup and an overview of the data collected. Finally, the software and analysis framework, which I was heavily involved in, will be described.

An analysis of the AlCap data using these tools will be presented in Ch. 5.

4.1.1 Existing Data

As previously stated, there already exists some data on charged particle emission after nuclear muon capture in the literature. These results come from experiments performed in the 1960s and 1970s [62–65] at different muon facilities in the world. Unfortunately, these results are not entirely appropriate to Comet for a number of reasons.

Firstly, there is no particle identification in these experiments and so the ratio of protons to deuterons to tritons is unknown. This would be a useful value to know since tritons have a larger penetration depth than protons and so the design of any absorber in the CyDet should take this into account.

Secondly, the current best data for charged particles emitted from aluminium [65] only measured protons at energies higher than 40 MeV, whereas Comet would like to also have information on protons in the whole energy range.

Finally, the data at the lower energies are for particles emitted from muon capture on silicon [63], which is not the material that Comet will be using to stop muons. The results of this experiment are shown in Fig. 4.1 and two regions can be seen around the trough at 1.4 MeV. The low energy region is due to nuclear recoils from neutron emission and the high energy region is due to proton emission and is the section of the spectrum that is important. In this high energy region it was found that there are 0.15 charged particles per muon capture.

To date, Comet and Mu2e use a fit to this measurement [66] for background estimates. This is given in Eq. 4.1, where T is the kinetic energy, $T_{th} = 1.4$ MeV, $T_0 = 3.1$ MeV, $\alpha = 1.328$, $A = 0.15$ and N is a normalisation factor. The resulting function is shown in Fig. 4.2. Moving away from this to aluminium data would obviously give a more accurate estimate of the Comet backgrounds.

$$\frac{A}{N}\left(1 - \frac{T_{th}}{T}\right)^{\alpha} e^{-\frac{T}{T_0}}. \tag{4.1}$$

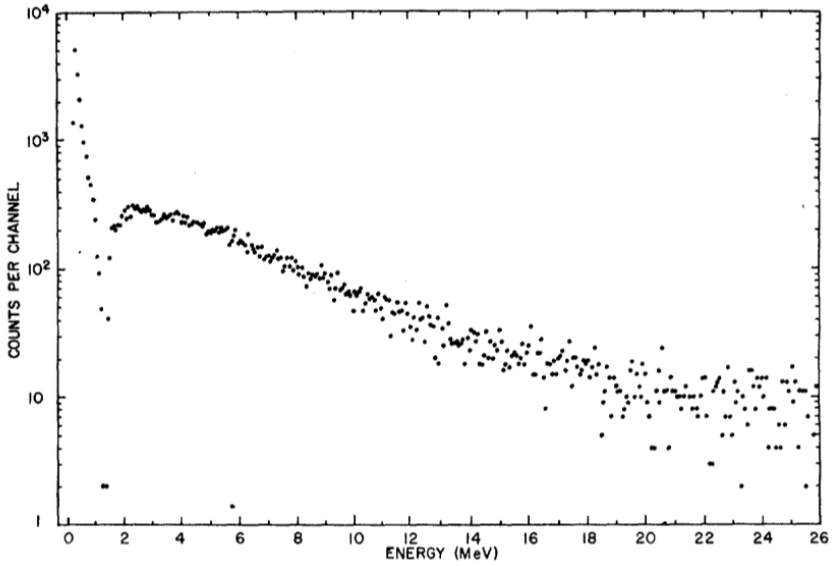

Figure 4.1: A plot of the number of charged particles per channel, emitted during nuclear muon capture on silicon, as a function of energy [63].

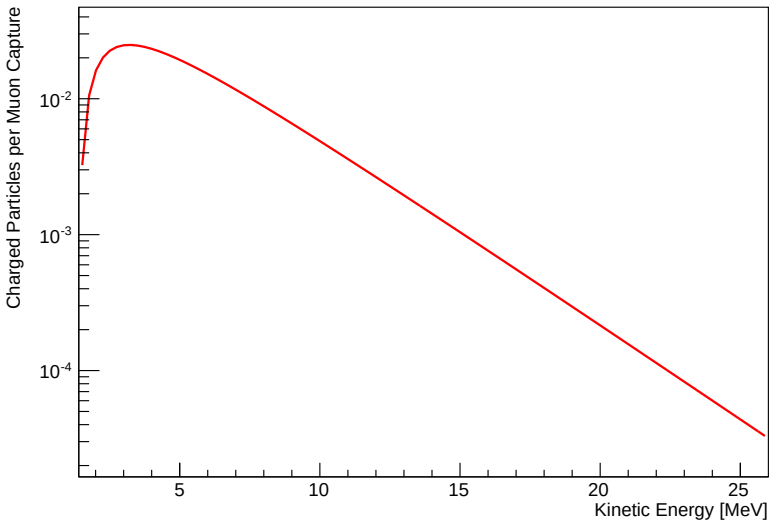

Figure 4.2: A plot of the parameterisation of Fig. 4.1 used by the Comet and Mu2e experiments.

4.1.2 Aims

In order to update the literature and provide some important information to Comet and Mu2e, the AlCap collaboration was set up, consisting of about 10 academics and students from both collaborations, with three main aims relating to each of the possible emission products from nuclear muon capture:

Proton emission: establish the rate and spectrum of proton emission with a precision of 5% down to 2.5 MeV. This is the limit of the experimental setup since protons with a lower kinetic energy will stop in the thin silicon layer (see Sec. 4.2.2).

Gamma and X-ray emission: investigate some new techniques of counting the number of stopped muons for Comet and Mu2e.

Neutron emission: establish the rate and spectrum of neutron emission from 1 MeV up to 10 MeV. This energy range comes from simulations of Mu2e that show that most neutrons reaching the cosmic ray veto are below 10 MeV with the most probable energy being 1 MeV [61].

4.1.3 The First Run

A proposal was accepted by the Paul Scherrer Institute (PSI, Switzerland) in January 2013 and the first AlCap run was carried out in December 2013.

The πE1 secondary beamline [67] was used because it provides a well-tuned low momentum μ^- beam that a few members of the AlCap experiment have experience with from their participation in the MuSun experiment [68]. A drawing of the beamline is shown in Fig. 4.3.

The primary focus of the first run was to measure the proton emission spectrum and to use the emitted X-rays to determine the number of stopped muons. In addition, some preliminary work on the detectors for the neutrons and gamma rays was carried out but this will be the major focus of a second AlCap run later in 2015 and will not be covered further in this thesis.

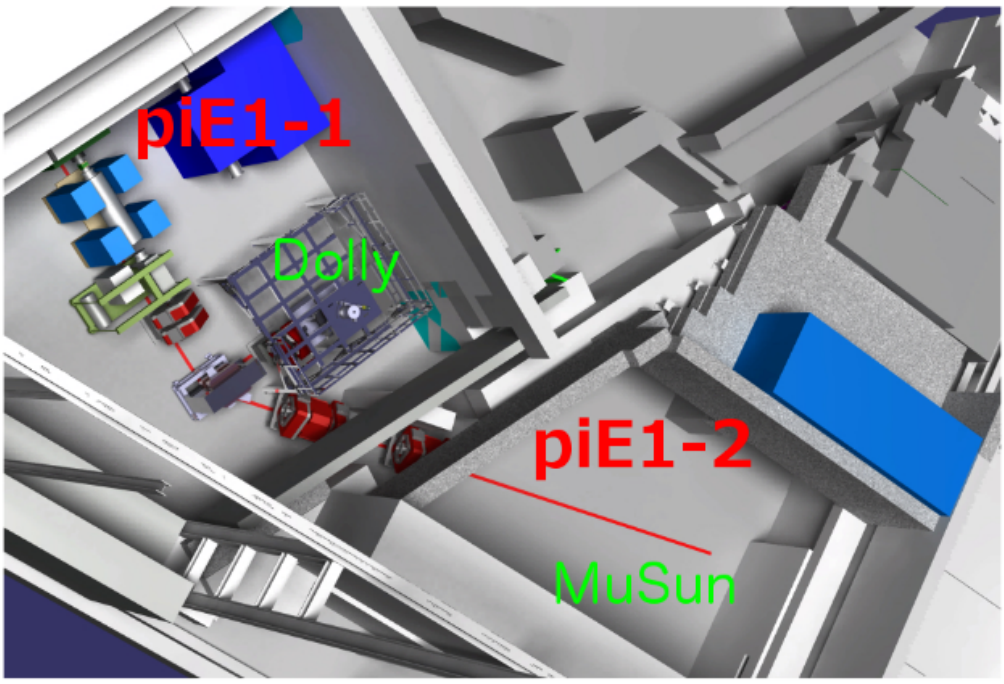

Figure 4.3: A drawing of the πE1 beamline [69].

4.2 Experimental Setup

The AlCap experiment is mostly contained within a vacuum chamber of diameter 32.4 cm and height 38 cm. A photograph of the experiment taken from above the chamber is shown in Fig. 4.4 and a diagram highlighting the important components is shown in Fig. 4.5.

With reference to Fig. 4.5, the experiment is set up so that muons enter the vacuum chamber through the port on the left-hand side and are stopped in a stopping target placed in the centre (blue). Once the muons are stopped, a fraction of them will undergo nuclear muon capture. During this process, particles will be emitted from the target and measured in the various detectors surrounding it. The charged particles that are emitted will be detected in the two detector systems placed at $\pm 90°$ to the muon beam inside the chamber (green and red) and any photons emitted will be measured in the germanium detector outside the chamber (top-left). In addition to the detectors measuring the emitted particles, there is also an entrance counter to measure the incoming muon beam (green line on the far left) and a veto scintillator placed behind the target so that punch-through muons can be vetoed (green line

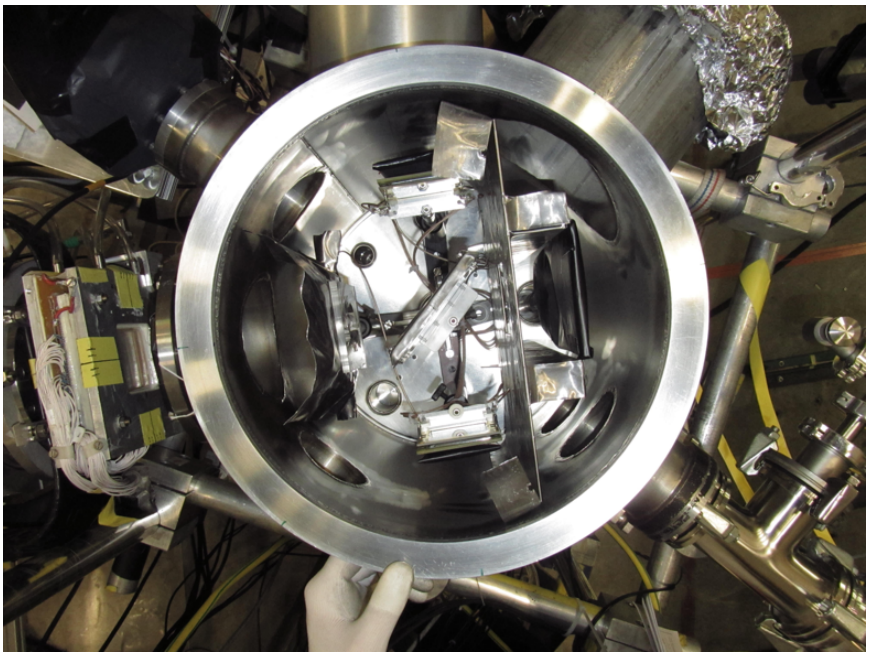

Figure 4.4: A photograph of the AlCap experiment. The diameter of the vacuum chamber is 32.4 cm and the height of the chamber is 38 cm.

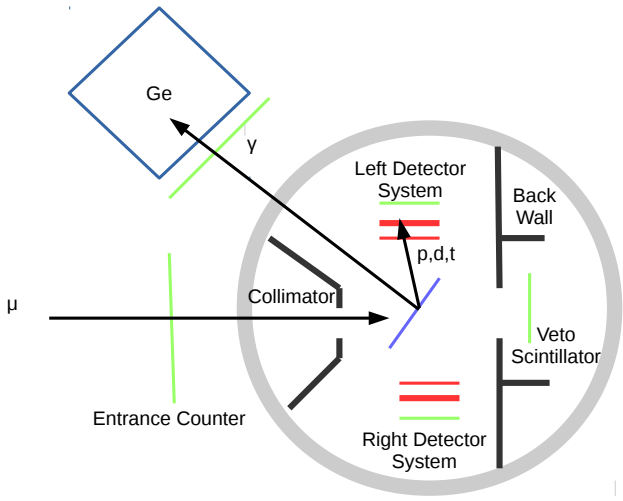

Figure 4.5: A diagram of the AlCap chamber with the target, detectors and shielding highlighted (see text for more details).

on the far right). Finally, in order to ensure that only emission products from the target are analysed, lead shielding is used to obscure parts of the experiment that could compromise this (black). The following subsections describe these parts of the experiment in more detail.

4.2.1 Stopping Target

The stopping target is where the muons are stopped and undergo nuclear muon capture and there are two materials that AlCap collected data on: aluminium, because both Comet and Mu2e will be using this material for their muon stopping targets to search for $\mu - e$ conversion; and silicon, so that a cross-check with the previous data shown in Fig. 4.1 could be made.

For each target material used in the run, two different thicknesses were used. For silicon, the targets were 1500 μm[1] and 62 μm thick and for aluminium the targets were 50 μm and 100 μm thick. Each sample was screwed inside a plastic holder and attached to a standard optical stand. The target was then placed in the centre of the chamber and rotated to be at an angle of 45° to the beam axis. A photograph of the aluminium target in its stand is shown in Fig. 4.6.

4.2.2 Detector Systems

The charged particles emitted from the stopping target are detected by the detector systems placed 12 cm away on either side of the target at ±90° to the beam. Each detector system consists of three layers: a thin (58 μm) silicon detector, a thick (1500 μm) silicon detector and a plastic scintillator. A photograph of the detector systems inside the chamber is shown in Fig. 4.7.

By layering the silicon detectors in this way, particle identification can be performed by plotting the energy deposited in the thin silicon layer (E_1) against the total energy deposited in both the thin and thick silicon layers ($E_1 + E_2$). This is demonstrated in Fig. 4.8, where a plot from the AlCap Monte Carlo simulation (described in Sec. 4.3.3) shows that there are clear bands corresponding to protons, deuterons, tritons and alphas.

[1]Note, one of the thick silicon detectors (see Sec. 4.2.2) was used for this target.

Figure 4.6: A photograph of the aluminium target in its holder with lead shielding covering the plastic holder.

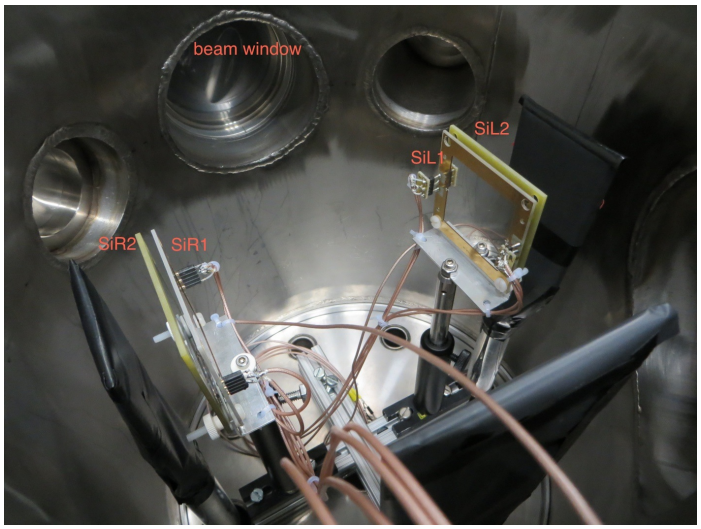

Figure 4.7: A photograph of the detector systems inside the chamber. One can see the thin silicon layers (SiL1 and SiR1), the thick silicon layers (SiL2 and SiR2) and the scintillators (wrapped in black paper).

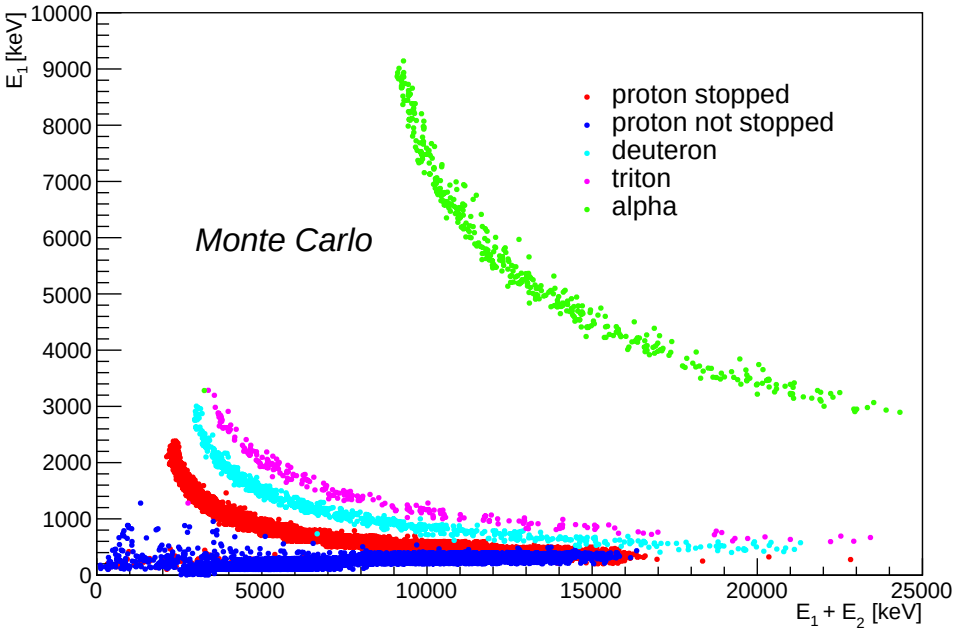

Figure 4.8: A plot of E_1 vs $E_1 + E_2$ of particles emitted from aluminium in a simulation of the AlCap experiment. Bands corresponding to protons, deuterons, tritons and alphas can be seen. Note that this plot does not take into account hits in the veto scintillators, if it did, then the blue band would not appear.

The plastic scintillator layer situated behind the silicon systems can act as a veto for any charged particles that do not completely stop in the thick silicon layer. The fraction of protons that stop in the thick silicon layer as a function of energy is shown in Fig. 4.9 and, as can be seen, the majority of protons with a kinetic energy less than 15 MeV will be stopped.

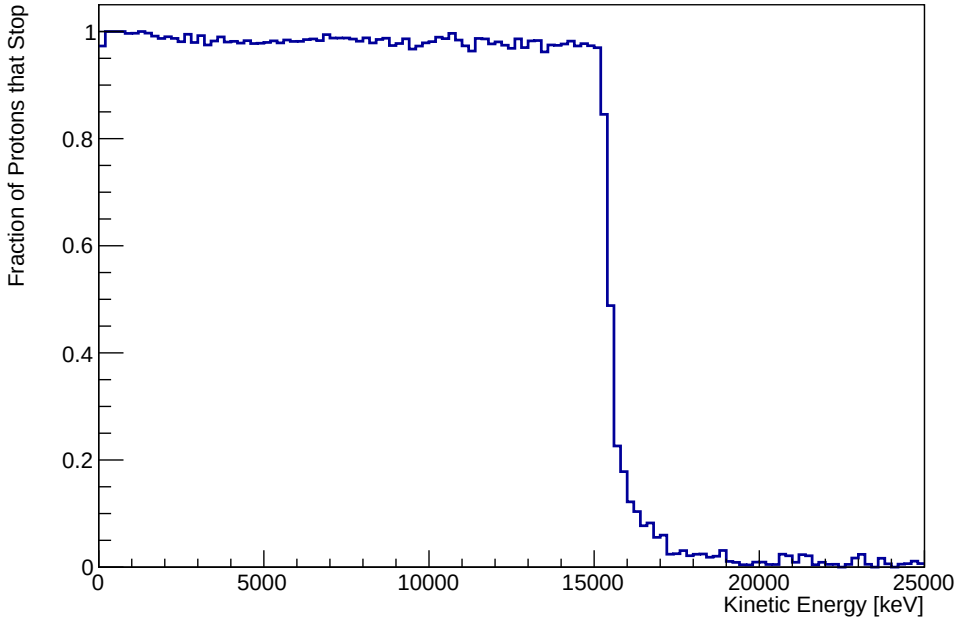

Figure 4.9: A plot of the fraction of protons that stop in the thick silicon layer as a function of energy from Monte Carlo.

All the silicon detectors had an active area of 50 x 50 mm^2 and were manufactured by Micron. The thin silicon detectors were Micron MSQ25 detectors [70] of 58 μm thickness and the thick silicon detectors were Micron MSX25 detectors [71] of 1500 μm thickness. The thin detectors have their active areas split into four quadrants, each with their own output.

4.2.3 Germanium Detector

Photons emitted from the target are measured in a germanium detector placed outside of the chamber next to one of the chamber ports and pointed towards the

target. The germanium detector used was a GMX Series HPGe Coaxial Detector System manufactured by ORTEC [72].

The main use of the germanium detector in the first AlCap run was to detect the muonic X-rays that are emitted when the muon is first captured by the atom and falls to the $1s$ state. By counting these X-rays, the number of stopped muons can be determined and thus used for normalisation. The muonic X-rays are characteristic of the material that the muon has stopped in and the energy level it falls from. The energy and intensity of these muonic X-ray peaks for silicon and aluminium are shown in Table 4.1, where the intensity of each peak is defined relative to the sum of all peaks in the spectrum.

Material	Transition	Intensity [%]	Energy [keV]	Ref.
Al	$2p - 1s$	79.8 ± 0.8	346.828 ± 0.002	Table II [37]
	$3p - 1s$	7.62 ± 0.15	412.87 ± 0.05	Table II [37]
Si	$2p - 1s$	80.3 ± 0.8	400.177 ± 0.005	Table XII [37]
	$3p - 1s$	7.40 ± 0.20	476.80 ± 0.05	Table XII [37]

Table 4.1: The energies and intensities of the muonic X-ray peaks in silicon and aluminium.

In addition to the germanium detector itself, a plastic scintillator was placed between the flange of the vacuum chamber and the germanium detector in order to veto any electrons that reach the germanium detector.

4.2.4 Lead Shielding

Lead shielding is used in various parts of the experiment in order to ensure that only emissions from the stopping target are measured during the analysis.

Lead is an appropriate material since it has a very short muonic atom lifetime of 80 ns, which is much shorter than the muonic atom lifetime of both aluminium (864 ns) and silicon (767 ns) [43]. Therefore, in order to ensure that only particles emitted from the target are analysed, a time cut can be made to remove any particles that arrive early since these are likely to have come from muons stopping in lead.

Lead shielding is placed in three parts of the experiment: just after the muon beam enters the chamber, behind the muon stopping target and around the target itself to cover the plastic holder.

The lead shielding just after the muon beam enters the chamber covers a collimator made of plastic. The hole in this collimator defines the shape of the muon beam that is incident on the target. The walls of the collimator also prevent muons from travelling directly into the silicon detectors and stopping there, since this will cause particles to be emitted directly into the detector systems.

There is also a lead wall placed behind the target, which stops any punch-through muons stopping in the steel chamber itself. A hole is made in the back wall so that the scintillator behind the target can still be used to veto any punch-through muons. A photograph of the back wall is shown in Fig. 4.10.

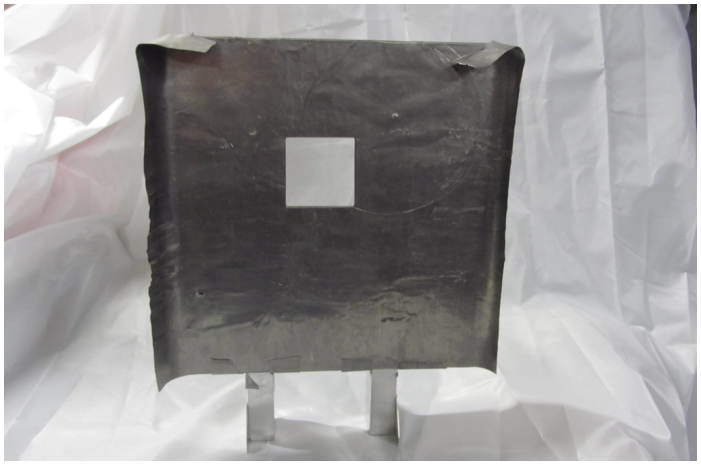

Figure 4.10: A photograph of the back wall. The hole allows the veto scintillator to still be used.

4.2.5 Entrance Counter

Just before the muons enter the vacuum chamber, there is an entrance counter which consists of two scintillators (called the μSc and μScA) and a small wire chamber (called the μPC).

The μSc counter is a 500 μm thick plastic scintillator and the μScA is a 3 cm thick plastic scintillator with a hole of 35 mm diameter. This and the collimator define

the shape of the muon beam as it enters the chamber. The anti-coincidence between these two counters is used to determine the number of incoming muons.

The μPC wire chamber consists of 24 X wires and 24 Y wires spaced 2 mm apart and provides data on the spatial distribution of the beam before it enters the chamber.

4.2.6 Vacuum Chamber

In order to use the high voltages required to operate the silicon detectors safely, the chamber has to be put under a pressure of 10^{-4} mbar. This was achieved by using a turbo pump kindly supplied by the PSI vacuum group.

4.2.7 Frontend Electronics and DAQ

A diagram of the AlCap hardware DAQ system is shown in Fig. 4.11 and shows how the various detectors, preamplifiers and digitisers are connected.

Amplifiers

The signals coming from the silicon and germanium detectors were split after preamplification into a "fast" and a "slow" channel. The pulses going through the slow channel were shaped by a shaping amplifier (Amp) and the pulses passing through the fast channel were shaped by a timing filter amplifier (TFA). Examples of these pulses are shown in Fig. 4.12.

The reason for having these parallel channels is so that a more precise measurement of the time of the pulses can be taken from the fast pulse, since the pulse peaks sharply, and a simpler measurement of the energy can be made from the slow pulse by measuring its amplitude.

For the scintillators, the signals were fed by light guides down to photomultiplier tubes (PMTs) which were then connected directly to the digitisers.

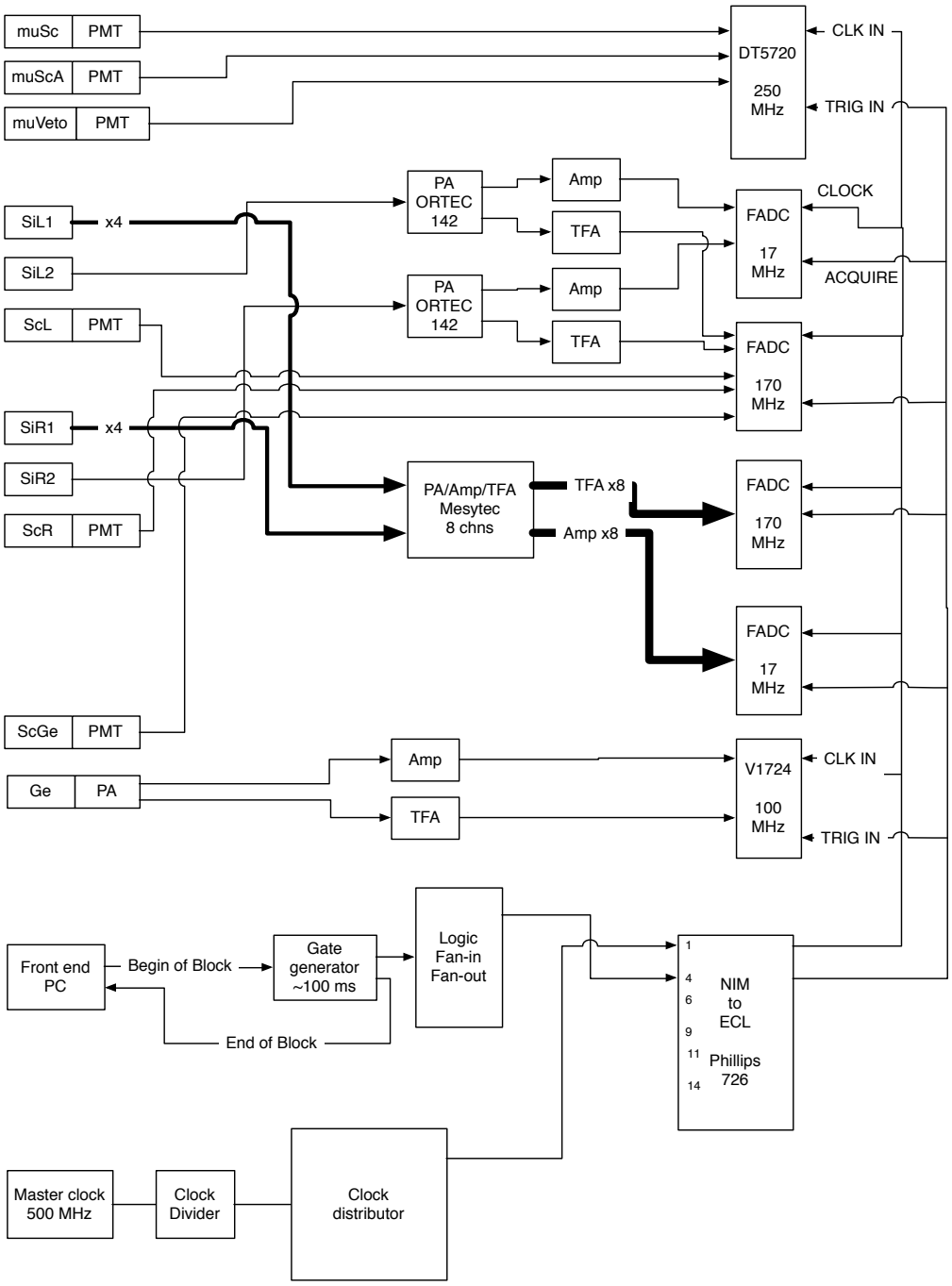

Figure 4.11: A diagram of the AlCap hardware DAQ system (note that the CAEN TDC and master run control are not shown).

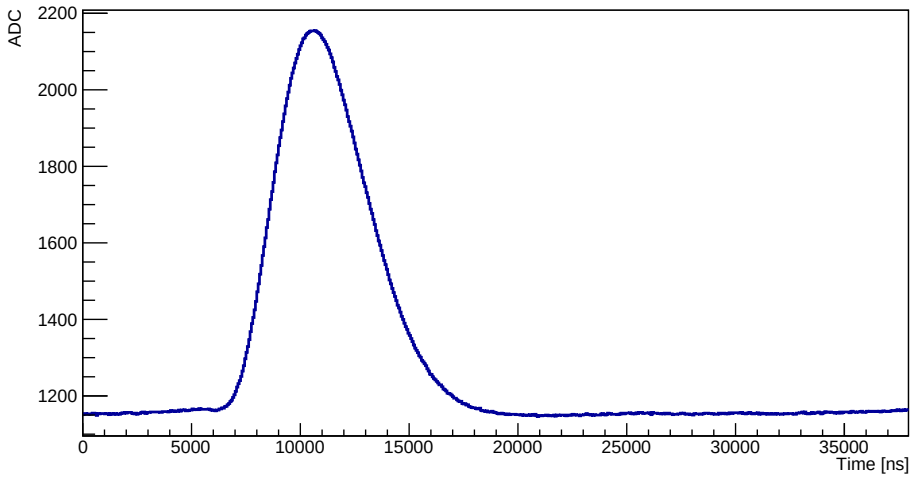

(a) Example Slow Pulse

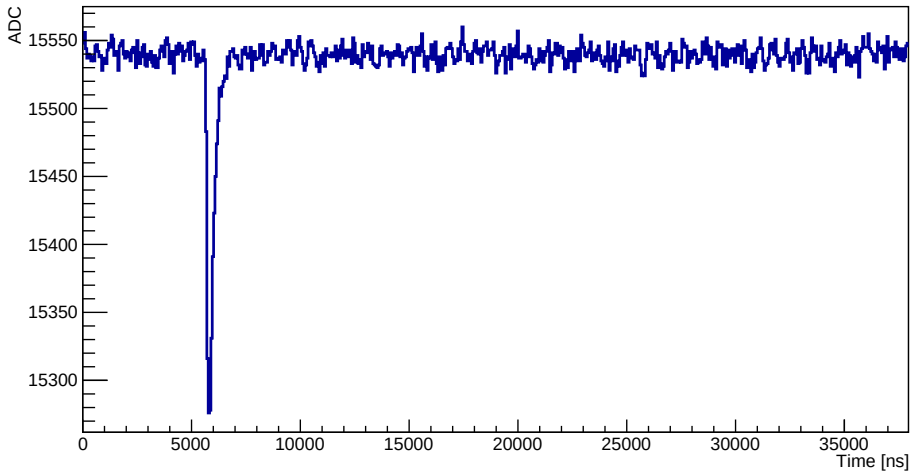

(b) Example Fast Pulse

Figure 4.12: Examples of (a) "slow" and (b) "fast" pulses in the germanium detector.

Digitisers

The analogue pulses created by the detectors were digitised using three different digitisers.

CAEN V1724

A VME module that digitises at a rate of 16 MS/s and encodes each sample in 14 bits. This module was used to digitise the pulses from the germanium detector since this detector produced larger peaks requiring 14 encoding bits to achieve acceptable resolution without overflows.

CAEN DT5720

A desktop module that digitises at a rate of 250 MS/s and encodes each sample in 12 bits. This module was used to digitise the pulses from the entrance counters and the veto scintillator since these produce very fast pulses and the extra sampling rate allows for reasonable digitised pulse shapes to be produced.

Flash ADC (FADC)

A custom built digitiser that digitises at a rate of 170 MS/s and encodes each sample in 12 bits. This module also has the capability of scaling down the sampling frequency on a channel-by-channel basis and so, for some of the slow channels, the sampling frequency was reduced by a factor of 10 to keep the total data rate down. Four of these boards were used to digitise the pulses from the silicon channels.

DAQ

The DAQ software was written using the Midas toolkit [73] and is used for the readout of the frontend electronics, event assembling, data logging, hardware control and writing to the run database. Some of these aspects were running on different machines and a diagram of the AlCap software DAQ architecture is shown in Fig. 4.13.

Data was collected almost continuously in a block structure, where each 110 ms block is stored in a single Midas event. All the events from a single run are collected into Midas (.mid) files which have a size limit of 2 GB. When this limit is reached a new run is started automatically and the old run is copied to archive.

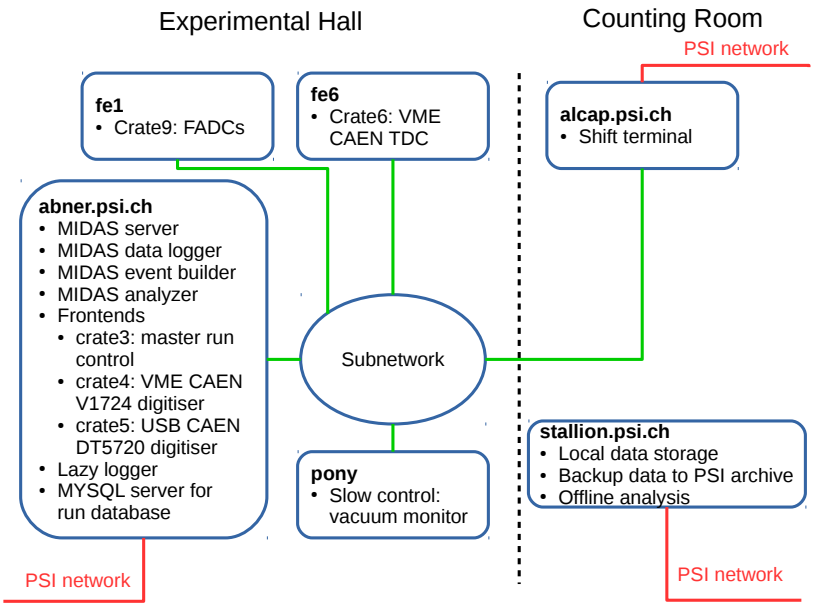

Figure 4.13: A diagram of the AlCap software DAQ architecture.

The data from each channel is written into a different Midas "bank", which is a block of memory labelled by a 4-character string. The naming scheme for these banks is as follows:

- The first character is either "C" (for one of the CAEN digitisers) or "N" (for one of the FADC digitisers).
- The second character corresponds to the channel number on that digitiser, where "a" is channel 0, "b" is channel 1 etc.
- The third and fourth characters indicate the specific board. For the CAENs, "BU" indicates the DT5720 provided by Boston University and "UH" indicates the V1724 provided by the University of Houston. For the FADCs, the last two characters were digits specifying the network address of the board in hexadecimal.

So, for example, the bank name Ne82 corresponds to the fifth channel (channel 4) on the FADC board at address 0x82.

In addition to the digitised pulse, each board provides a timestamp of when the pulse passed a hardware threshold. The timestamp is recorded as the number of digitiser clock ticks since the start of the Midas block.

The final thing that is also recorded into the Midas file is the runtime configuration of the experiment (e.g. channel mappings). All the information stored in the Midas online database (ODB) is stored both in the raw data file and as a text file for easier use in the offline analysis.

4.3 Software Framework

The software framework for the AlCap experiment consists of three programs. The first is `alcapana`, a Midas-based [73] program which is used for a quick, first stage analysis of the data. The second program is `rootana`, a Root-based [74] program that is used to perform the bulk of the offline analysis. The final program is the Monte Carlo simulation, built using the Geant4 toolkit [48, 49], and is used for all simulation purposes in AlCap.

4.3.1 `alcapana`

`alcapana` was written using the Midas toolkit with modules created to perform simple analyses on the raw Midas data files. This makes it suitable for online data quality monitoring plots that can be displayed on the shift computer. A screenshot of the online display is shown in Fig. 4.14.

The other use for `alcapana` is to convert the Midas files into Root files for use in `rootana`. During this process, the data is restructured so that each pulse is represented by a so-called `TPulseIsland` (`TPI`). This is a C++ class that contains the following member variables:

- a string specifying the Midas bank name;
- an integer specifying the time stamp of the pulse in digitiser clock ticks since the beginning of the Midas block; and

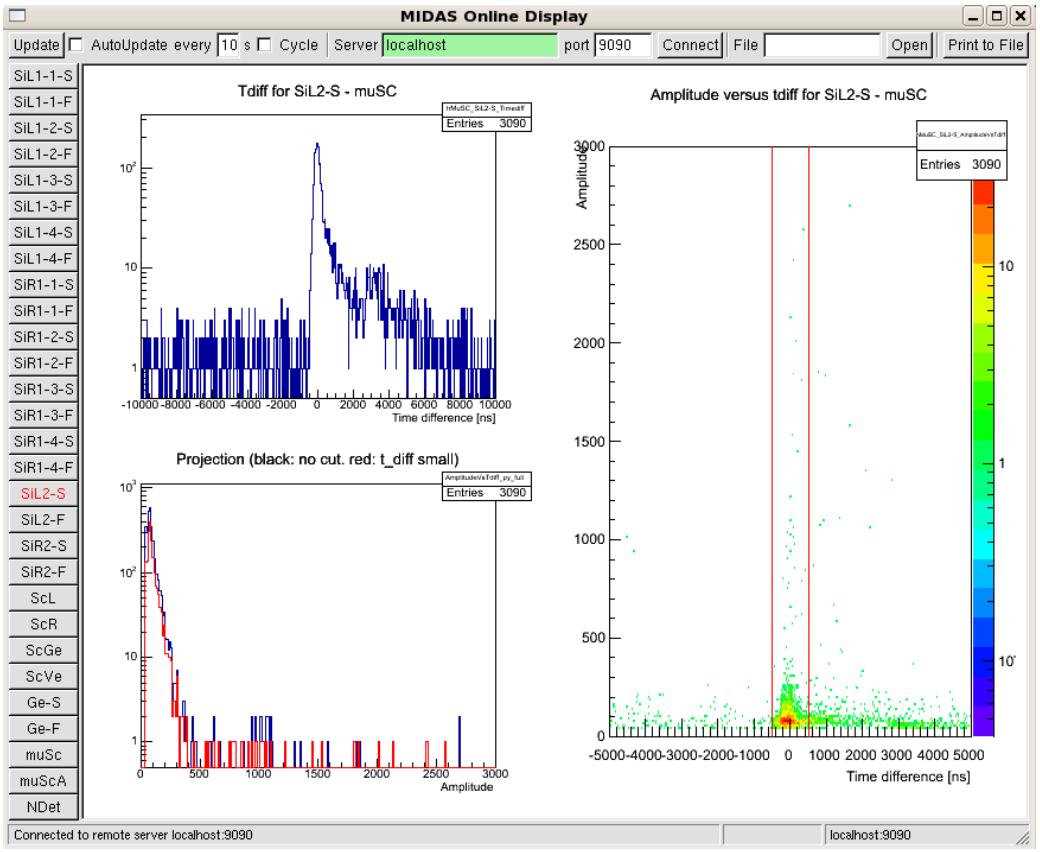

Figure 4.14: A screenshot of the AlCap online display showing some example plots. (Right): 2D plot showing the time difference of all hits in the μSc channel and all hits in the SiL2-S channel vs. the amplitude of the hit in the SiL2-S channel. This plot is monitored to ensure that the time difference is within the red lines. (Top-left): projection of the right-hand plot onto the x-axis. (Bottom-left): projection of the right-hand plot onto the y-axis with a cut on small time differences shown in red.

- a vector of integers corresponding to the time-ordered ADC samples of the pulse.

During this conversion, since a single real pulse may occur during the change-over between two Midas events, pulses with consecutive timestamps are stitched together to form a longer `TPI`. The data for each Midas block is then stored in a container which maps a Midas bank name to a vector of `TPI`s. Each Midas block is then stored as an entry in a Root tree and it is this tree that `rootana` uses for the analysis.

In addition to copying the data, `alcapana` also copies the runtime configuration that is stored in the online database (ODB). This is stored as a separate Root tree to the data and contains all the information relevant to that run (e.g. channel mappings) so that the `rootana` analysis can draw useful information from the data.

`alcapana` produces two files, a "hist" file, which contains all the histograms that the analysis modules have plotted, and a "tree" file which contains the data and runtime configuration and is the input file used by `rootana`.

4.3.2 `rootana`

`rootana` is the Root-based analysis program that is used to perform the majority of the offline analysis and is structured in such a way that the analysis flows through certain distinct stages that go from the digitised pulses to "physics" events.

In the first stage, waveform analysis is performed on the raw `TPI` to get a few important parameters of the pulse such as the amplitude and the time. This also gives a reduction in the data size and this reduced object is known as a `TAnalysedPulse` (`TAP`).

Next, `TAP`s from corresponding fast and slow channels are paired up to create `TDetectorPulse`s (`TDP`s) which represent a single physics event in that detector.

Finally, `TDP`s from different detectors are assigned to a pulse in the μSc entrance counter to create a `TMuonEvent` (`TME`). This is a more intuitive structure for the analysis since every detector event is related to a specific muon and so is the main data object used.

A diagram of the rootana analysis structure is shown in Fig. 4.15.

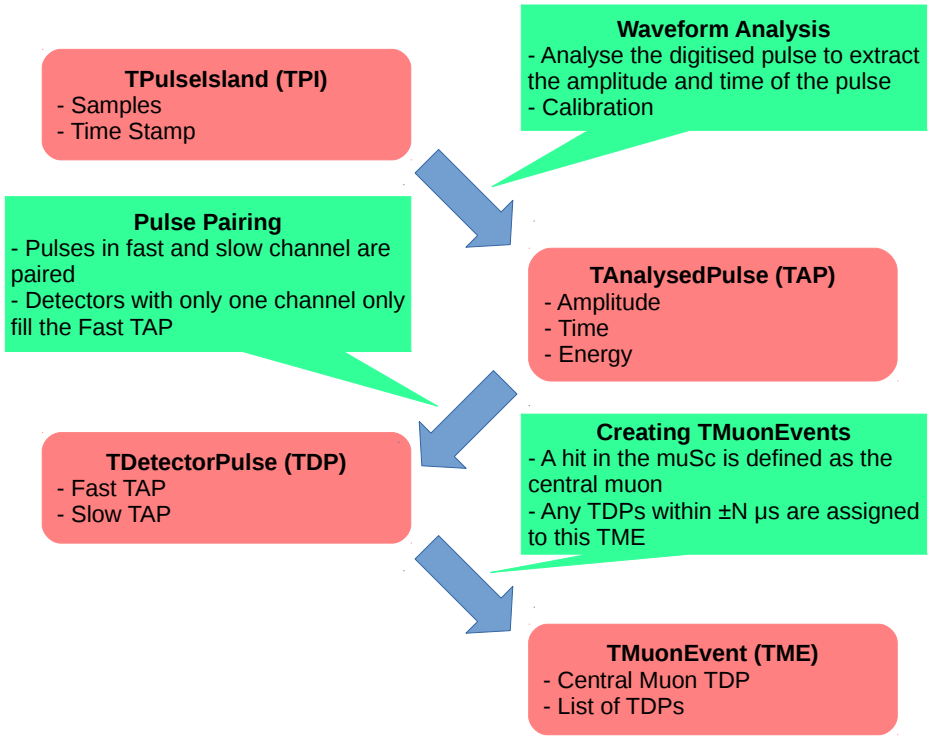

Figure 4.15: A diagram of the structure of the rootana analysis with the flow between TPIs, TDPs and TMEs shown. A rootana analysis module can be inserted at any point in this chain to analyse a given pulse type.

Waveform Analysis (TPIs → TAPs)

The first stage of the analysis is to convert the TPIs to TAPs by analysing the waveform and obtaining various pulse parameters. The most important of these are the time and the amplitude of the pulse and rootana has the functionality to easily switch algorithms for calculating these.

The amplitude of the pulse is given by a simple "max bin" method, where the peak of the pulse is taken as the height above pedestal of the maximum sample in the digitised pulse. Note that the pedestal is defined on a per channel per run basis and is obtained from taking the mean of the first five samples of the pulse.

The time of the pulse is given by a "constant fraction" method, which is defined as the time it takes the pulse to reach a certain fraction of its amplitude with interpolation between the two nearest samples being performed. This has the advantage that it gives a more consistent definition, particularly in slow pulses where the peak is broad and so the maximum bin could easily give a poor time resolution. The fractions used are defined on a channel by channel basis and are given in Table 4.2. These were determined by finding the fraction that gave the narrowest distribution in a plot of the time difference between hits in the channel and the μSc.

A diagram illustrating both of these methods on a particularly noisy pulse is shown in Fig. 4.16. Unfortunately, no data of known pulses shapes was taken to test these algorithms, which will be rectified in the next run.

Channel	Constant Fraction	Channel	Constant Fraction
μSc	0.60		
Ge-S	0.60	Ge-F	0.90
SiR2-S	0.60	SiR2-F	0.90
SiL2-S	0.60	SiL2-F	0.90
SiR1-1-S	0.60	SiR1-1-F	0.70
SiR1-2-S	0.40	SiR1-2-F	0.60
SiR1-3-S	0.90	SiR1-3-F	0.90
SiR1-4-S	0.70	SiR1-4-F	0.70
SiL1-1-S	0.50	SiL1-1-F	0.30
SiL1-2-S	0.30	SiL1-2-F	0.10
SiL1-3-S	0.40	SiL1-3-F	0.40
SiL1-4-S	0.70	SiL1-4-F	0.90

Table 4.2: The constant fractions used for each channel in determining the time of each pulse.

Also, in addition to the waveform analysis, it is at this stage that the pulses are calibrated. The time of the pulse is converted from clock ticks to nanoseconds by Eq. 4.2 and the energy of the slow pulse is obtained from its amplitude in ADC values with the precise conversion determined based on the calibration runs (see Sec. 4.4.3).

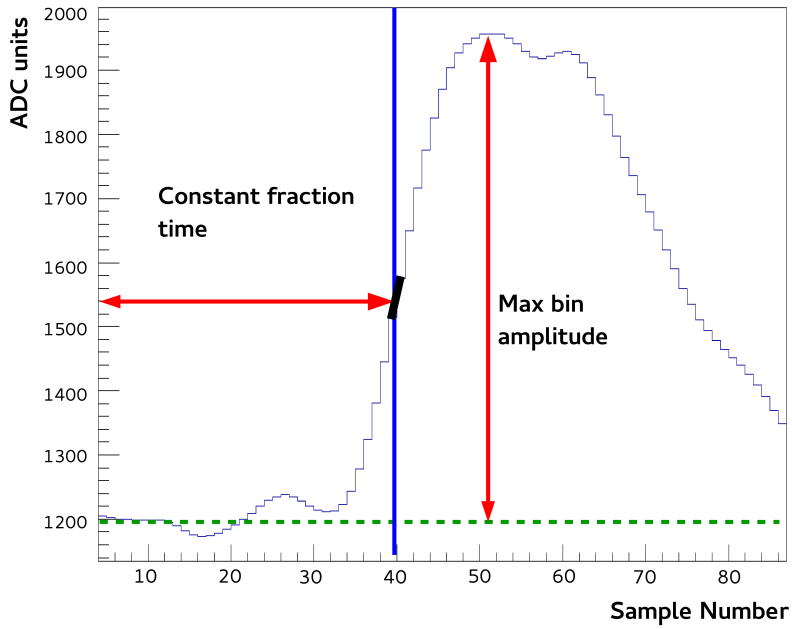

Figure 4.16: An illustration of the methods used in the waveform analysis to get the amplitude ("max bin") and the time ("constant fraction").

$$\text{time} = \frac{\text{number of clock ticks}}{\text{sampling rate of digitiser}}. \tag{4.2}$$

Another important aspect of the data that needs to be accommodated is that there may be more than one pulse on a `TPI` due to pile-up. Therefore, it may be necessary to split `TPI`s up into sub-pulses before the waveform analysis and so a "pulse candidate finder" was developed. Two different algorithms are implemented for this: the first algorithm is mainly used for slow pulses and just checks whether any sample in the digitised pulse goes above a simple amplitude threshold; and the second algorithm is for fast pulses and checks whether there has been a large change in ADC value of ~ 100 counts between two consecutive samples. If these conditions are met then the start of the pulse is registered and every subsequent sample is considered part of the pulse until the ADC value of a sample is lower than the pedestal and the end of the pulse is registered. Once the pulse has been defined, a few extra bins either side are taken to ensure the full pulse is collected. Some trivial examples are shown in

Fig. 4.17, however, this has not yet been looked into further and is not included in the analysis in Ch. 5.

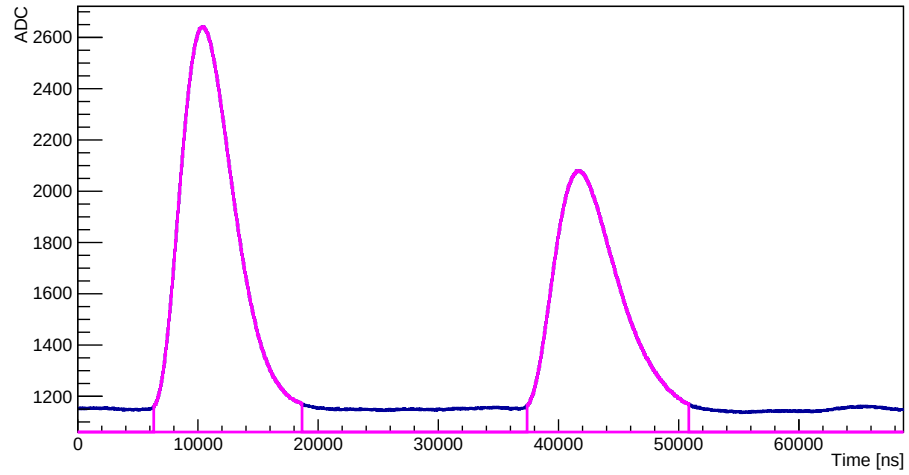

(a) Example Slow Pulses

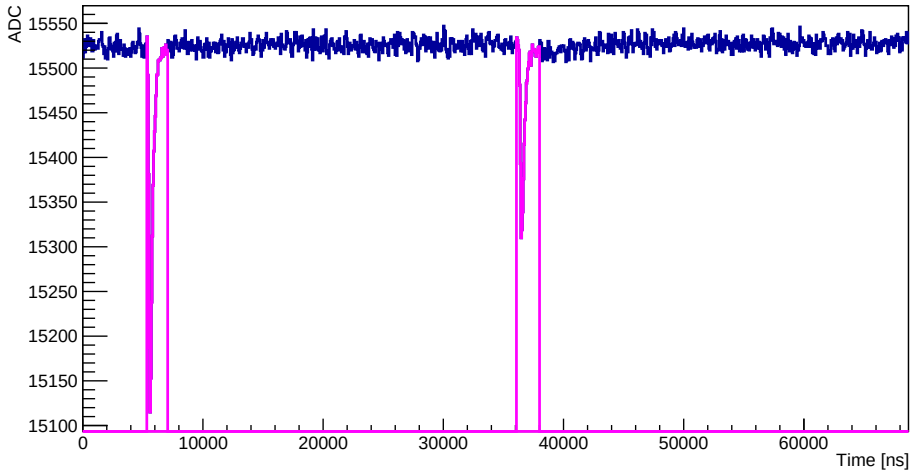

(b) Example Fast Pulses

Figure 4.17: Examples of pulses found by the pulse candidate finder for `TPIs` in the germanium fast and slow channels.

Pairing Fast and Slow Pulses (`TAPs` → `TDPs`)

Once the digitised pulses have been analysed and reduced to their important parameters, any detector that has both a fast and a slow channel (i.e. the silicon and

germanium detectors) should have these pulses paired so that there is a fast and a slow pulse in a single TDetectorPulse (TDP). The intention here is that this TDP then corresponds to a single physics event in the detector.

The algorithm works by iterating through the list of fast and slow TAPs on a given channel and finds which of them is the next pulse to occur. The algorithm then checks whether the next pulse in the other channel is close enough in time to be considered paired (typically 1 μs). If it is, a normal TDP is created and if it isn't, a TDP is created with only one TAP rather than two. It is worth noting that TDPs are written so that they can handle instances where the user asks for information of the slow pulse even if it does not exist for a given TDP.

For detectors with only one channel (e.g. the μSc counter) then this algorithm is not used and each TAP is placed into its own TDP.

Creating Muon Events (TDPs $\rightarrow$ TMEs)

Once each detector has a list of TDPs in that Midas block ($\sim$ 110 ms in length), TMuonEvents (TMEs) are created. This is done by looping through the hits in the μSc detector and, for each hit, collating all the TDPs from all detectors that occur within a certain time of it (typically 15 μs). This μSc hit is termed the central muon and, in order to ensure that all hits in the other detectors are caused by the same muon, a simple check is made to see if there is more than one TDP in the μSc channel for each TME. For all other channels, there is allowed to be more than one TDP in the TME and it is also possible that a single TDP is included in more than one TME.

4.3.3 Monte Carlo Simulation

A Monte Carlo simulation of the experiment has been developed using the Geant4 toolkit. A visualisation of the implemented geometry is shown in Fig. 4.18.

The simulation is written in such a way that most aspects of it can be easily modified by editing various configuration files. These files exist for the geometry, the initial particle distribution and the output variables.

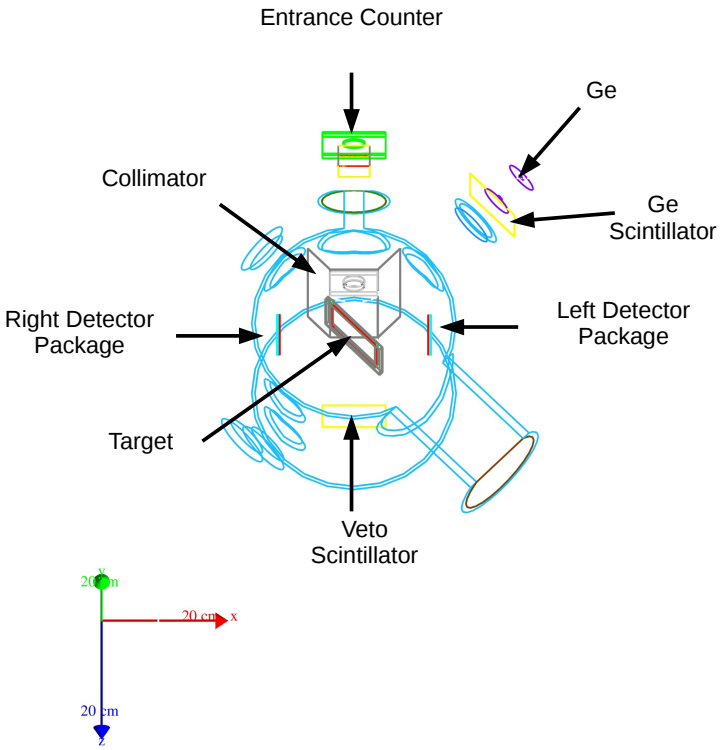

Figure 4.18: A visualisation of the AlCap Monte Carlo simulation showing the implemented geometry for an aluminium target. Note that the back wall does not appear due to a bug in the visualisation.

Geometry

The geometry configuration files define and place all volumes of the experiment. Some of these are placed within each other but ultimately they are all placed within the "world" volume. By editing this file, properties of each volume can be changed easily to suit the simulation study being done. For example, the thickness and material of the target can be changed to simulate the experimental set-up of a different dataset. It is also in this file that the so-called "sensitive" detector volumes are defined, where any particle passing through it will have some of its properties recorded and written to the output file.

Input

The configuration files for the initial particle distribution (also known as the "generator" configuration files) are used to define various aspects of the particles that are created at the beginning of the simulation including the particle type and the distributions of the starting position and initial momentum. These distributions can be defined as a uniform or Gaussian distribution with associated parameters or they can be stored in histograms and sampled from there. This is especially useful if the results of a previous simulation are available since this could improve the efficiency of the simulation. For example, after running a simulation where muons are fired at the target, a 3D histogram of the muon stopping positions can be created and used to define the starting positions of protons in another simulation.

Output

Finally, the output configuration file defines the variables that are read out of the simulation at the sensitive volumes. This includes, for example, each particle's momentum as it enters and leaves the volume or the amount of energy deposited in that volume. Also, certain conditions can be specified in this file so that only particles passing a certain cut will be recorded. This can aid in reducing the output file size and allowing more statistics to be collected if it is suitable for the study being done.

4.4 Run Summary

Data was collected from both silicon and aluminium stopping targets with the aluminium data being useful for Comet and Mu2e and the silicon data being collected so that a cross check with the data in the literature could be made.

For both materials, two different target thicknesses were used. In the silicon case, there was a thick, active target of 1500 μm thickness and a thin, passive target of 62 μm used; and for aluminium, targets of thickness 100 μm and 50 μm were used. A summary of the datasets collected is given in Table 4.3, where the beam momentum is given as a factor of 28 MeV (see Sec. 4.4.1) and the total number of muons is defined as the number that enter the experiment as counted by the μSc.

Target	Beam Momentum [$\times$28 MeV]	Integrated Run Time [h]	Number of Muons
Si (1500 μm) (Active Target)	1.30	10.3	2.89×10^8
Si (62 μm) (Passive Target)	1.06	10.5	1.72×10^7
Al (100 μm)	1.09	13.8	2.94×10^8
Al (50 μm)	1.07	43.0	8.81×10^8

Table 4.3: A summary of the data that was collected.

4.4.1 Beam Tuning

The beam had already been tuned by the MuSun experiment that was previously situated in the experimental area to a suitable momentum of 28 MeV. So, for AlCap, the currents in some of the magnets were simply scaled to achieve different beam momenta, the choice of this scaling factor was made by performing short runs at different scale factors and doing a preliminary analysis of the data in one of two ways.

For the thick silicon dataset, the energy deposited in the target could be analysed directly. From this information and comparing to a Monte Carlo simulation, the

stopping depth could be determined and a scale factor of 1.30 was selected since this meant that muons stopped towards the centre of the target.

For the passive silicon and aluminium targets, the choice of beam momentum was made based on a preliminary analysis of the X-ray spectra by trying to maximise the number of stopped muons. From this, scale factors of 1.06, 1.07 and 1.09 were chosen for the passive silicon target, the 50 μm aluminium target and the 100 μm aluminium target respectively.

The beam momentum spread ($\frac{\Delta p}{p}$) could be either 3% or 1% and the former was chosen since a higher muon rate was preferred to a narrower momentum spread.

4.4.2 Data Quality

During the run, the status of each run was recorded as either "Y" for candidate good data, "N" for bad data (for example, if it was noticed that a certain channel was malfunctioning) or "T" for test data. After the run, a report based on log book entries was compiled and recorded any changes to the experimental setup (e.g. any channels moving to different digitisers) and, based on this, the data quality flags were then redefined to "G" for golden runs, "B" for runs related to the beam (e.g. the momentum scan runs), "C" for calibration runs and "N" for unusable runs. The results of this classification are shown in Fig. 4.19.

Following this initial check, the golden runs were analysed in `alcapana` with modules written to determine the true quality of the data and to find any obvious errors that could be corrected or factors that would result in the run being demoted from the golden datasets. In addition, basic calibrations were performed. For example, because of all the different cable delays, the time in each channel needs to be shifted so that they all align with the μSc.

In order to check what the time shift should be, a plot such as that in Fig. 4.20 is produced and shows the time difference between all pulses in the μSc channel and the SiR2-S channel. The peak corresponds to where the channels are correlated and, as can be seen in Fig. 4.20a, this is not at zero and so time shifts are added on a channel-by-channel basis to correct for this as seen in Fig. 4.20b.

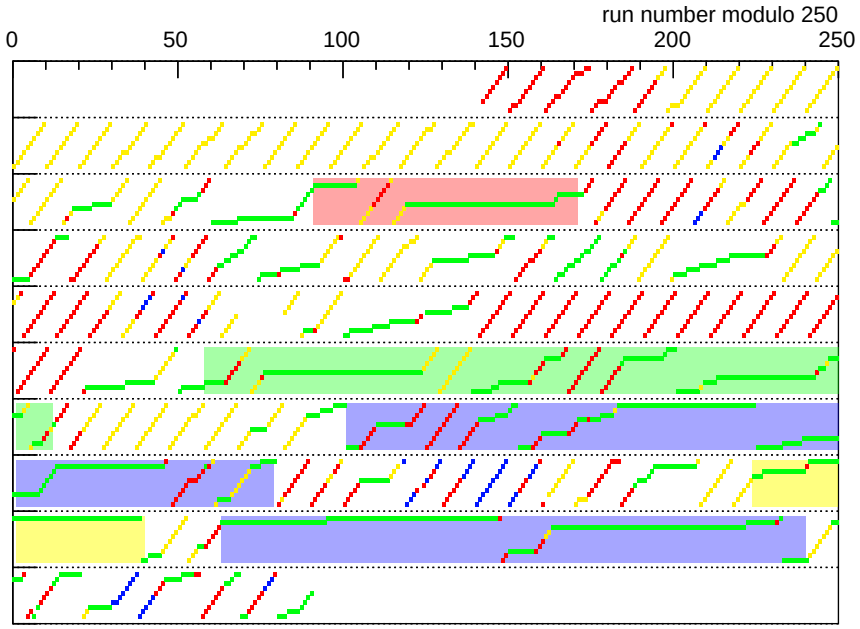

Figure 4.19: A plot of the data quality during the first AlCap run. Each block is one run where the colour indicates the data quality (red = bad run, yellow = beam run, green = golden run, blue = calibration run). Long sequences of runs at the same y-coordinate indicate runs that were autostarted due to the 2 GB limit on the Midas output file. The boxes show the final datasets given in Table 4.3: Si (1500 μm) (red), Si (62 μm) (yellow), Al (100 μm) (green) and Al (50 μm) (blue). Note that there are some runs that are deemed "golden" but are not included in any of the datasets because the beam was tuned to a different momentum. These runs may be useful to analyse at some future point.

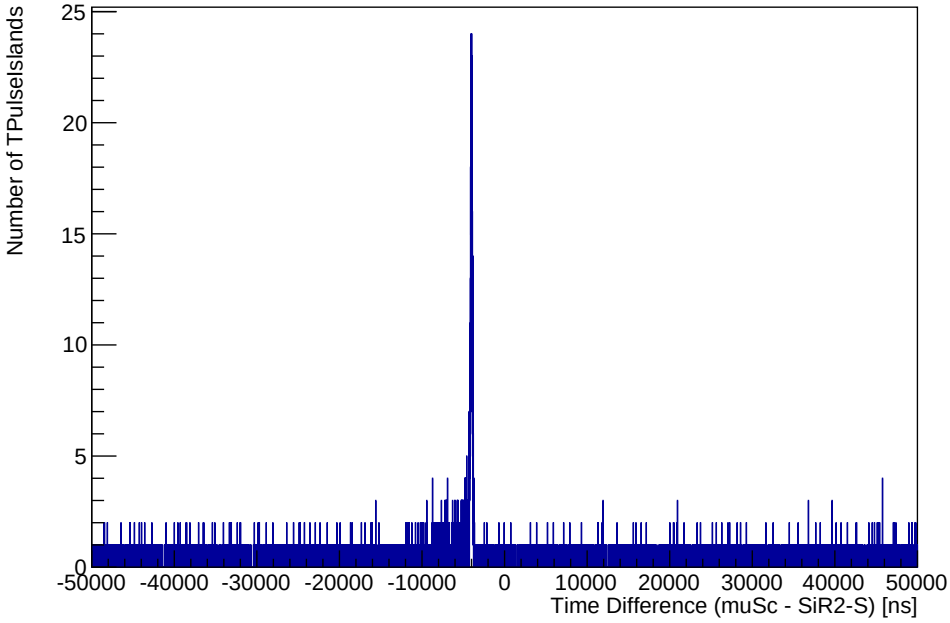

(a) before correction

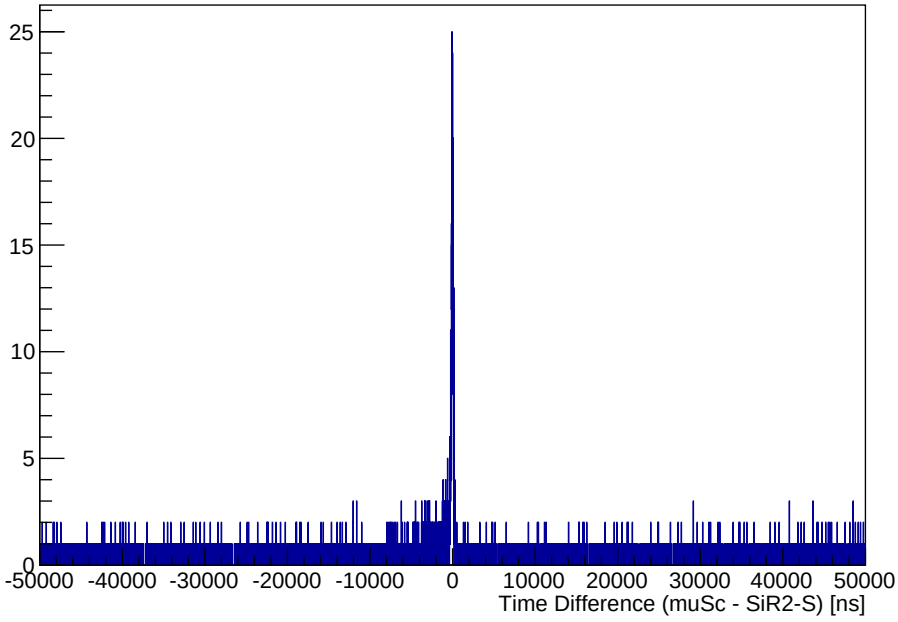

(b) after correction

Figure 4.20: Plots showing the time difference between all pulses in the μSc channel and the SiR2-S channel both (a) before and (b) after a corrective time shift has been applied.

In order to check large number of runs at the same time, the plots from each run were combined to create trend plots of each histogram for each dataset. An example trend plot is shown in Fig. 4.21 and shows that it is easy to see that the time shifts are all correct over the whole dataset.

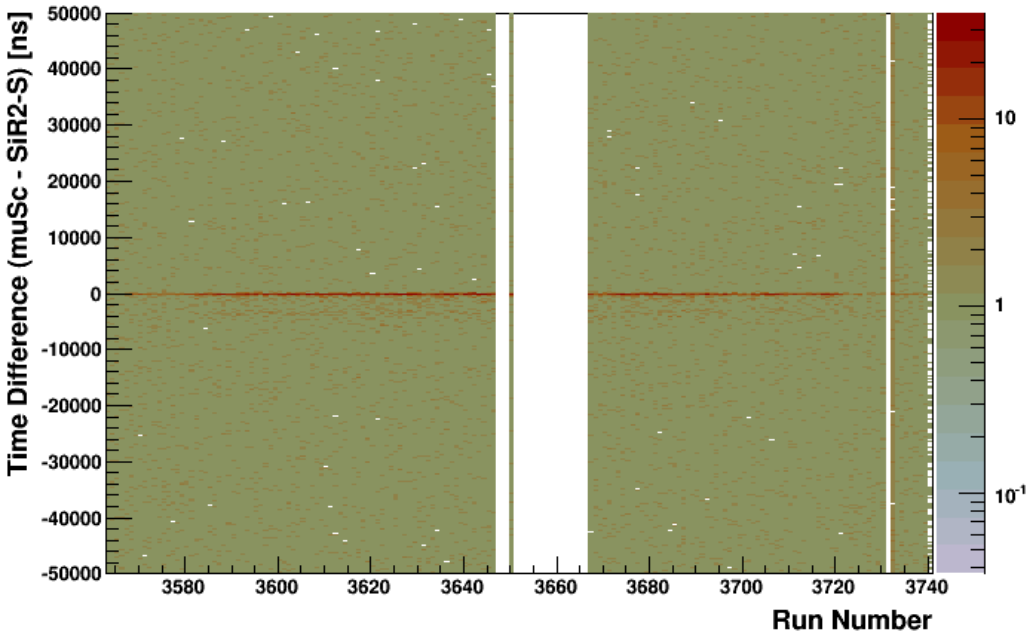

Figure 4.21: An example of a low level data quality trend plot (corresponds to Fig. 4.20).

During the low level data quality check some issues were discovered with the veto scintillators caused by the fact that the FADC they were plugged into was overflowing its data buffer very early into each Midas event and so subsequent data was lost from the scintillator. This makes it difficult to reliably use the scintillator as a veto and so is not included in the analysis in Ch. 5. This means that non-stopping proton band of Fig. 4.8 will appear.

4.4.3 Calibration Runs

In order to calibrate the energy of the detectors, some calibration runs were performed using various radioisotope sources with well-known energies.

Silicon Calibration

For the silicon detectors, a linear calibration was assumed and so only two points were used to obtain the calibration constants. In addition, there were many runs where momentum scan runs of the muon beam on the active silicon targets (which were, in reality, the detectors) and so it would be possible to double check this, however, this has not yet been done.

For both the thin and the thick silicon detectors the 5484 keV peak of an ^{241}Am α-source was used. It is worth noting that the thick silicon detector has a 0.5 μm thick, inactive layer. This means that alpha particles lose about 66 keV and so appear at 5422 keV.

For the thick silicon detectors, the other point used for the calibration is the MIP peak from beam electrons which was obtained from Monte Carlo. Since these calibrations were done when one of these detectors was rotated at 45° to the beam direction the MIP peak changes from 466 keV (see Fig. 4.22) to $\frac{466}{\cos(45°)} = 660$ keV. Also at this stage, a pulser was calibrated to simulate a 1 MeV energy deposit for use as a calibration point in the thin silicon calibration.

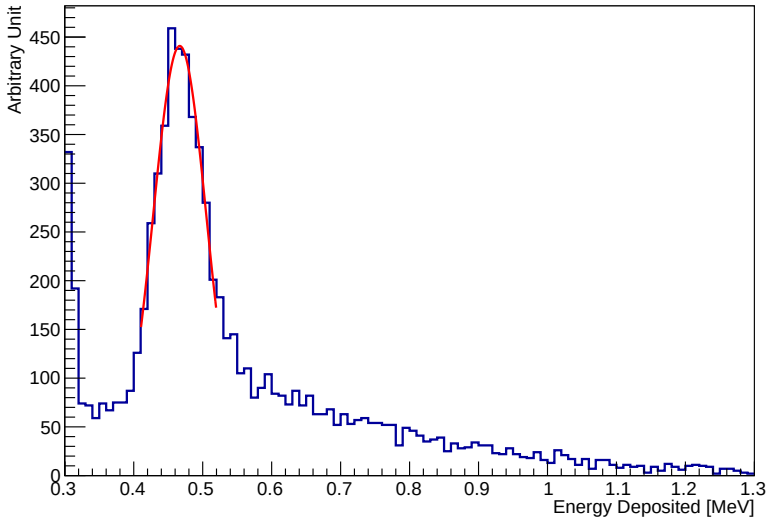

Figure 4.22: The energy deposited in the thick silicon detector by electrons (from Monte Carlo). The fit corresponds to the MIP peak and has a value of 466 keV.

The calibration constants for the silicon channels are given in Table 4.4.

Channel	Peak [keV]	ADC Value [ADC]	Slope	Offset
SiL2-S	5422	703.6	7.864	−111.23
	466	73.4		
SiR2-S	5422	703.9	7.963	−183.00
	660	102.1		
SiR1-1-S	1000	423.4	2.570	−87.97
	5485	2168.8		
SiR1-2-S	1000	428.4	2.660	−136.54
	5485	2114.5		
SiR1-3-S	1000	407.9	2.526	−30.20
	5485	2183.7		
SiR1-4-S	1000	429.5	2.570	−103.71
	5485	2174.8		
SiL1-1-S	1000	420.2	2.649	−113.17
	5485	2113.2		
SiL1-2-S	1000	408.3	2.577	−52.19
	5485	2148.7		
SiL1-3-S	1000	420.7	2.689	−131.06
	5485	2088.9		
SiL1-4-S	1000	420.3	2.580	−84.29
	5485	2158.8		

Table 4.4: The calibration constants for the silicon detectors.

Germanium Calibration

For the germanium calibration, a ^{152}Eu source was used. This source has many γ-ray lines which are listed in Table 4.5 along with their intensities and the calibrated ADC and efficiency values. The ADC values were obtained from a Gaussian fit close to where the peak was expected to be and the efficiencies were calculated as the number of counts seen divided by the number of expected counts, where the number of expected counts was derived from the known activity and age of the source. The energy calibration curve is shown in Fig. 4.23 and the efficiency curve is shown

in Fig. 4.24, where the differences in the error bars on each point are due to the intensities of the different γ-rays.

Energy [keV]	Intensity [%]	ADC Value	Efficiency [10^{-4}]
121.7817 ± 0.0003	28.41 ± 0.13	1000.7 ± 0.1	9.7 ± 0.1
244.6974 ± 0.0008	7.583 ± 0.04	2015.1 ± 0.2	6.7 ± 0.3
344.2785 ± 0.0012	26.58 ± 0.12	2831.3 ± 0.1	5.0 ± 0.1
411.1165 ± 0.0012	2.237 ± 0.010	3378.9 ± 0.5	4.1 ± 0.5
443.965 ± 0.003	3.125 ± 0.014	3647.8 ± 0.4	4.3 ± 0.4
778.9045 ± 0.0024	12.96 ± 0.06	6392.6 ± 0.2	2.5 ± 0.1
867.380 ± 0.003	4.241 ± 0.023	7117.5 ± 0.5	2.3 ± 0.2
964.072 ± 0.018	14.62 ± 0.06	7909.9 ± 0.2	2.2 ± 0.1
1085.837 ± 0.010	10.13 ± 0.06	8907.4 ± 0.3	1.9 ± 0.1
1089.737 ± 0.005	1.731 ± 0.010	8939 ± 1.0	2.3 ± 0.3
1112.076 ± 0.003	13.40 ± 0.06	9121.9 ± 0.2	1.9 ± 0.1
1212.948 ± 0.011	1.415 ± 0.009	9948.3 ± 0.8	1.6 ± 0.3
1299.142 ± 0.008	1.632 ± 0.009	10654.6 ± 0.9	1.7 ± 0.2
1408.013 ± 0.003	20.85 ± 0.09	11547.6 ± 0.2	1.5 ± 0.1

Table 4.5: The calibration data of the germanium detector taken using a ^{152}Eu source. The energies and intensities of the γ-lines used are taken from Ref. [75].

Using the fit parameters from the efficiency curve, the efficiencies of the $2p - 1s$ muonic X-rays for silicon (400.177 keV) and aluminium (346.828 keV) were found to be $(4.44 \pm 0.08) \times 10^{-4}$ and $(5.00 \pm 0.10) \times 10^{-4}$ respectively.

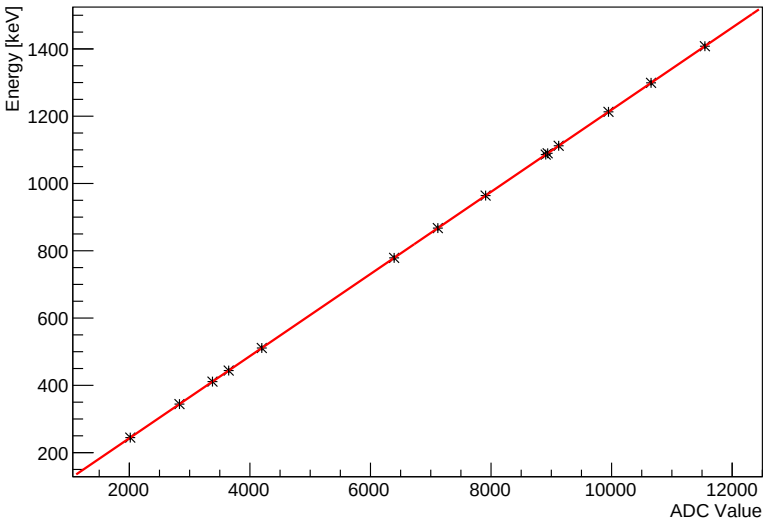

Figure 4.23: The germanium calibration curve. The curve was fitted to the distribution $y = mx + c$, where y is the energy, x is the ADC value and the parameters c and m were determined to be -1.25 ± 0.01 and 0.122042 ± 0.000002 respectively.

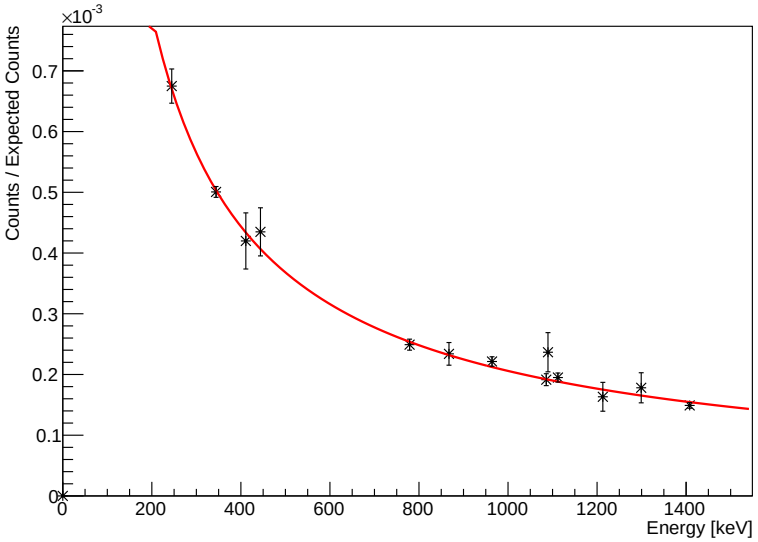

Figure 4.24: The germanium efficiency curve. The curve was fitted to the distributions $y = ax^b$, where y is the efficiency, x is the energy and the parameters a and b were determined to be 0.067 ± 0.008 and -0.84 ± 0.02 respectively.

Chapter 5

Rate of Proton Emission from a 50 μm Aluminium Target

"Determination that snail, say, is about to demonstrate (8)"
— Dante, *Financial Times #14524*

5.1 Overview

An analysis of the 50 μm aluminium target was performed with the aim of measuring the rate of proton emission following nuclear muon capture.

The rate of proton emission, R, is the number of protons, N_p, divided by the number of muons captured by the nucleus, $N(\mu^- p \to \nu_\mu n)$. This normalisation factor can be obtained by analysing the $2p - 1s$ muonic X-ray peak to get the number of stopped muons, $N_{\mu-stop}$, and then multiplying by the fraction of stopped muons that will be captured (0.609 [37]). Therefore, the rate of proton emission is given by Eq. 5.1:

$$R = \frac{N_p}{N(\mu^- p \to \nu_\mu n)} = \frac{N_p}{0.609\ N_{\mu-stop}}. \tag{5.1}$$

In the 50 μm aluminium dataset, there was a total of 292 MIDAS runs recorded with 8.81×10^8 muons passing through the μSc entrance counter. The beam momentum was 29.96 MeV and the $\frac{\Delta p}{p}$ was 0.362 MeV.

The following section describes the improvements made to the Monte Carlo in order to aid the analysis before going into more detail of the analysis itself.

5.2 Development of Realistic Input Mode for Monte Carlo

One of the first things to be developed after the run was a more realistic simulation of the muon beam for the Monte Carlo simulation using data collected from the entrance counter. In particular, the spatial distribution of the beam can be extracted from the μPC wire chamber as shown in Fig. 5.1.

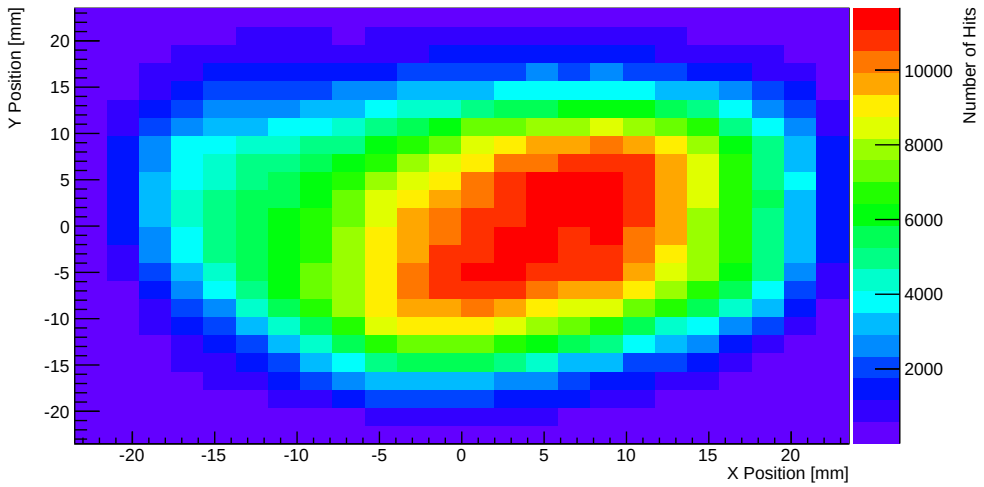

Figure 5.1: The spatial distribution of the beam as recorded by the μPC in one run. A slight skew to one side can be seen which was not initially implemented in the Monte Carlo simulation and is still to be understood.

In order to fully implement a realistic beam at the target it is also necessary to know how the beam disperses between the μPC wire chamber and the target. For this, a simulation of the beamline between the production target and the final focus was

provided by PSI using the TURTLE program [76] in the form of a PDF of the "beam envelope", which was digitised and is shown in Fig. 5.2.

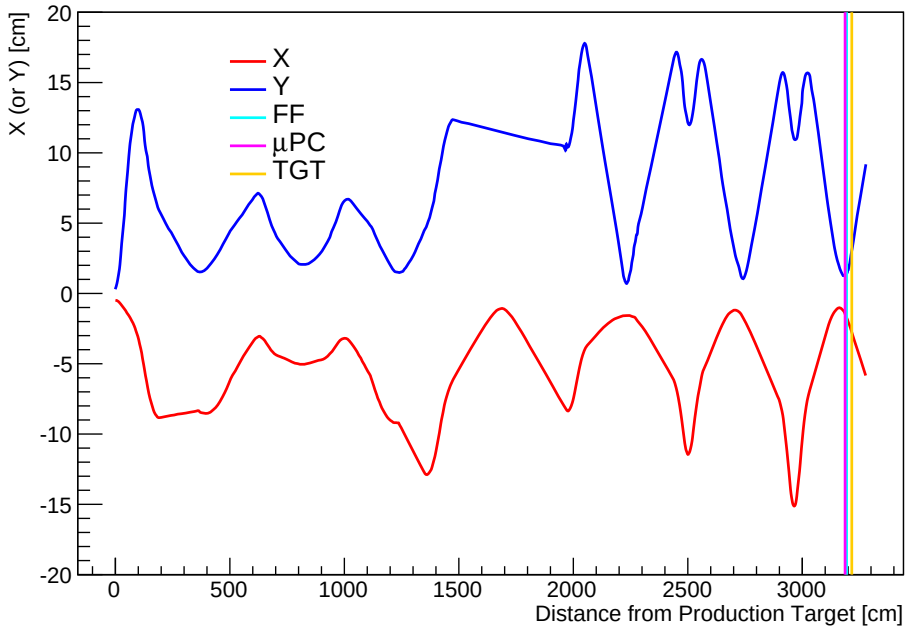

Figure 5.2: The digitised output of a TURTLE simulation of the beam envelope as it travels through the πE1 beamline (see Fig. 4.3). The locations of the μPC, final focus (FF) and target (TGT) are also shown. These are 67.5 mm, 120 mm and 353.08 mm from the end of the beampipe respectively.

There are two limitations to this: first, there is no information correlating the transverse momentum with position; and second, it is uncertain what the definition of the "beam envelope" is.

From the digitised envelope, the spread in x and y at the final focus[1], $(\delta x, \delta y)_{\mathrm{FF}}$ is $(12, 12)$ mm. Then, since there is no magnetic field beyond the end of the beampipe, the momentum envelope is taken to be the gradient of these slopes and so $(\delta p_x, \delta p_y)_{\mathrm{FF}} = (0.03, 0.1)$ rad.

Since it is uncertain how the beam envelope is related to the RMS spread of the beam, the μPC was used to determine this relation. At the location of the μPC, the

[1]Note that the final focus is not at the beam waist which is further upstream and closer to the μPC (see Fig. 5.3).

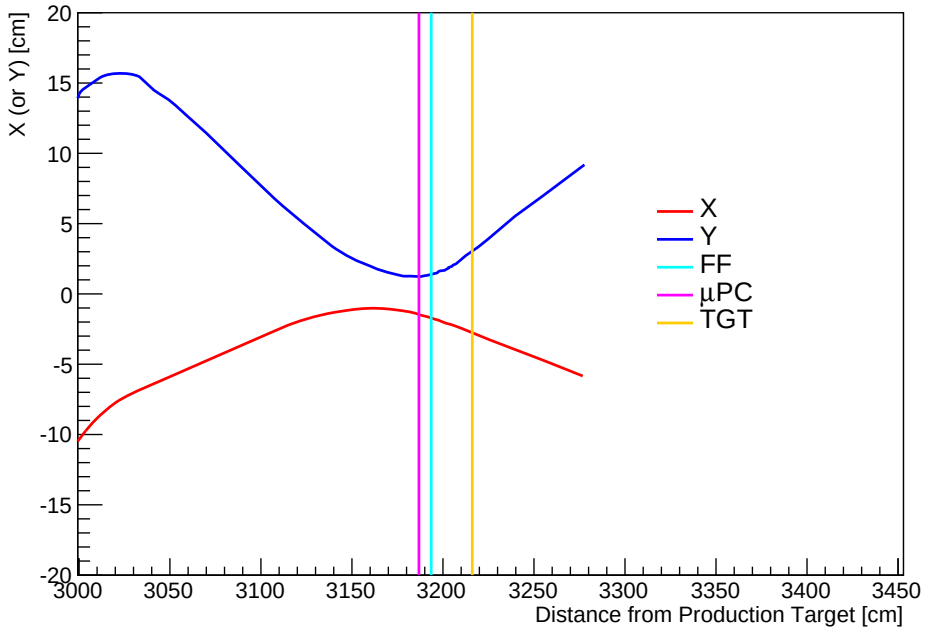

Figure 5.3: The digitised output of a TURTLE simulation of the beam envelope as it travels through the πE1 beamline (see Fig. 4.3). The locations of the μPC, final focus (FF) and target (TGT) are also shown. These are 67.5 mm, 120 mm and 353.08 mm from the end of the beampipe respectively.

change in δx and δy is given by $d \times (\delta p_x, \delta p_y)_{\mathrm{FF}}$, where d is the distance between the final focus and the μPC, which gives $\Delta(\delta x, \delta y)_{\mathrm{FF} \to \mu\mathrm{PC}} = (2.0, 6.8)$ mm.

Next, it can be assumed that, since the beam is transitioning from a converging beam to a diverging beam, that the position and momentum are uncorrelated near the final focus (i.e. the beam waist). This means that the changes in the spread can be subtracted in quadrature from the spreads at the final focus to give the spreads at the μPC: $(\delta x, \delta y)_{\mu\mathrm{PC}} = (11.8, 9.8)$ mm.

Comparing this to the RMS given in the data from the μPC ($(10.8, 8.9)$ mm) shows that the envelope is about 10% bigger than the RMS spread. Assuming that the relation between the envelope and the RMS spread is the same for momentum then $(\delta p_x, \delta p_y)_{\mu\mathrm{PC}} = (0.033, 0.11)$ rad.

Using all of this information, two input modes for the Monte Carlo were created. The first mode (known as the "muPC" mode) generates initial muons at the end of the beampipe. The second mode (known as the "collimator" mode) generates initial muons just after the lead collimator so that the efficiency of the simulation can be improved if it is only stopped muons that are important for the given study.

5.2.1 Implementation of muPC Input Mode

The "muPC" mode is implemented in the following steps:

- a random (x, y) position is selected from the histogram in Fig. 5.1;
- a random p_z is selected from a Gaussian distribution with the momentum amplitude and spread given by the 28 MeV scale factors of Table 4.3;
- a Gaussian distribution is used to obtain the values of p_x and p_y where the means of the distributions are based on the results of the previous section (i.e. $\langle p_x \rangle = 0.033 p_z$ and $\langle p_y \rangle = 0.11 p_z$);
- using these momentum components and the (x, y) position at the μPC, the starting position is projected back to the end of the beampipe, where the muon is instantiated.

To validate this input mode, a simulation of 500×10^3 muons was performed. In this simulation, it was found that the fraction of incoming muons that were stopping in

the 50 μm aluminium target was $4.63 \pm 0.04\%$. This is significantly less than the value found in the X-ray analysis of the data (see Sec. 5.4) which was $6.47 \pm 0.01\%$. This affects the stopping distribution of muons in the target however, this will not affect the final result since this will be normalised to the number of stopped muons. It is believed that the discrepancy arises because of the uncertainty in the amount of passive material in between the end of the beampipe and the target and there is work underway using the momentum scan runs of the active silicon target to determine this more accurately. This will also be solved in the next run by carefully accounting for all upstream material. The momentum distribution of the stopped and incident muons is shown in Fig. 5.4.

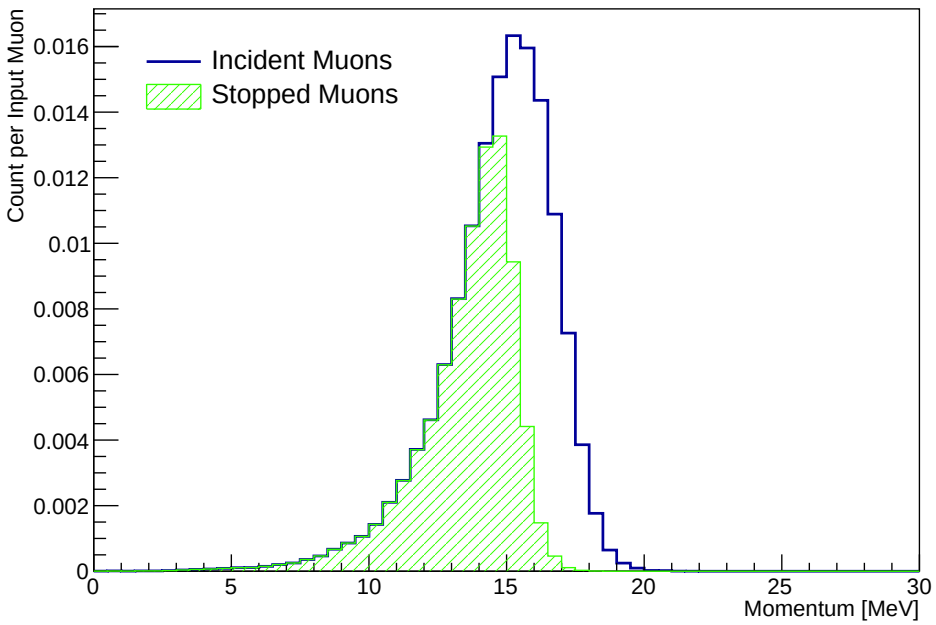

Figure 5.4: A plot showing the Monte Carlo momentum distribution of muons that stop in and are incident on the 50 μm aluminium target. For reference the initial muon momentum upon leaving the beampipe is 29.96 MeV/c.

5.2.2 Implementation of Collimator Input Mode

The "collimator" input mode is implemented in much the same way as the "muPC" input mode except for two important differences:

- the initial position of the muon is projected forward from the μPC to just after the collimator (195.08 mm downstream of the μPC); and
- an amount of kinetic energy determined from a simulation is subtracted from the nominal value to account for energy loss.

In order to know how much energy muons lose when travelling from the end of the beampipe to the collimator, a simulation on the above "muPC" mode was performed and the kinetic energy of the muons was recorded in a software monitor placed after the collimator. Fig. 5.5 shows the energy lost by muons of momentum 29.96 MeV after passing through the material upstream of the collimator: the entrance counter and the cover on the chamber port. A function consisting of a combination of a Landau, an exponential and a Gaussian was fitted to this distribution and hard-coded into the "collimator" input mode.

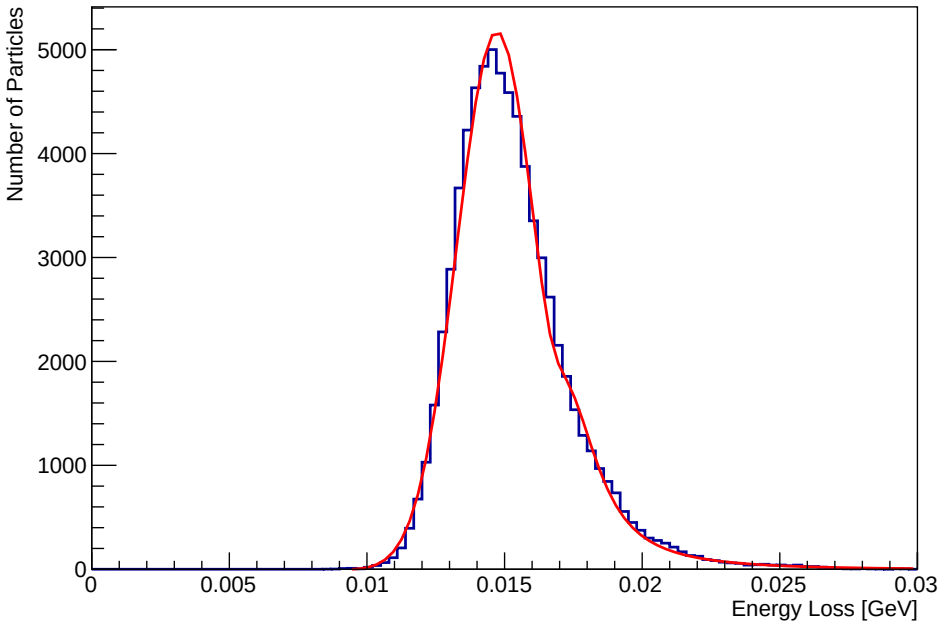

Figure 5.5: A plot showing the energy loss of muons with momentum 29.96 MeV between the end of the beampipe and just after the lead collimator. The fit used in the "collimator" input mode is shown as well.

5.2.3 Stopped Muon Position Distribution

Using the above "collimator" mode it is possible to efficiently record the stopping positions of a large number of muons for use later in the analysis (see, for example, unfolding in Sec. 5.5.4).

A simulation of 20×10^6 muons was performed and their stopping positions in the target were recorded into a 3-dimensional histogram which was used to sample starting positions in subsequent simulations. Fig. 5.6 shows the stopping depth of muons within the 50 μm aluminium target with the beam entering from the left.

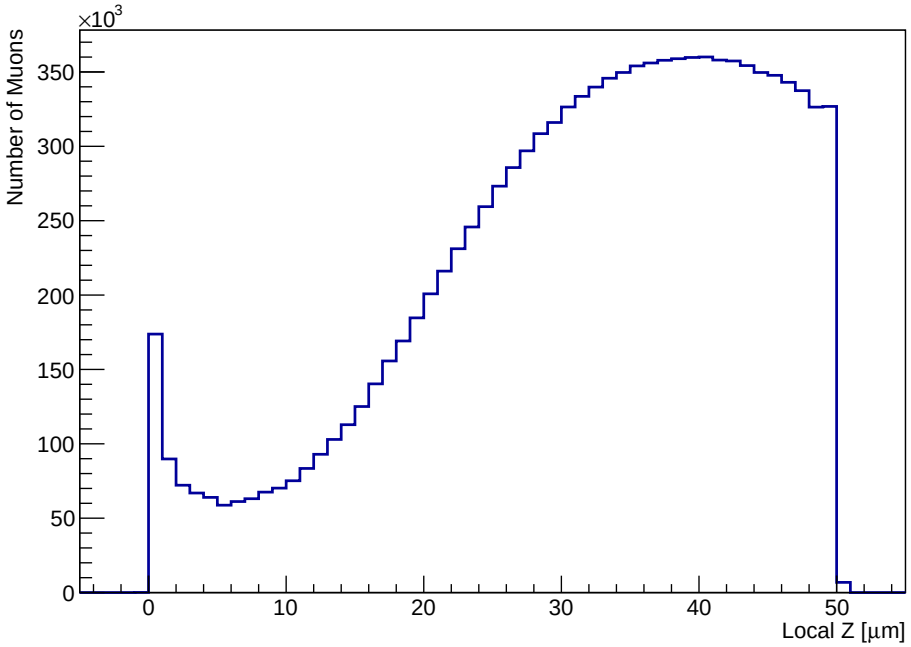

Figure 5.6: A plot showing the Monte Carlo stopping depth of the muons in the 50 μm aluminium target (perpendicular to the face of the target. i.e. muons travel $\sqrt{2}$ further). The beam enters from the left and the peak immediately as the beam enters is from low momentum muons being stopped straight away.

5.3 Muon Definition

In this analysis, a muon is defined as any hit in the μSc counter with an amplitude greater than 230 ADC (see Fig. 5.7) and has no other hits in the μSc within 15 μs. This results in a total of 6.03×10^8 incoming muons in the 50 μm aluminium dataset.

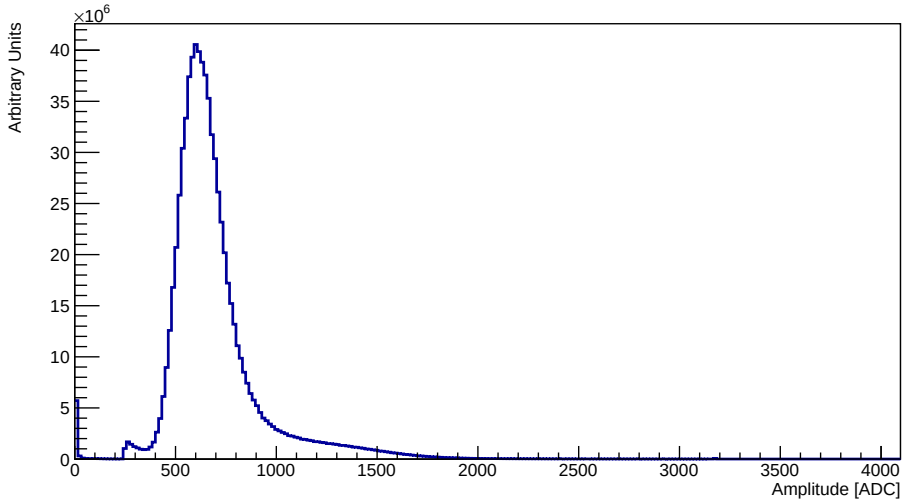

Figure 5.7: The amplitude spectrum of pulses in the μSc detector. The muon peak can be clearly seen and a cut above 230 ADC is used to define the incoming muons. The odd behaviour at amplitudes below this is an artefact of the digitiser used for this channel and arises from the fact that the digitiser reads out all of its channels, even if only one of the channels passes its hardware threshold.

5.4 Stopped Muon Analysis

5.4.1 X-Rays

In order to determine the number of stopped muons and obtain the number of muon captures for normalisation, an analysis of the X-ray spectrum recorded by the germanium detector was performed.

After a muon is captured by an atom, it transitions down to the $1s$ state and, as it falls, it emits photons of characteristic energies. For aluminium, the peak of interest is the $2p - 1s$ peak at 346.8 keV which accounts for 79.8% of the emitted X-rays

as given in Table 4.1. Fig. 5.8 shows the full spectrum recorded by the germanium detector in this dataset.

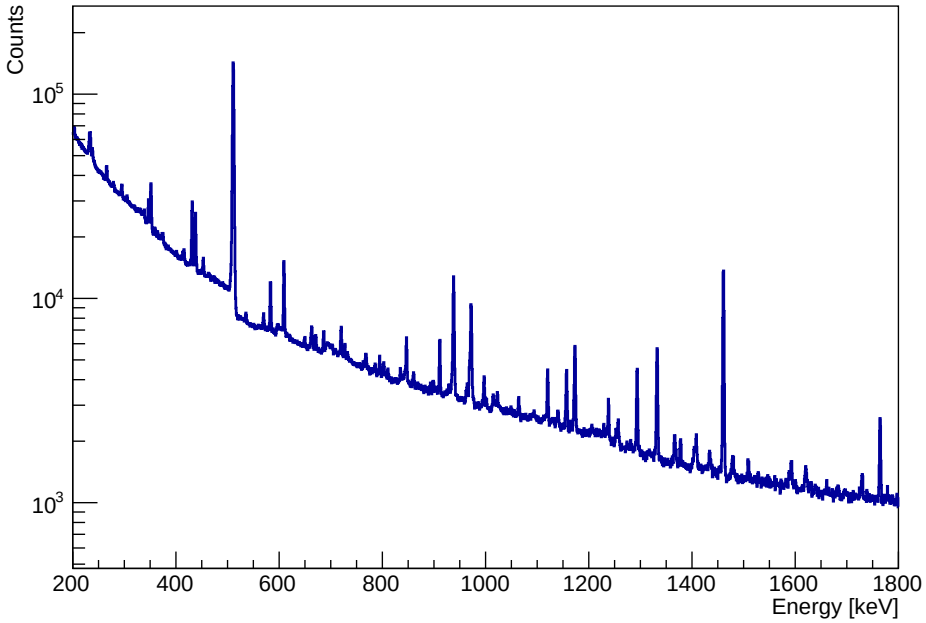

Figure 5.8: The full calibrated X-ray spectrum recorded by the germanium detector for this dataset. Note that these are the raw counts (i.e. the efficiencies calculated in Sec. 4.4.3 have not been included).

The region of interest around the $2p - 1s$ aluminium peak is shown in Fig. 5.9. In this figure, two peaks can be seen. The peak on the left is the $2p - 1s$ aluminium X-ray and the peak on the right is from a long-lived intermediate state after lead capture. Looking in three time bins, it can be seen that the aluminium peak only appears at early times since the muons stop in the aluminium and emit photons almost immediately. The background peak is much longer lived and so, in order to isolate the aluminium $2p - 1s$ peak, a time cut of less than 500 ns relative to the entering muon was used.

In order to obtain the number of X-rays, a double Gaussian with a linear background was fitted to the prompt spectrum in the region 340 keV to 356 keV. The result is shown in Fig. 5.10. As can be seen, the energy of the peak agrees with the value given in Table 4.1 and the pertinent parameters of the aluminium peak were found to be:

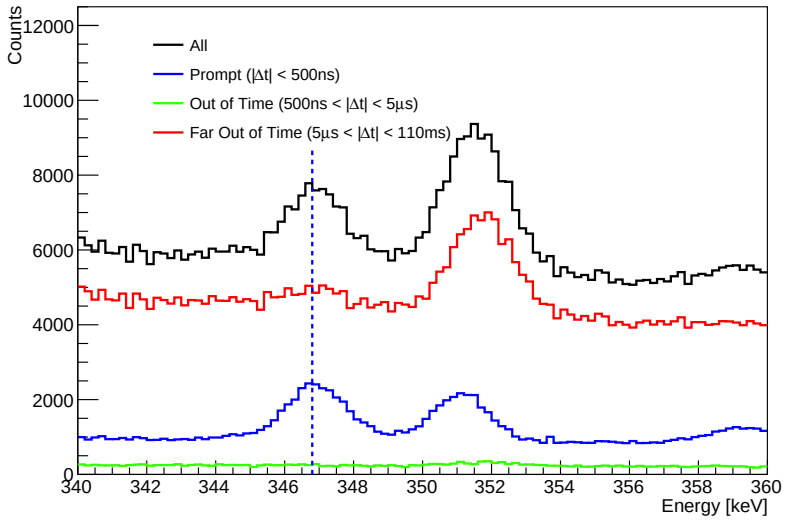

Figure 5.9: The X-ray spectrum in the region around the aluminium $2p-1s$ peak (indicated by dotted line) in three time bins: prompt ($t < 500$ ns, blue), out of time (500 ns $< t <$ 5 μs, green) and far out of time (5 μs $< t <$ 110 ms, red). The upper limit of 110 ms is due to the MIDAS event length (see Sec. 4.2.7).

$$A = 1450 \pm 20; \quad \sigma = 0.90 \pm 0.01 \text{ keV};$$

Finally, the number of muon stops is given by Eq. 5.2, where I is the intensity of the muonic X-ray (0.798 from Table 4.1), ε is the efficiency of the germanium detector at this energy ($(5.00 \pm 0.10) \times 10^{-4}$ from Fig. 4.24), A and σ are the amplitude and sigma parameters of the above fit and w is the width of the bin (0.2 keV).

$$N_{\mu-stop} = \frac{N_{X-rays}}{I\varepsilon} \tag{5.2}$$

$$= \frac{A\sigma\frac{\sqrt{2\pi}}{w}}{I\varepsilon} \tag{5.3}$$

Using these numbers gives the number of stopped muons as $(41.0 \pm 0.9) \times 10^6$ in the full dataset, which corresponds to a stopping rate of $6.47 \pm 0.01\%$ and, using the fraction of stopped muons that will be captured by the nucleus, the total number of muon captures is $0.601 \times (41.0 \pm 0.9) \times 10^6 = (24.6 \pm 0.5) \times 10^6$.

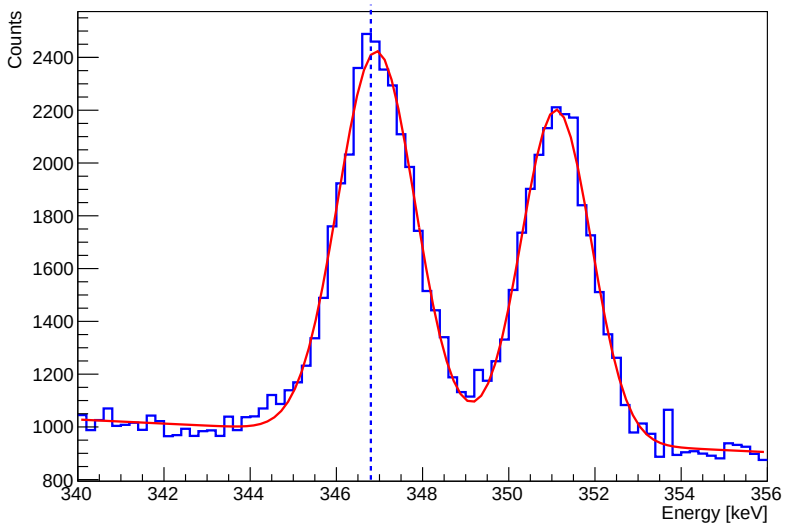

Figure 5.10: The prompt spectrum around the aluminium $2p-1s$ X-ray peak with the double Gaussian fit that was used to obtain the number of X-rays. The dotted line indicates the energy of the aluminium $2p-1s$ peak.

5.4.2 Systematics

The main systematic in counting the number of X-rays is from the timing cut used. To obtain a systematic uncertainty this was reduced from 500 ns to 400 ns and the fit was performed again. The resulting parameters of this fit are shown in Table 5.1 along with the original values from the 500 ns cut.

Time Cut [ns]	A	σ [keV]	$N_{\mu-stop}[\times 10^6]$
500	1450 ± 20	0.90 ± 0.01	39 ± 1
400	1440 ± 20	0.90 ± 0.01	38 ± 1
Relative Uncertainty [%]	–	–	2.6

Table 5.1: The fit parameters for the X-ray analysis for different time cuts and the relative uncertainty in the number of stopped muons.

5.4.3 Final Number of Stopped Muons

Taking into account all uncertainties, the total number of captured muons is found to be $(24.6 \pm 0.5\ (\text{stat.}) \pm 0.6\ (\text{syst.})) \times 10^6$.

5.5 Proton Analysis

The next step in determining the rate of proton emission is to obtain the number of protons that were detected in the silicon detectors. In this analysis, only the slow channels of the silicon detectors were analysed since the fast channels were particularly noisy. Therefore, in terms of the framework described in Sec. 4.3.2, the pairing up of fast and slow channels was not done and the slow channels were passed straight through to the final `TMuonEvent` stage.

5.5.1 Timing Cut

Directly after the `TME`s have been created, there are two important backgrounds that need to be addressed. The first is from muons that scatter directly into the silicon detector and stop, producing protons when captured by the silicon nucleus. The second background arises from muons stopping in lead and being captured by a lead nucleus. Both of these backgrounds are mitigated by removing any `TME` that contains a hit in any silicon channel that occurs less than 100 ns after the muon enters the chamber. The choice of 100 ns was made because the muonic atom lifetime of lead is 80 ns and the time of flight of a muon with momentum 29.96 MeV is $\mathcal{O}(5\text{ ns})$.

In order to determine the efficiency (ε) of this cut and the purity (P) of the remaining sample (as defined in Eq. 5.4), the Monte Carlo simulation described in Sec. 5.2.3 was analysed. Since the Monte Carlo simulation does not include the time resolution of the detectors, a time resolution smear was added afterwards to account for this.

$$\varepsilon = \frac{N_{\text{p from Al after cut}}}{N_{\text{total p from Al}}} \quad P = \frac{N_{\text{p from Al after cut}}}{N_{\text{total after cut}}}. \tag{5.4}$$

The time resolutions were found by plotting the time difference between hits in the silicon channels and the μSc and fitting a Gaussian to the peak (see an example in Fig. 5.11). Although the full distribution is not Gaussian, it is only the peak that contains hits that are prompt with the μSc and give an indication of the resolution of the detector. The limits for each fit were -150 and $+150$ ns and the resulting resolutions of each channel are given in Table 5.2. These show that the thick silicon detector has a time resolution of 80.1 ± 0.4 ns and the average resolution of the thin silicon detectors is 169 ± 32 ns. Adding these in quadrature gives a final resolution of 187 ± 32 ns and so the arrival times of all particles in the Monte Carlo were smeared with a Gaussian of this spread.

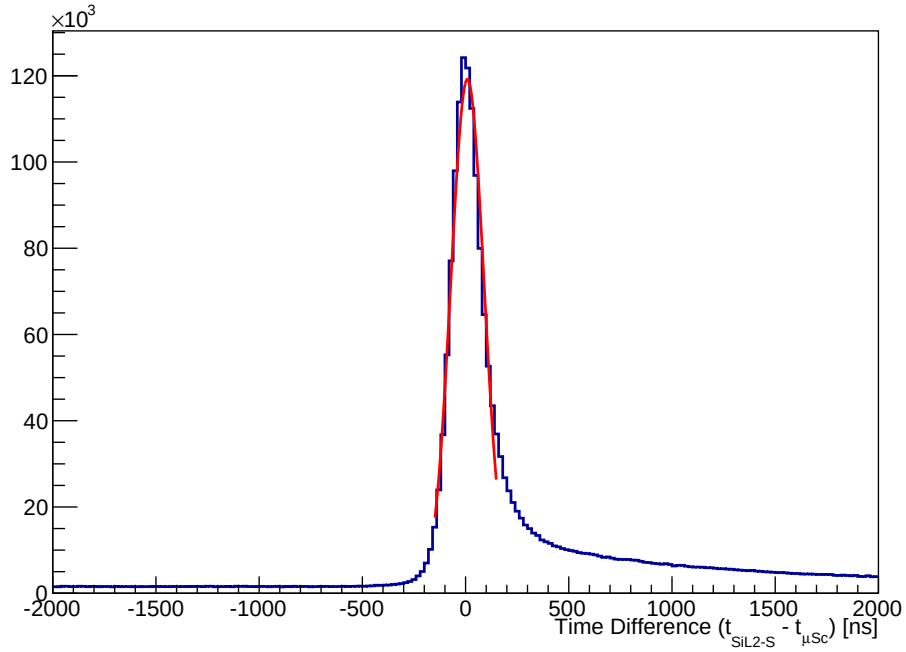

Figure 5.11: A plot of the time difference between the SiL2-S channel and the μSc channel. The Gaussian fit corresponds to the resolution of that channel.

Plots of the arrival times (with smearing) of muons, protons that originated in lead and protons that originated in aluminium were made (Fig. 5.12) and integrated to obtain the efficiency (ε) and purity (P) of the cut. These were found to be 0.870 ± 0.004 and 0.936 ± 0.005 respectively.

Channel	Resolution [ns]	Channel	Resolution [ns]
SiL2-S	80.37 ± 0.08	SiR2-S	79.84 ± 0.08
SiR1-1-S	132 ± 1	SiL1-1-S	158 ± 2
SiR1-2-S	159 ± 2	SiL1-2-S	145 ± 3
SiR1-3-S	150 ± 2	SiL1-3-S	203 ± 5
SiR1-4-S	178 ± 3	SiL1-4-S	227 ± 6

Table 5.2: The timing resolution of each silicon channel.

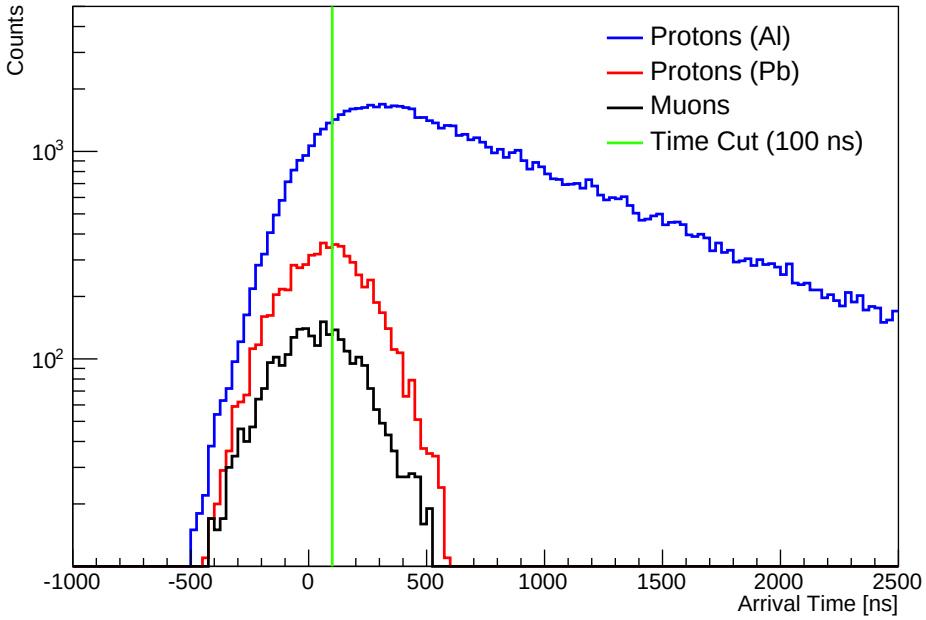

Figure 5.12: The arrival times of scattered muons (black), protons from lead (red) and protons from aluminium (blue) as well as the 100 ns time cut that was applied (green). The arrival times have been smeared by a Gaussian of width 187 ns.

5.5.2 E_1 vs $(E_1 + E_2)$ Plots

Particle identification is performed by plotting the energy deposited in the thin silicon layer (E_1) against the energy deposited in both the thin and the thick layers ($E_1 + E_2$). These E_1 vs $(E_1 + E_2)$ plots were created by looping through all the pulses in the silicon channels in each `TME` and making the following cuts:

- energy deposited in the thick silicon layer is greater than 100 keV;
- energy deposited in the thin silicon layer is greater than 100 keV; and
- time difference between the thick and the thin hit is less than 500 ns.

The E_1 vs (E_1+E_2) plots for each detector arm are shown in Fig. 5.13 and have a few interesting features. The first is the electron spot in the bottom-left which consists of very few bins with a very high number of entries. Immediately surrounding this is a larger region which corresponds to the remaining muons that scatter directly into the detector. Finally, the proton, deuteron and alpha bands can be clearly seen. The alpha band has a flat top due to pulses overflowing the digitisers.

5.5.3 Extracting Stopped Protons

Since the PID is very clean and there is good distinction between the bands, a series of simple cuts are used to isolate the stopped proton band:

- cut any event below the line $E_1 = -\frac{1}{2}(E_1 + E_2) + 2000$ to remove the electron spot and scattered muon region;
- cut any event below the line $E_1 = 300$ to remove the protons that have not stopped in the detector (as seen in Fig. 4.8); and finally,
- cut any event above the line $E_1 = 4500e^{-0.0004(E_1+E_2)} + 500$ to remove the remaining deuteron band.

In addition, there is an additional requirement that any bin with < 10 entries is removed. This reduces the number of entries in the extracted band and is included as a systematic later in Sec. 5.5.5.

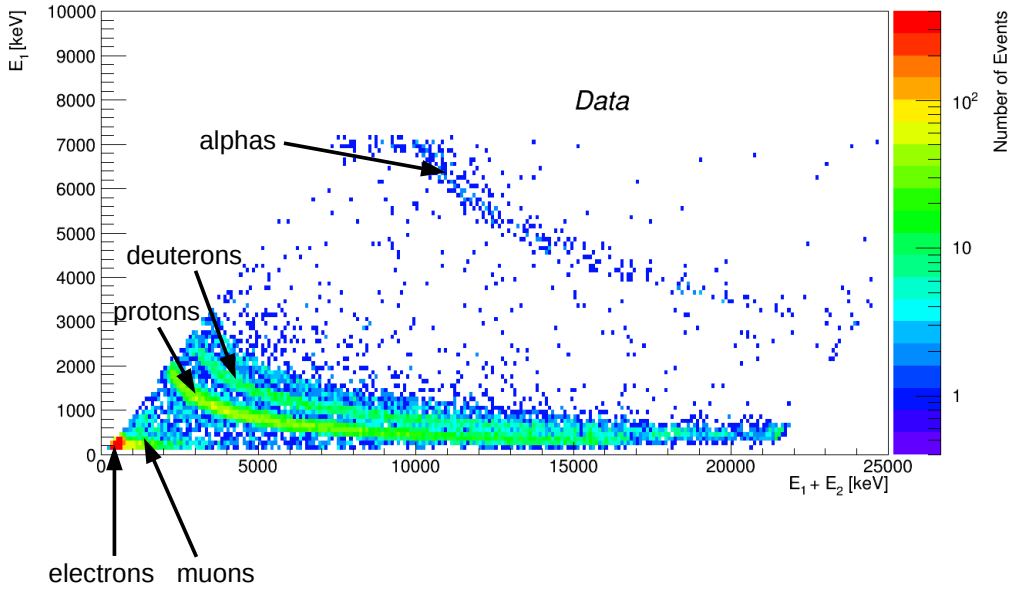

(a) Left Silicon Detectors

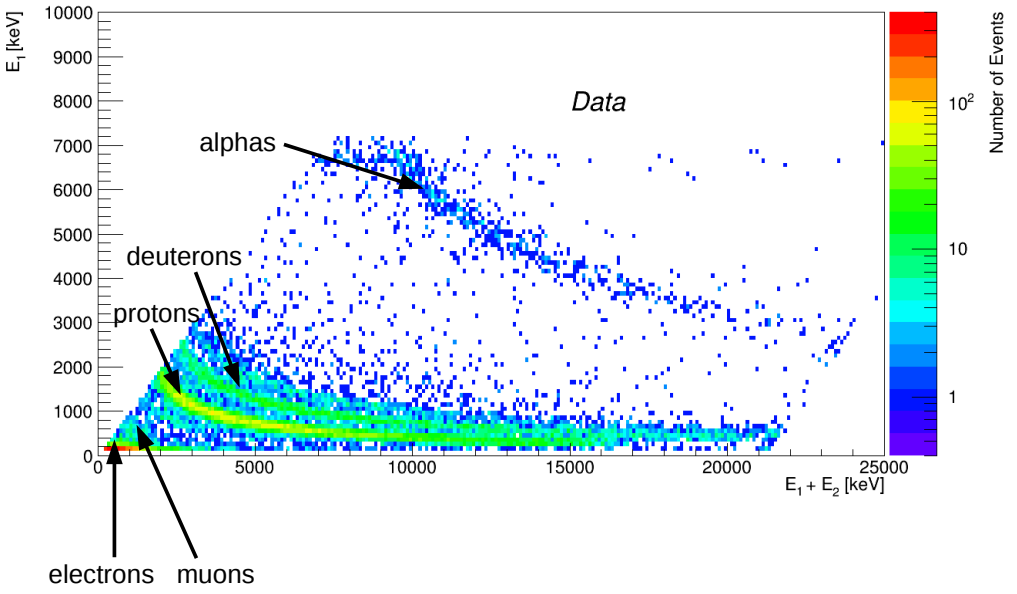

(b) Right Silicon Detectors

Figure 5.13: The E_1 vs $(E_1 + E_2)$ plots for the (a) left and (b) right silicon detector systems.

Fig. 5.14 illustrates these cuts and the resulting stopped proton bands for both the left and right detector arms are shown in Fig. 5.15.

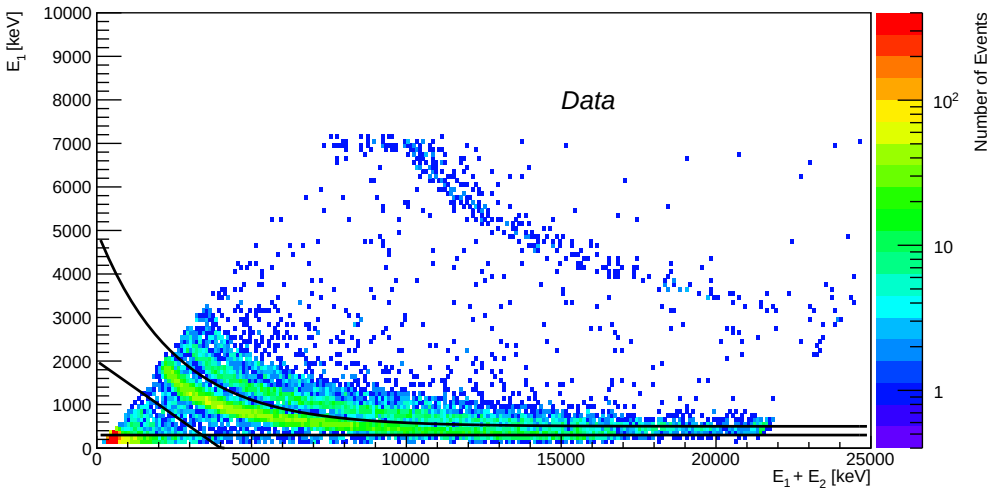

Figure 5.14: A plot of the E_1 vs $(E_1 + E_2)$ plot with lines showing the cuts that are made to extract the stopped proton band. Note that the requirement that a bin has > 10 entries is not shown.

In order to determine the efficiency and purity of this series of cuts, the Monte Carlo simulation described in Sec. 5.2.3 was analysed and the E_1 vs $(E_1 + E_2)$ plots were produced (see Fig. 5.16). As can be seen, because the veto scintillator is not used, the non-stopping proton band merges into the stopped proton band at about 10 MeV and so only protons with kinetic energies up to this value can be accurately measured.

Also, when compared to the data (Fig. 5.13), there is a small discrepency in the location of the proton band because there is a dead layer in the silicon detectors that is not simulated and will be added to the Monte Carlo before the next run. To account for this, a scaling factor was applied to the Monte Carlo, the value of which was obtained by taking a slice in the 2D plot of both data and Monte Carlo at $E_1 + E_2 = 3000$ keV and projecting onto the y-axis. This gives a peak corresponding to the proton band which can be fitted to a Gaussian, the mean of this is used to get a ratio between data and Monte Carlo and a scaling factor of 0.93 ± 0.01 is obtained, where the error is a combination of the fit errors (see Fig. 5.17). This error

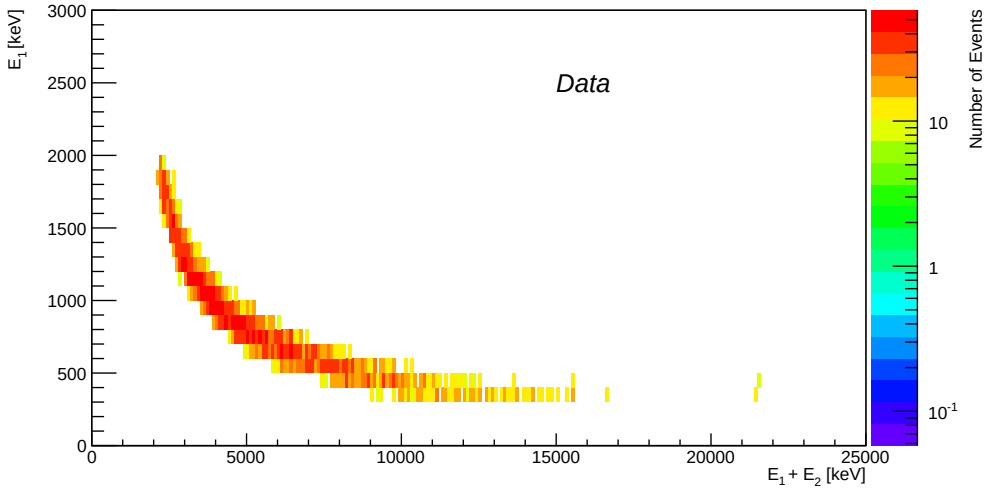

(a) SiL Stopped Protons

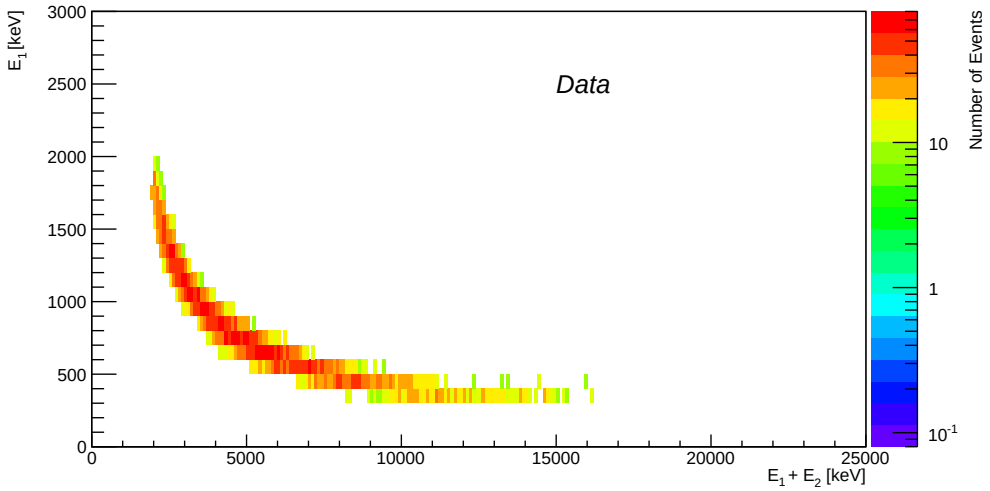

(b) SiR Stopped Protons

Figure 5.15: The E_1 vs $(E_1 + E_2)$ plots showing the stopped protons after all cuts for both the left and right silicon detector systems.

is probably too small, however, there is a larger effect when changing the position of the slice and this is covered in Sec. 5.5.5.

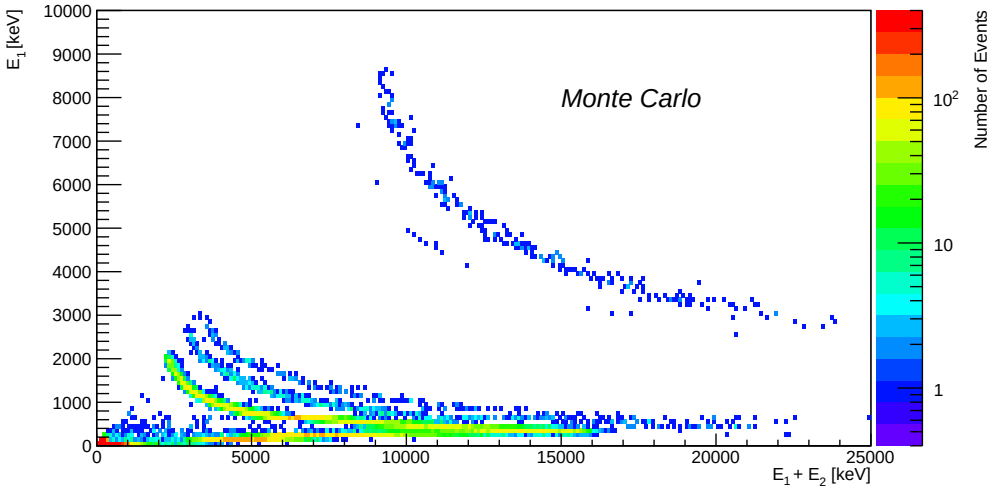

(a) Left Detector System (Monte Carlo)

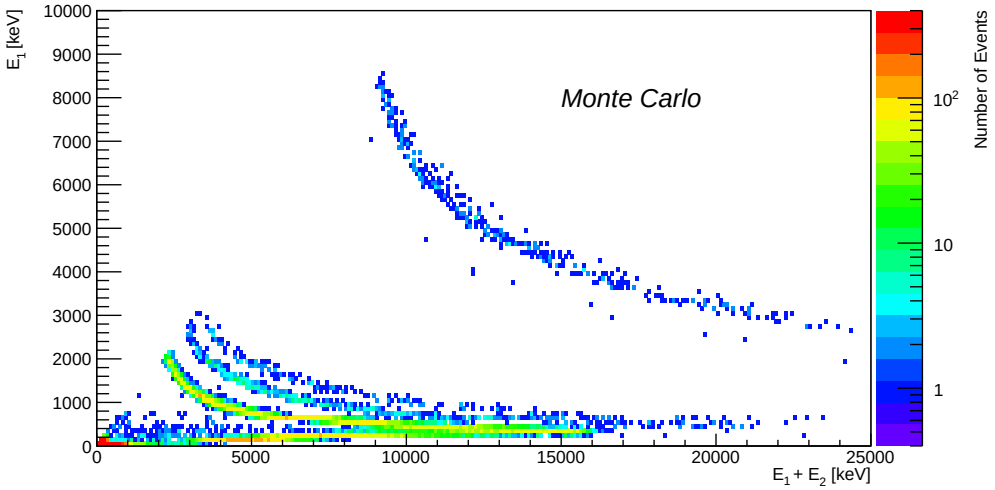

(b) Right Detector System (Monte Carlo)

Figure 5.16: The E_1 vs $(E_1 + E_2)$ plots for the (a) left and (b) right silicon detector systems (Monte Carlo).

The same cuts that were applied to the data were then applied to the Monte Carlo, which results in the proton bands in Fig. 5.18. In addition, because the identity of the particles is also recorded, the bands for each individual particle can be extracted and used to estimate the efficiency and purity of the cut.

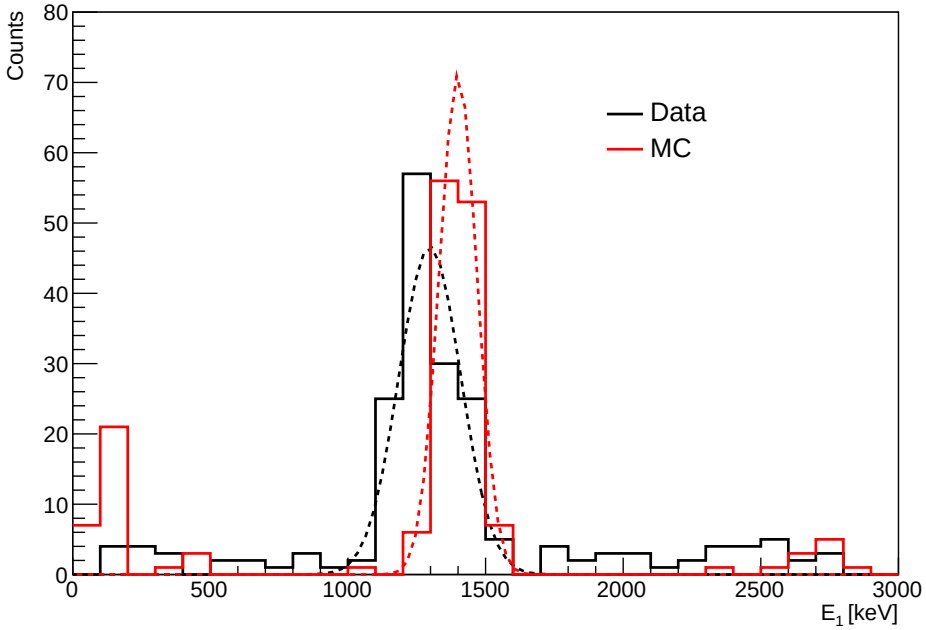

Figure 5.17: Energy slice at $E_1 + E_2 = 3000$ keV illustrating how the Monte Carlo scaling was obtained.

One other important aspect that is not simulated in the Monte Carlo is the detector resolution: the particle bands are rather narrower than they are in the data. To accommodate for this, extra smearing is added by taking the profile of each band and scaling its RMS. The amount to smear a given energy bin i by, $\sigma_{i,\mathrm{det}}$, can be calculated by Eq. 5.5:

$$\sigma^2_{i,\mathrm{det}} = \sigma^2_{i,\mathrm{data}} - \sigma^2_{i,\mathrm{MC}}. \tag{5.5}$$

where $\sigma_{i,\mathrm{data}}$ and $\sigma_{i,\mathrm{MC}}$ are the RMS spread of the band in bin i of the data and Monte Carlo respectively. This value was calculated for each energy bin in the extracted proton band profiles. Since there are several bins where σ_{data} is less than σ_{MC} (due to bins where there is little data), the mean value of σ_{det} for all bins where $\sigma_{\mathrm{data}} > \sigma_{\mathrm{MC}}$ is used as the value to smear all bins by. The final values are $\sigma_{\mathrm{det,\ SiL}} = 57 \pm 26$ keV and $\sigma_{\mathrm{det,\ SiR}} = 51 \pm 27$ keV. The large variance can be seen in Fig. 5.19 and the

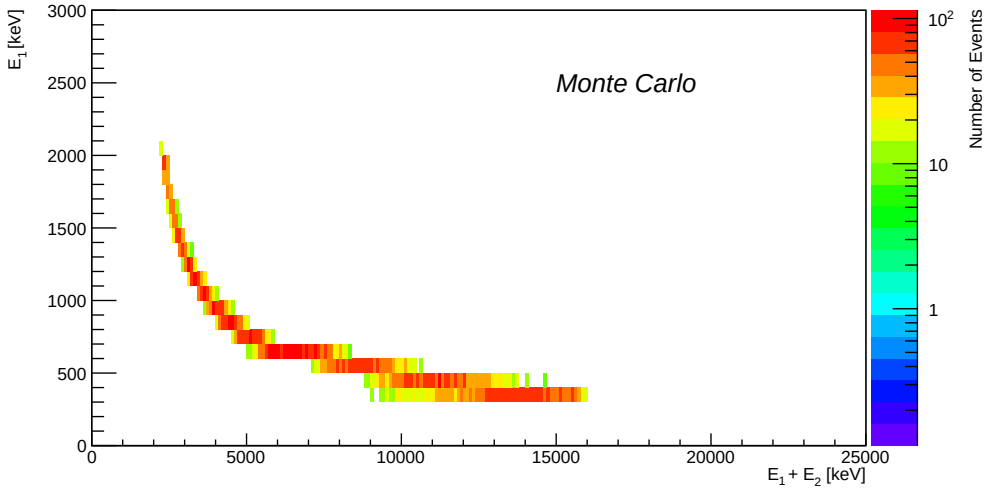

(a) SiL Stopped Protons (Monte Carlo)

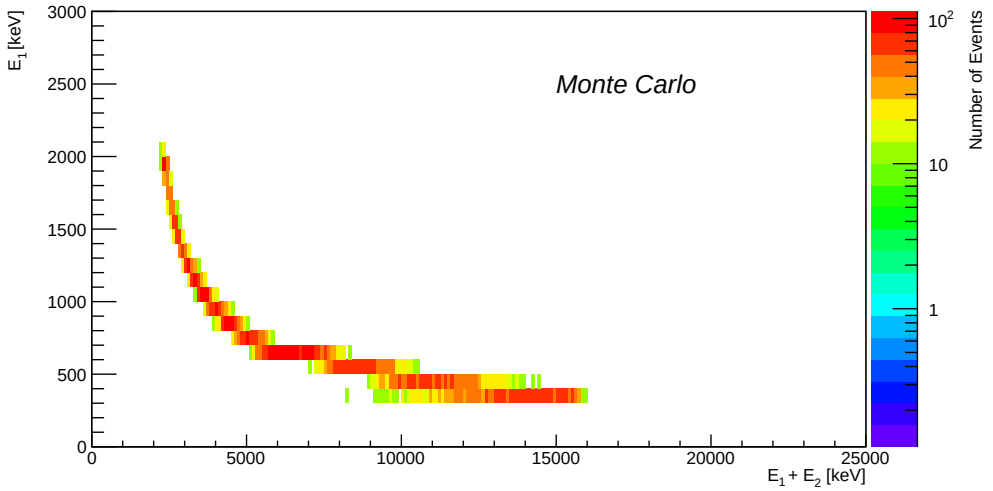

(b) SiR Stopped Protons (Monte Carlo)

Figure 5.18: The E_1 vs $(E_1 + E_2)$ plots showing the stopped protons after all cuts for both the left and right silicon detector systems (Monte Carlo).

systemetic effect of this is covered in Sec. 5.5.5. This could be improved if a more detailed Monte Carlo simulation were available.

The result of Monte Carlo smearing is shown in Fig. 5.20. Profiles of these are then used to obtain the efficiency and purity of the cut. In each energy bin a Gaussian is constructed with a mean and RMS given by the profile for each individual particle type (proton, deuteron etc.) which is then integrated in the limits defined by the profile from the extracted band. The energy dependence is taken into account by taking a weighted average of the efficiency in each $(E_1 + E_2)$ bin. From this it was found that $\varepsilon_{\mathrm{SiL}} = 0.62$, $\varepsilon_{\mathrm{SiR}} = 0.63$, $P_{\mathrm{SiL}} = 0.96$ and $P_{\mathrm{SiR}} = 0.98$, where ε and P are defined in Eq. 5.4.

Finally, the E_1 vs $E_1 + E_2$ plot in the data is projected onto the x-axis and scaled to account for the efficiency and the purity of both the timing and proton cut to get the measured energy spectra shown in Fig. 5.21. Integrating these spectra between 2.5 and 10 MeV gives the number of protons measured as shown in Table 5.3.

Arm	Raw $[\times 10^3]$	$\varepsilon_{\text{time cut}}$	$P_{\text{time cut}}$	$\varepsilon_{\text{proton cut}}$	$P_{\text{proton cut}}$	Result $[\times 10^3]$
Left	6.16 ± 0.08	0.870	0.936	0.62	0.96	10.5 ± 0.1
Right	7.16 ± 0.08			0.63	0.98	12.3 ± 0.1

Table 5.3: The final number of measured protons.

5.5.4 Unfolding

Since the proton energy measured by the silicon detectors will not be the same as the energy of the proton when it was created, it is necessary to unfold the data back to get the original energy. For this, a response matrix is required which maps the observed proton energies with the possible initial proton energies.

For this analysis, the response matrices for the left and right detector arms were obtained from a Monte Carlo simulation of 10^7 protons with a uniform kinetic energy distribution between 0 and 20 MeV generated inside the target based on the stopped muon position distribution in Sec. 5.2.3 and emitted in all directions. The geometrical acceptance of the silicon detectors is inherently included in this

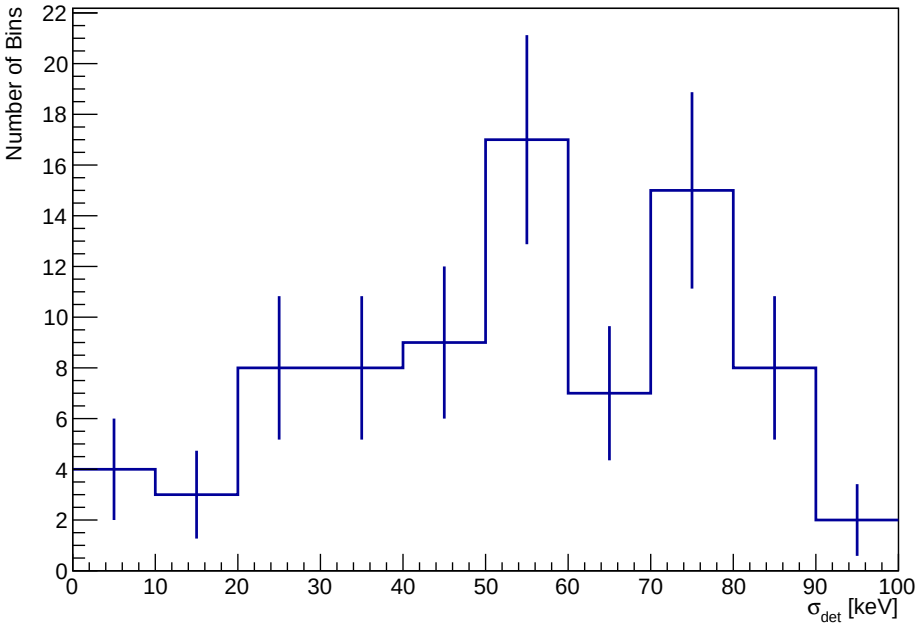

(a) Left Detector System

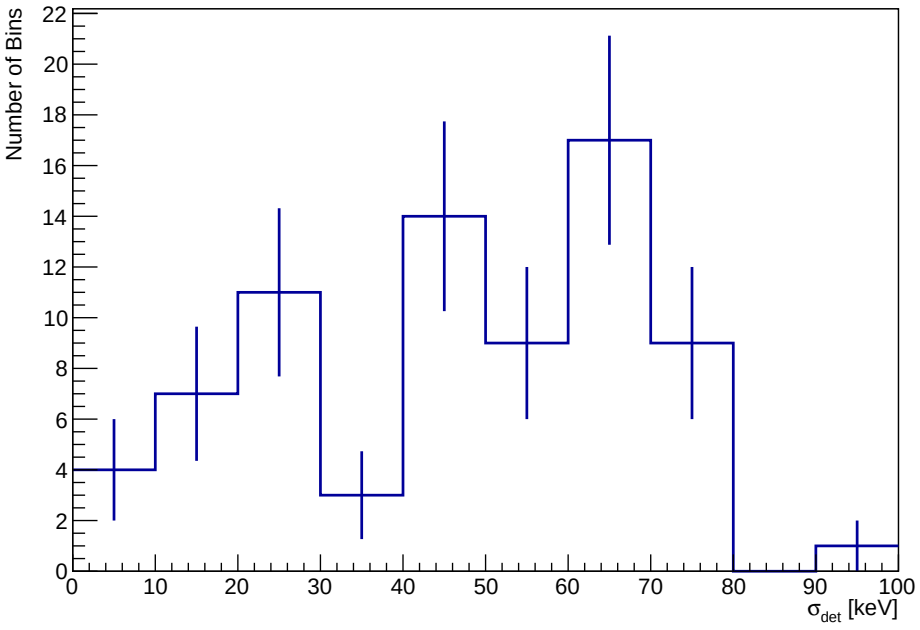

(b) Right Detector System

Figure 5.19: Plots of the distribution of σ_{det} for each detector system. On the x-axis is σ_{det} and on the y-axis is the number of $(E_1 + E_2)$ bins with that σ_{det}.

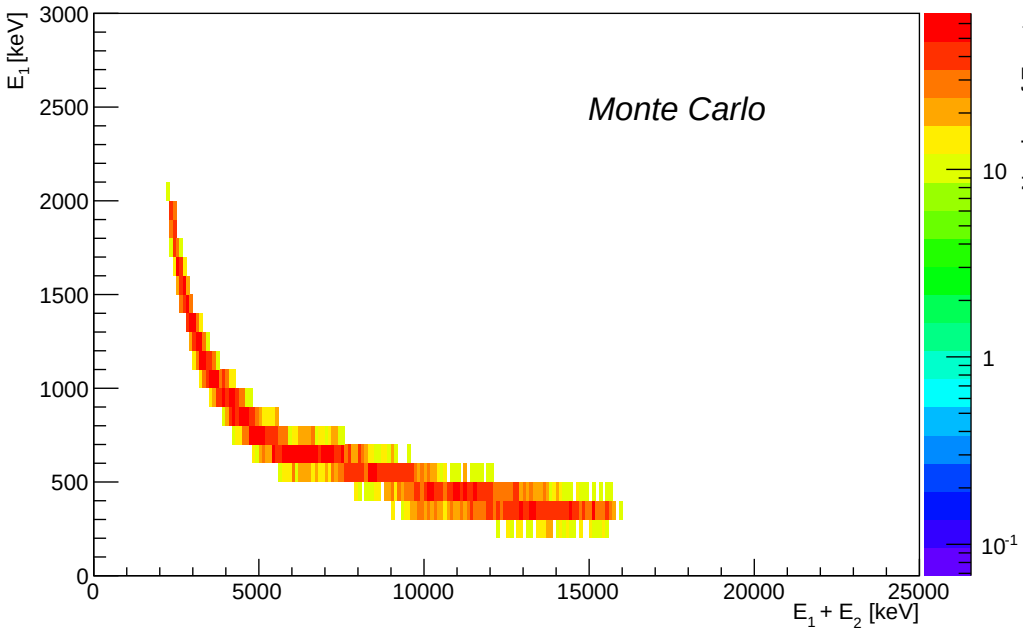

(a) Left Detector System

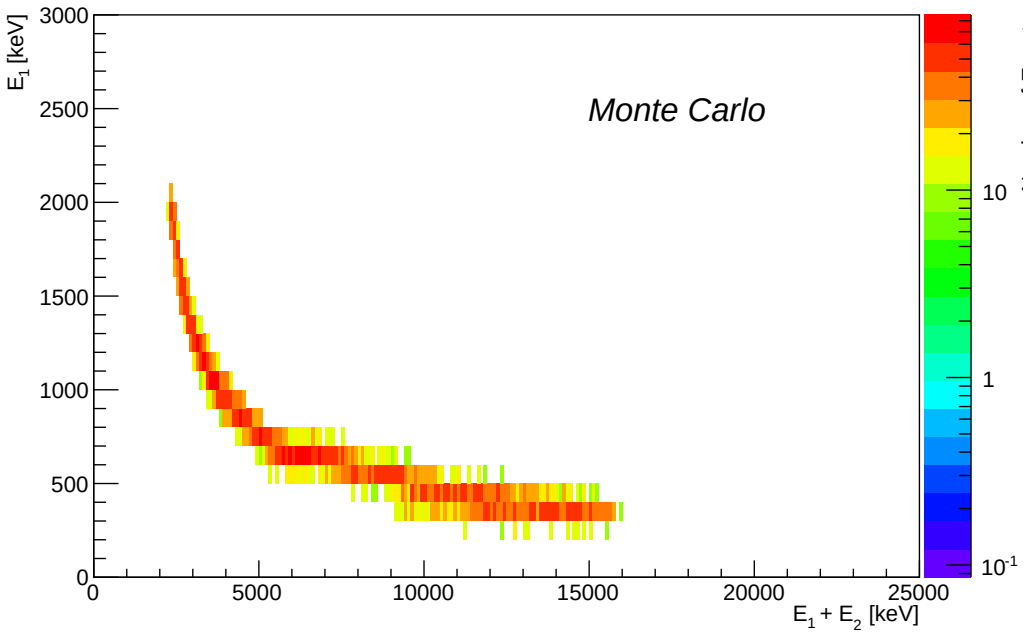

(b) Right Detector System

Figure 5.20: The extracted proton bands from the Monte Carlo after the detector smearing is added.

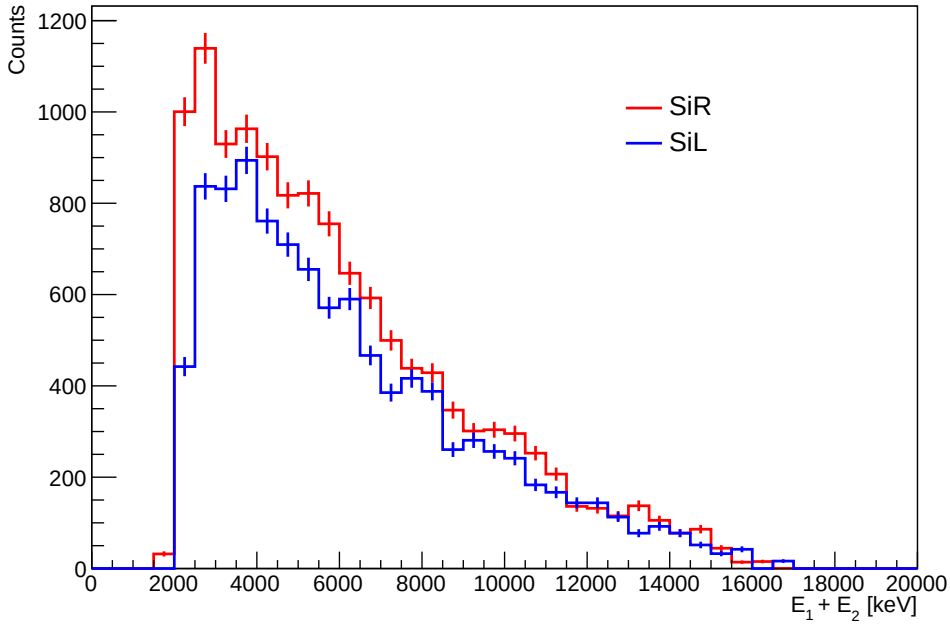

Figure 5.21: The measured energy spectrum of protons stopping in the two detector arms.

because, if the simulated proton does not enter the silicon detector volumes, then the proton is registered as a miss and factored into the unfolding at the next step. Of the 10^7 initial protons, 85594 protons produced hits in the SiR detector system and 86028 protons produced hits in the SiL detector system. This gives a geometrical acceptance of approximately 0.9%.

The response matrices were created with 500 keV wide bins and can be seen in Fig. 5.22. It is expected that all entries will be very close to the diagonal since the energy loss in such a thin piece of aluminium should be small. It is unknown why this is not the case. A possible explanation is that there are a few protons that are scattering off something hard such as the lead shielding around the target but this has yet to be confirmed.

Using these response matrices, the measured proton energy spectra in Fig. 5.21 were unfolded using the Bayesian unfolding method [77] as implemented in the RooUnfold package [78].

The unfolded spectra are shown in Fig. 5.23. As can be seen, the spectra in both arms match very closely at energies above 3.5 MeV but below this there are large

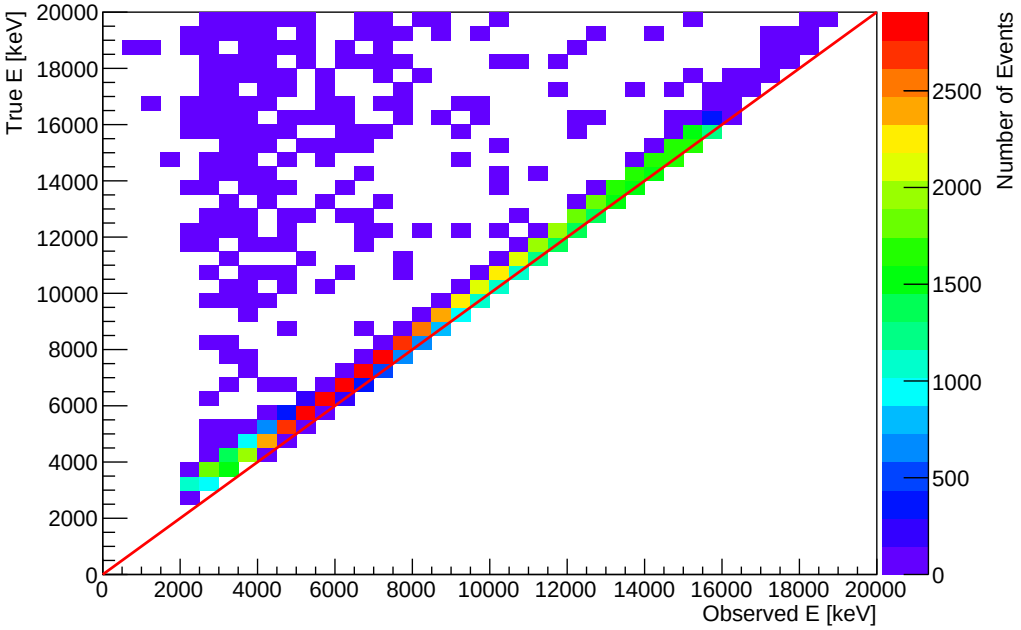

(a) SiL Response Matrix

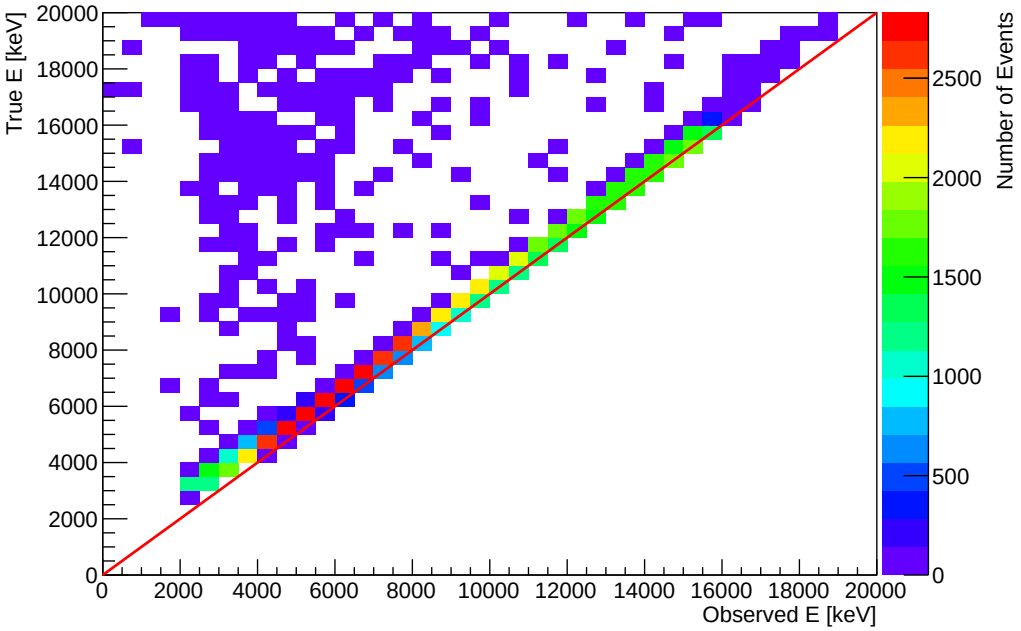

(b) SiR Response Matrix

Figure 5.22: The response matrices used in the unfolding with the observed energy on the x-axis and the true energy on the y-axis. The line $E_{\text{obs}} = E_{\text{true}}$ is also shown in red.

differences, with the right-hand detector giving a much larger rate. By default, four iterations of the Bayesian method were used and when more iterations are performed, there is a larger disagreement between the left and right arms (see Fig. 5.24). Therefore, this disagreement is thought to be an artefact of the unfolding, possibly arising from the fact that there are few entries in the response matrix in this region, and so only protons in the range 3.5 to 10 MeV are included in this analysis.

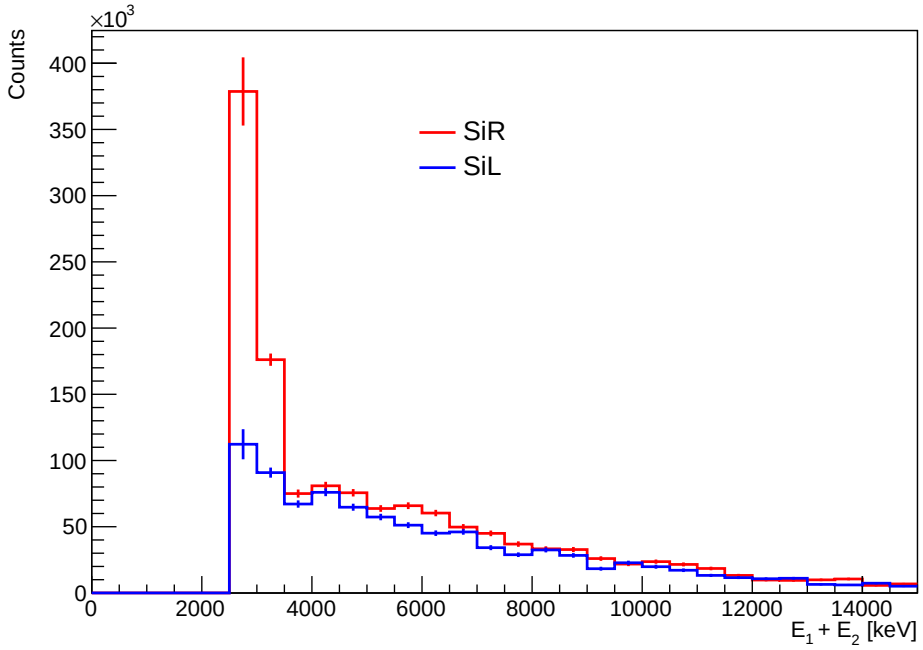

Figure 5.23: The unfolded energy spectra of protons stopping in the two detector arms with the lower and upper energies of this analysis shown in black.

Integrating the unfolded spectra of Fig. 5.23 gives the total number of protons emitted between 3.5 and 10 MeV as:

$$N_L = (0.727 \pm 0.009) \times 10^6 \text{ protons}$$
$$N_R = (0.833 \pm 0.009) \times 10^6 \text{ protons}$$

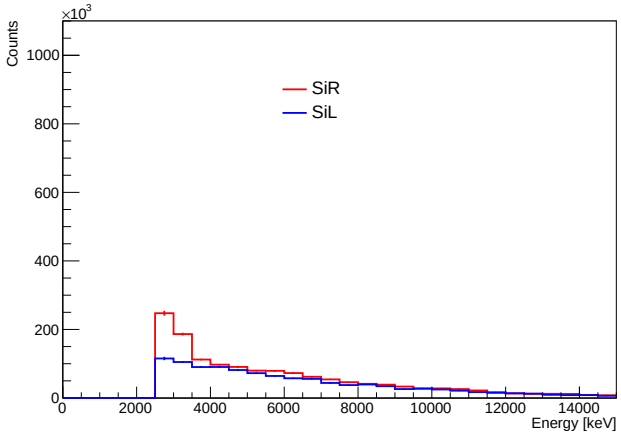

(a) 1 iteration

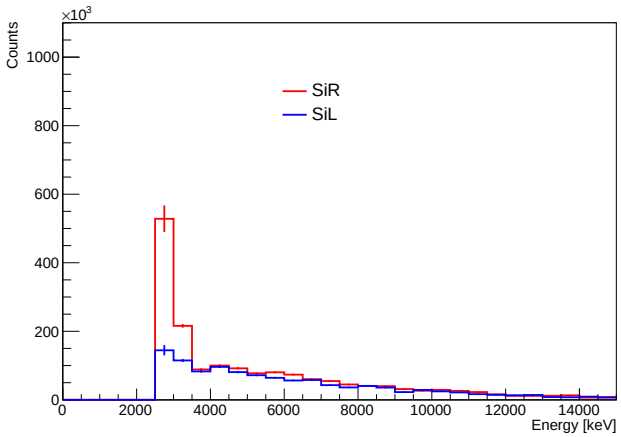

(b) 5 iterations

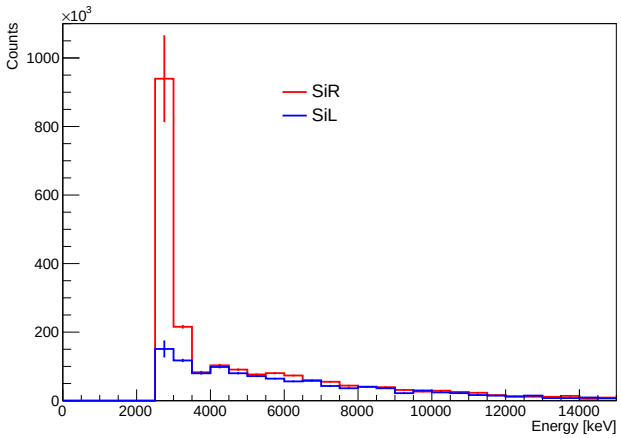

(c) 10 iterations

Figure 5.24: Plots of the unfolding after (a) 1 iteration, (b) 5 iterations and (c) 10 iterations showing that, at energies below 3.5 MeV, the agreement between the unfolded spectra of left and right arms gets worse. This motivates the choice to ignore protons with energies below 3.5 MeV for this analysis.

5.5.5 Systematics

Timing Cut

In Sec. 5.5.1, the arrival times of particles in the Monte Carlo were smeared by a Gaussian with a 187 ns spread in order to evaluate the efficiency and purity of the timing cut for the number of stopped protons. Since the time resolution was found to be 187 ± 32 ns, the calculation was redone with smearings of 155 ns and 219 ns. The recalculated efficiencies and purities, as well as the relative uncertainty in these values, are shown in Table 5.4.

Resolution [ns]	$\varepsilon_{\mathrm{Al}}$	P_{Al}
187	0.870 ± 0.004	0.936 ± 0.005
155	0.856 ± 0.004	0.935 ± 0.005
219	0.834 ± 0.004	0.934 ± 0.005
Relative Uncertainties [%]	4.1	0.2

Table 5.4: The efficiencies and purities of the timing cut for different timing resolutions.

In addition to the smearing, the time cut was changed from 100 ns to 132 ns, with the resulting efficiency, purity and relative uncertainty given in Table 5.5.

Time Cut [ns]	$\varepsilon_{\mathrm{Al}}$	P_{Al}
100	0.870 ± 0.004	0.936 ± 0.005
132	0.854 ± 0.004	0.939 ± 0.005
Relative Uncertainties [%]	1.8	0.3

Table 5.5: The efficiencies and purities of the timing cut for different choices in the timing cut.

Stopped Proton Cut

In Sec. 5.5.3, the Monte Carlo was scaled to the data by a factor of 0.93. Since this had an uncertainty of 0.01, this scale factor was changed and the efficiencies and purities of the stopped proton cut were recalculated and are given in Table 5.6.

Scale Factor	$\varepsilon_{\mathrm{SiL}}$	P_{SiL}	$\varepsilon_{\mathrm{SiR}}$	P_{SiR}
0.93	0.62	0.98	0.63	0.99
0.92	0.63	0.98	0.64	0.99
0.94	0.62	0.98	0.63	0.99
Relative Uncertainties [%]	1.6	0	1.6	0.0

Table 5.6: The efficiencies and purities of the proton cut with different Monte Carlo to data scale factors.

In addition, since the original scale factor was taken from an energy slice at $E_1 + E_2 = 3000$ keV, it was decided to determine a new scale factor for an energy slice at $E_1 + E_2 = 2500$ keV. The recalculated efficiency, purity and relative uncertainty of the cut is given in Table 5.7.

Energy Slice [keV]	Scale Factor	$\varepsilon_{\mathrm{SiL}}$	P_{SiL}	$\varepsilon_{\mathrm{SiR}}$	P_{SiR}
3000	0.93	0.62	0.98	0.63	0.99
2500	0.88	0.62	0.93	0.62	0.95
Relative Uncertainties [%]	–	0.0	5.1	0.0	4.0

Table 5.7: The efficiencies and purities of the proton cut with a scale factor determined from a different energy slice.

Also, since the detector energy smearing that was added in Sec. 5.5.3 had a large variance, the profile bands were scaled by the 1σ band of this. The recalculated efficiencies and purities are given in Table 5.8.

Also, there was a low entry cut to extract the proton band which reduces the number of entries as given in Table 5.9.

Smearing	$\varepsilon_{\mathrm{SiL}}$	P_{SiL}	$\varepsilon_{\mathrm{SiR}}$	P_{SiR}
σ_{det}	0.62	0.98	0.63	0.99
$\sigma_{\mathrm{det}} - 1\sigma$	0.59	0.99	0.60	1.00
$\sigma_{\mathrm{det}} + 1\sigma$	0.64	0.94	0.65	0.97
Relative Uncertainties [%]	4.8	4.1	4.8	2.0

Table 5.8: The efficiencies and purities of the proton cut after adding different amounts of detector smearing.

	N_L	N_R
with low entry cut	12146	12237
without low entry cut	12775	12748
Relative Uncertainties [%]	5.2	4.2

Table 5.9: The number of entries in the extracted band with and without the low entry cut.

Unfolding

In Sec. 5.5.4, the Bayesian method used to unfold the data had four iterations by default. In order to determine a systematic uncertainty, the number of iterations was changed and the number of unfolded protons in the left and right detector arms between 3.5 and 10 MeV was recounted. The results of this are shown in Table 5.10.

In addition, the bin width of the response matrix was reduced from 500 keV to see what effect this had on the final number of unfolded protons. This result of this is given in Table 5.11.

5.5.6 Final Number of Protons

A summary of the systematic uncertainties for the proton analysis is given in Table 5.12 and the final number of protons in each arm is found to be:

$$N_L = (0.727 \pm 0.009\ (\mathrm{stat.}) \pm 0.08\ (\mathrm{syst.})) \times 10^6\ \mathrm{protons}$$

Number of Iterations	N_L [$\times 10^6$]	N_R [$\times 10^6$]
4	0.742 ± 0.009	0.841 ± 0.010
1	0.746 ± 0.006	0.864 ± 0.007
2	0.745 ± 0.008	0.852 ± 0.008
3	0.744 ± 0.008	0.845 ± 0.009
5	0.742 ± 0.009	0.839 ± 0.010
10	0.739 ± 0.010	0.832 ± 0.01
50	0.738 ± 0.010	0.836 ± 0.01
Relative Uncertainties [%]	0.5	2.4

Table 5.10: The number of unfolded protons for different numbers of iterations of the Bayesian method.

Bin Width [keV]	N_L [$\times 10^6$]	N_R [$\times 10^6$]
500	0.742 ± 0.009	0.841 ± 0.010
200	0.751 ± 0.008	0.827 ± 0.009
100	0.727 ± 0.007	0.812 ± 0.008
Relative Uncertainties [%]	2.0	3.4

Table 5.11: The number of unfolded protons for different bin widths in the response matrix.

$$N_R = (0.833 \pm 0.009\ (\text{stat.}) \pm 0.09\ (\text{syst.}))) \times 10^6\ \text{protons}$$

	Left Arm	Right Arm
Timing Cut		
Resolution:		
ε_{Al}	4.1 %	
P_{Al}	0.2 %	
Time Cut Value:		
ε_{Al}	1.8 %	
P_{Al}	0.3 %	
Stopped Proton Cut		
Scale Factor:		
ε_{Al}	1.6 %	1.6 %
P_{Al}	0.0 %	0.0 %
Scale Factor Slice:		
ε_{Al}	0.0 %	0.0 %
P_{Al}	5.1 %	4.0 %
Energy Smear:		
ε_{Al}	4.8 %	4.8 %
P_{Al}	4.1 %	2.0 %
Low Entry Cut:		
N_{folded}	5.2 %	4.2 %
Unfolding		
Iterations:		
N_{unfolded}	0.5 %	2.4 %
Bin Width:		
N_{unfolded}	2.0 %	3.4 %
Total	11.3 %	10.4 %

Table 5.12: The final systematic relative uncertainties in the proton analysis.

Since the unfolding method includes the geometrical acceptance, both detector arms should give the same distribution and, assuming that the systematic errors are 100% correlated, the numbers are inconsistent. It is not known where this inconsistency is

coming from and therefore, an extra uncertainty is added, which is the variance of the two values. The final number of emitted protons is then:

$$N = (0.78 \pm 0.09(\text{corr.}) \pm 0.07(\text{uncorr.})) \times 10^6 \text{ protons}$$

5.6 Final Result

Using the total number of muons captured from Sec. 5.4 of $(24.6 \pm 0.5$ (stat.) $\pm$ 0.6 (syst.)) $\times 10^6$, the final rate of proton emission after nuclear muon capture for protons with energies between 3.5 and 10 MeV is:

$$R = 0.032 \pm 0.005 \text{ protons per muon capture}$$

From the parameterisation in Eq. 4.1, the number of proton per muon capture in the region 3.5 to 10 MeV is 0.09, which is significantly more than the value found in this analysis. Therefore, COMET and MU2E should not expect any unforeseen problems with this background process. This result is consistent with a similar analysis done on the 100 μm aluminium dataset [79].

5.7 Future Plans

In 2015, ALCAP plans to finish the analysis of the silicon datasets in order to compare with the data currently in the literature and also to perform two new runs. The first will take place in June 2015 and will collect neutron and photon emission data and the second will take place in November 2015 and will collect more proton data on more targets.

Chapter 6

Conclusions

"Finally decide (8)"
— Rufus, *Guardian #24946*

The COMET experiment will be searching for the charge lepton flavour violating process $\mu^- + N(Z, A) \rightarrow e^- + N(Z, A)$ with a single event sensitivity of 3×10^{-17}. This search complements direct searches for New Physics since this process can occur in virtual loops where higher mass particles can contribute.

In order to achieve such a low sensitivity COMET will be using new technologies to create the most intense muon beam in the world. This involves a pion capture system to collect all pions emitted when the proton beam strikes the pion production target.

To estimate the muon yield of this system, simulations were performed and found that the number of pions and muons per proton 3 m downstream of the pion production target will be in the region 0.01 to 0.17 if a 16 cm long tungsten target is used. The uncertainty in this result is based on different hadron production models that simulate the proton-target interaction. COMET Phase-I will be using a 60 cm long graphite target is used and a conservative estimate of 0.0292 ± 0.0002 was found and this motivated the decision to run for 110 days rather than the originally planned 90 days.

In addition, because COMET is a rare search experiment, it is very important that all sources of background are known and understood. For this reason, the ALCAP

experiment was set up in order to measure the backgrounds caused when a muon is captured by a nucleus. In particular, the rate of proton emission in aluminium between 3.5 and 10 MeV was found to be 0.032 ± 0.004 protons per muon capture which is significantly less than the value 0.09 that COMET and MU2E have been assuming and so future background estimates will take this into account. In addition, with more analysis a measurement of the spectrum can be made which will then be implemented into the COMET and MU2E simulations.

Bibliography

[1] C. P. Burgess and G. D. Moore, *"The Standard Model: a primer"*, Cambridge University Press (2007).

[2] P. J. Mohr, B. N. Taylor and D. B. Newell, *"CODATA Recommended Values of the Fundamental Physical Constants: 2010"*, Rev. Mod. Phys. **84** 1527 (2012).

[3] D. Hanneke, S. Fogwell and G. Gabrielse, *"New Measurement of the Electron Magnetic Moment and the Fine Structure Constant"*, Phys. Rev. Lett. **100** 120801 (2008).

[4] ATLAS Collaboration, *"Observation of a new particle in the search for the Standard Model Higgs boson with the ATLAS detector at the LHC"*, Phys. Lett. **B716** 1 (2012).

[5] CMS Collaboration, *"Observation of a new boson at a mass of 125 GeV with the CMS experiment at the LHC"*, Phys. Lett. **B716** 30 (2012).

[6] Gargamelle Collaboration, *"Observation of Neutrino Like Interactions Without Muon Or Electron in the Gargamelle Neutrino Experiment"*, Phys. Lett. **B46** 138 (1973).

[7] DONUT Collaboration, *"Observation of tau neutrino interactions"*, Phys. Lett. **B504** 218 (2001).

[8] CDF Collaboration, *"Observation of top quark production in $\bar{p}p$ collisions"*, Phys. Rev. Lett. **74** 2626 (1995).

[9] D0 Collaboration, *"Observation of the top quark"*, Phys. Rev. Lett. **74** 2632 (1995).

[10] D. Walsh, R. F. Carswell and R. J. Weymann, *"0957 + 561 A, B - Twin quasistellar objects or gravitational lens"*, Nature **279** 381 (1979).

[11] N. Cabibbo, *"Unitary Symmetry and Leptonic Decays"*, Phys. Rev. Lett. **10** 531 (1963).

[12] M. Kobayashi and T. Maskawa, *"CP Violation in the Renormalizable Theory of Weak Interaction"*, Prog. Theor. Phys. **49** 652 (1973).

[13] B. Pontecorvo, *"Mesonium and anti-mesonium"*, Sov. Phys. JETP. **6** 429 (1957).

[14] Z. Maki, M. Nakagawa and S. Sakata, *"Remarks on the unified model of elementary particles"*, Prog. Theor. Phys. **28** 870 (1962).

[15] B. Pontecorvo, *"Neutrino Experiments and the Problem of Conservation of Leptonic Charge"*, Sov. Phys. JTEP. **26** 984 (1968).

[16] A. D. Sakharov, *"Violation of CP Invariance, c Asymmetry, and Baryon Asymmetry of the Universe"*, Pisma Zh. Eksp. Teor. Fiz. **5** 32 (1967).

[17] Planck Collaboration, *"Planck 2013 results. I. Overview of products and scientific results"*, Astronomy & Astrophysics, **571** A1 (2014).

[18] SuperKamiokande Collaboration, *"Evidence for oscillation of atmospheric neutrinos"*, Phys. Rev. Lett. **81** 1562 (1998).

[19] SNO Collaboration, *"Direct evidence for neutrino flavor transformation from neutral current interactions in the Sudbury Neutrino Observatory"*, Phys. Rev. Lett. **89** 011301 (2002).

[20] T2K Collaboration, *"Indication of Electron Neutrino Appearance from an Accelerator-produced Off-axis Muon Neutrino Beam"*, Phys. Rev. Lett. **107** 041801 (2011).

[21] B. Kayser, F. Gibrat-Debu and F. Perrier, *"The Physics of Massive Neutrinos"*, World Scientific (1989).

[22] R. Barbieri, P. Creminelli, A. Strumia and N. Tetradis, *"Baryogenesis through leptogenesis"*, Nucl. Phys. **B575** 61 (2000).

[23] E. Noether, *"Invariant Variation Problems"*, Gott. Nachr. **1918** 235 (1918).

[24] A. de Gouvêa, *"(Charged) Lepton Flavor Violation"*, Nucl. Phys. **B188** 303 (2009).

[25] Muon G-2 Collaboration, *"Final Report of the Muon E821 Anomalous Magnetic Moment Measurement at BNL"*, Phys. Rev. **D73** 072003 (2006).

[26] E. P. Hincks and B. Pontecorvo, *"Search for gamma-radiation in the 2.2-microsecond meson decay process"*, Phys. Rev. **73** 257 (1948).

[27] Particle Data Group, *"Review of Particle Physics"*, Chin. Phys. **C38** 090001 (2014).

[28] MEG Collaboration, *"MEG Upgrade Proposal"*, `arXiv:1301.7225`, (2013).

[29] COMET Collaboration, *"COEMT Technical Design Report"*, `http://comet.kek.jp/Documents_files/PAC-TDR-2014/PAC-Review-20141110.pdf`.

[30] Mu3e Collaboration, `http://www.psi.ch/mu3e/`.

[31] Mu2e Collaboration, *"Mu2e Technical Design Report"*, `http://mu2e-docdb.fnal.gov/cgi-bin/ShowDocument?docid=4299`.

[32] J.Adam et. al. *"The MEG detector for $\mu^+ \to e^+\gamma$ decay search"*, Eur. Phys. J. **C73** 2365 (2013).

[33] SINDRUM Collaboration, *"Search for the Decay $\mu^+ \to e^+e^+e^-$"*, Nucl. Phys. **B299** 1 (1988).

[34] SINDRUM II Collaboration, *"A Search for muon to electron conversion in muonic gold"*, Eur. Phys. J. **C47** 337 (2006).

[35] Y. Kuno and Y. Okada, *"Muon Decay and Physics Beyond the Standard Model"*, Rev. Mod. Phys. **73** 151 (2001).

[36] V. Cirigliano, R. Kitano, Y. Okada and P. Tuzon, *"On the model discriminating power of $\mu - e$ conversion in nuclei"*, Phys. Rev. **D80** 013002 (2009).

[37] D. F. Measday, T. J. Stocki, B. A. Moftah and H. Tam, *"γ rays from muon capture in ^{27}Al and natural Si"*, Phys. Rev. **C76** 035504 (2007).

[38] A. Czarnecki, X. Garcia i Tormo and W. J. Marciano, *"Muon decay in orbit: spectrum of high-energy electrons"*, Phys. Rev. **D84** 013006 (2011).

[39] A. Czarnecki, X. Garcia i Tormo and W. J. Marciano, *"Muon decay in orbit spectra for $\mu - e$ conversion experiments"*, Hyperfine Interact. **210** 19 (2012).

[40] A. Czarnecki, M. Dowling, X. Garcia i Tormo, W. J. Marciano and R. Szafron, *"Michel decay spectrum for a muon bound to a nucleus"*, `arXiv:1406.3575` (2014).

[41] R. M. Dzhilkibaev and V. M. Lobashev, *"The solenoid muon capture system for the MELC experiment"*, Sov. J. Nucl. Phys. **49** 384 (1989).

[42] MuSIC Collaboration, *"First measurements of muon production rate using a novel pion capture system at MuSIC"*, J. Phys. Conf. Ser. **408** 012079 (2013).

[43] T. Suzuki, D. F. Measday and J. P. Roalsvig, *"Total Nuclear Capture Rates for Negative Muons"*, Phys. Rev. **C35** 2212 (1987).

[44] HARP Collaboration, *"The HARP detector at the CERN PS"*, Nucl. Instrum. Meth. **A571** 527 (2007).

[45] HARP-CDP Collaboration, *"Comments on: The HARP detector at the CERN PS"*, Nucl. Instrum. Meth. **A571** 562 (2007).

[46] C. Booth, *"Rebuttal of Comments to The HARP detector at the CERN PS"*, Nucl. Instrum. Meth. **571** 564 (2007).

[47] HARP Collaboration, *"Large-angle production of charged pions with 3-12.9-GeV/c incident protons on nuclear targets"*, Phys. Rev. **C77** 055207 (2008).

[48] GEANT4 Collaboration, *"GEANT4: A Simulation toolkit"*, Nucl. Instrum. Meth. **A506** 250 (2003).

[49] J. Allison et. al. *"Geant4 developments and applications"*, IEEE Trans. Nucl. Sci. **53** 270 (2006).

[50] N. V. Mokhov, *"The MARS code system user's guide version 13(95)"*, FERMILAB-FN-0628 `http://www-ap.fnal.gov/MARS/` (1995).

[51] N. V. Mokhov and O. E. Krivosheev, *"MARS code status"*, FERMILAB-CONF-00-181 943 (2000).

[52] N. V. Mokhov, *"Status of MARS code"*, FERMILAB-CONF-03-053 (2003).

[53] N. V. Mokhov et. al. *"Recent enhancements to the MARS15 code"*, Radiat. Prot. Dosim. **116** 99 (2005).

[54] S. G. Mashnik, *"Overview and Validation of the CEM and LAQGSM Event Generators for MCNP6, MCNPX, and MARS15"*, arXiv:0812.1820 (2008).

[55] GEANT4 Collaboration, *"GEANT4 Physics Reference Manual"*, http://geant4.web.cern.ch/geant4/UserDocumentation/UsersGuides/PhysicsReferenceManual/fo/PhysicsReferenceManual.pdf

[56] K. K. Gudima, S. G. Mashnik and V. D. Toneev, *"Cascade-exciton model of nuclear reactions"*, Nucl. Phys. **A401** 329 (1983).

[57] V. S. Barashenkov, A. S. Il'inov, N. M. SobolevskiÄŋ and V. D. Toneev, *"Interaction of particles and nuclei of high and ultrahigh energy with nuclei"*, Soviet Physics Uspekhi, **16** 1 31 (1973).

[58] S. G. Mashnik, M. I. Baznat, K. K. Gudima, A. J. Sierk and R. E. Prael, *"Extension of the CEM2k and LAQGSM codes to describe photo-nuclear reactions"*, arXiv:0503061 (2005).

[59] H. W. Bertini, *"Low-Energy Intranuclear Cascade Calculation"*, Phys. Rev. **131** 1801 (1963).

[60] J. Wellisch and G. Folger, *"The binary cascade"*, CERN-2005-02 313 (2005).

[61] AlCap Collaboration, *"PSI Proposal"*, http://muon.npl.washington.edu/exp/AlCap/R-13-03.1_BV44.pdf (2013).

[62] G. Heusser and T. Kirsten, *"Radioisotope production rates by muon capture"*, Nucl. Phys. **A195** 369 (1972).

[63] S. E. Sobottka and E. L. Wills, *"Energy Spectrum of Charged Particles Emitted Following Muon Capture in* Si^{28}*"*. Phys. Rev. Lett. **20** 12 596 (1968).

[64] A. Wyttenbach et. al. *"Probabilities of Muon Induced Nuclear Reactions Involving Charged Particle Emission"*, Nucl. Phys. **A294** 278 (1978).

[65] K. S. Krane et. al. *"Energetic charged particle spectrum following mu- capture by nuclei"*, Phys. Rev. **C20** 1873 (1979).

[66] E. Hungerford, *"Comment on Proton Emission after Muon Capture"*, MECO Note 34.

[67] Paul Scherrer Institute, *"πE1 Secondary Beam Line"*, http://aea.web.psi.

ch/beam2lines/pie1.pdf.

[68] MuSun Collaboration, *"Muon Capture on the Deuteron – The MuSun Experiment"*, arXiv:1004.1754 (2010).

[69] MuSun Collaboration, *"Progress Report 2012 and Beam Request for 2013"*, http://muon.npl.washington.edu/exp/MuSun/documents/progress12.pdf.

[70] http://www.micronsemiconductor.co.uk/pdf/g.pdf

[71] http://www.micronsemiconductor.co.uk/pdf/msx.pdf

[72] http://www.ortec-online.com/download/gamma-x.pdf

[73] *"MIDAS: Maximum Integrated Data Acquisition System"*, http://midas.psi.ch.

[74] R. Brun and F. Rademakers, *"ROOT - An Object Oriented Data Analysis Framework"*, Nucl. Instrum. Meth. **A389** 81 http://root.cern.ch (1997).

[75] International Atomic Energy Agency, https://www-nds.iaea.org/xgamma_standards/.

[76] *"PSI Graphic Turtle Framework by U. Rohrer based on a CERN-SLAC-FERMILAB version by K.L. Brown et al."*, http://aea.web.psi.ch/Urs_Rohrer/MyWeb/turtle.htm.

[77] G. D'Agostini, *"A Multidimensional unfolding method based on Bayes' theorem"*, Nucl. Instrum. Meth. **A362** 487 (1995).

[78] T. Adye, *"Unfolding algorithms and tests using RooUnfold"*, arXiv:1105.1160 http://hepunx.rl.ac.uk/~adye/software/unfold/RooUnfold.html (2011).

[79] T. H. Nam, *"A Study of Muon Capture for Muon to Electron Conversion Experiments"*, PhD Thesis, Osaka University, (2014).